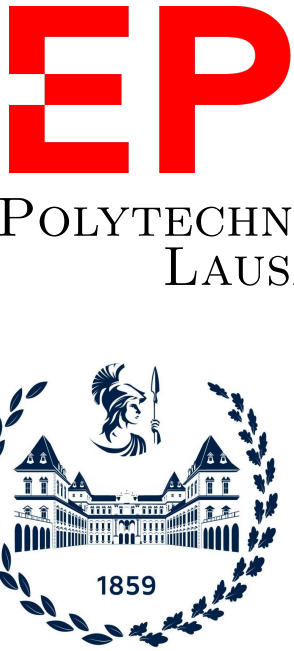

École Polytechnique Fédérale de Lausanne

Politecnico di Torino

1D thermal modeling of an high-speed compressor-turbine unit with CFD-FEA validation

Master Thesis

Author:
Andrea Cioffi

Supervisors:
Prof. Jürg Schiffmann
Prof. Daniela Anna Misul
PhD candidate Victoria He

2nd January 2024

Acknowledgements

Firstly, I would like to thank my project supervisor Victoria, whose fundamental support and invaluable insights guided the research and contributed significantly to my professional and personal growth, sharing with me some important aspects of her experience and knowledge.

Special appreciation goes to Professor Jürg Schiffmann, whose lab provided an incredible environment for discussion, suggestions, and the birth of ideas.

To all the members of the LAMD staff, from fellow Ph.D. students to post-docs, and engineers: your constant presence and engagement made this academic endeavor truly enriching. You always integrated me into your group as an effective member of the lab, starting with the sled experience in Les Diablerets, through the several coffee breaks where curious discussions were always raised, to the pizza days and apèro for celebrating special events. Thank you, Lena and Arnau, for sharing desperation and support through the development of our master thesis, and the special moments out of the office.

A great thanks to Professor Daniela Anna Misul, my thesis supervisor at Politecnico of Turin. Thanks to the "Thermal and Hydraulic Machines" course, taught by you, I was able to approach and delve deeper into the world of turbomachinery, in which I have a deep interest.

I also want to express my gratitude to colleagues and friends from Politecnico di Torino, where my academic journey began in 2018. During these years I had the chance to meet valuable and sincere people with whom I shared many worthy moments.

Last but not least, a heartfelt thanks goes to my parents for their incredible support. Despite their unfamiliarity with the university system, they consistently did their best to encourage, motivate, and believe in me.

Abstract

High-speed turbomachinery, characterized by elevated power density and rotational speed, frequently encounters challenges associated with high-temperature distribution. An accurate understanding of the thermal effects and heat dissipation through the machine's components is crucial throughout the design process - from the initial to the final design. The coupling condition between thermal and mechanical effects, which results in component expansions and residual stress nucleation, has to be carefully modeled, hence a multiphysics problem and conjugated heat transfer analysis must be developed.

A comprehensive transient thermal assessment of high-speed turbomachinery requires the integration of multi-domain modeling involving fluid dynamics, thermodynamics, and thermo-mechanics. However, achieving high accuracy while maintaining low computational cost presents a conflicting but essential objective. Conventional conjugated heat transfer problems, investigated through coupled computational fluid dynamics and finite element analysis simulations, often suffer from computational inefficiencies and long processing times. Furthermore, such simulations are typically performed at an advanced stage of the machine's geometry development - thus the geometry has to be known and defined.

This study addresses these challenges by developing a two-dimensional model for a high-speed compressor turbine unit. The idea is to exploit fundamental analytical relationships to analyze the heat transfer modes occurring in the machine, exploiting a lumped parameters approach rather than other numerical methods. The model's accuracy and performance will be validated through finite element analysis (FEA) and computational fluid dynamics (CFD), ensuring the suitability of the 2D model for early-stage design evaluations. The software used are *Matlab*, for data analysis and post-processing, *Simulink* and *Simscape* for the lumped parameter model, and *Ansys Mechanical* and *Fluent* for the FEA/CFD validations.

The research gave valuable insights into how to properly address a thermal model. Comparison between the 2D thermo-mechanical network and CFD/FEA validation drove the workflow in the proper way, and experimental results were matched as well. Besides the thermal management, critical areas such as the radial gas bearings were investigated in terms of thermal expansions, where high centrifugal forces coupled with severe temperature, could lead to system failures. However, this research showed safe operating conditions, at least in this region.

Contents

List of Figures

List of Tables

Nomenclature

α	Surface absorptivity [-]/Groove width ratio [-]/Thermal diffusivity [m s]
α	Thermal expansion coefficient [K^{-1}]
β	Volumetric coefficient of thermal expansion [K^{-1}]
δ	Radial length of the air gap [m]
$\dot{\phi}$	Energy flow rate [W]
$\dot{m}$	Mass flow rate [$kg\,s^{-1}$]
ϵ	Strain [-]
ϵ	Surface emissivity [-]
ν	Kinematic viscosity [m^2/s]
ν	Poisson ratio [-]
ω	Rotational speed [$rad\,s^{-1}$]
$\overline{d}$	Mean hydraulic diameter [-]
ρ	Density of a material [kg/m^3]
σ	Constant of Stefan-Boltzmann $= 5.67e-8$ [$W/K^4/m^2$]
σ	Stress [MPa]
A_{vol}	Volute surface-solid contact area [m^2]
C_f	Skin friction coefficient [-]
D	Cylinder's diameter [m]
d_h	Hydraulic diameter [m]
E	Specific heat flux by radiation from a real surface [W/m^2]
E_b	Specific heat flux by radiation from a black body [W/m^2]
g	Gravitational acceleration [m/s^2]
G_{abs}	Radiadion from external sources absorbed by a surface [W/m^2]
Gr	Grashof number [-]
h	Enthalpy [$J\,kg^{-1}$]
h_g	Groove clearance [m]
h_r	Radial clearance [m]

h_v Specific enthalpy of the gas volume [$\mathrm{J\,kg^{-1}}$]

k Material's thermal conductivity [$\mathrm{W\,m^{-1}\,K^{-1}}$]

L Characteristic length [m]

L_δ Axial length of the air gap [m]

L_{arc} Length of the spiral arc [m]

M Mass of the constant volume chamber block [kg]

m Thermal inertia [kg]

Nu Nusselt number [-]

Nu_{avg} Average Nusselt number [-]

p Pressure [bar]

q Specific convective heat flux [$\mathrm{W/m^2}$]

q_x Specific heat flux in x direction [$\mathrm{W/m^2}$]

q_{rad} Total specific heat flux emitted by radiation[$\mathrm{W/m^2}$]

Q_{wHGJB} Windage losses in HGJB [W]

Q_{wSGTB} Windage losses in SGTB [W]

Q_{w-disk} Windage losses of a rotating disk [W]

$Q_{w-rotor}$ Windage losses of a rotating shaft [W]

$Q_{windage}$ Windage losses [W]

R Specific gas constant [$\mathrm{J\,K^{-1}\,mol^{-1}}$]

R_a Axial thermal resistance [$\mathrm{K\,W^{-1}}$]

r_m Average of stator and rotor radii [m]

r_o Rotor outer radius [m]

R_r Radial thermal resistance [$\mathrm{K\,W^{-1}}$]

$R_{(\theta)}$ Radius of the logarithmic spiral [m]

R_{in} Disk inner radius [m]

R_{out} Disk outer radius [m]

Ra Rayleigh number [-]

Re Reynolds number [-]

Re_ϕ Disk rotational Reynolds number [-]

$Re_{\overline{D}}$ Reynolds number at the mean volute hydraulic diameter [-]

rho Density [$\mathrm{kg/m^3}$]

T	Convective heat transfer coefficient [W/K/m^2]
T	Temperature [K]
T_∞	Fluid's undisturbed temperature [K]
T_∞	Unperturbed fluid temperature [K]
T_s	Solid's surface temperature [K]
T_s	Surface temperature [K]
Ta	Taylor number [-]
Ta_m	Modified Taylor number [-]
Ta_{cr}	Critical Taylor number [-]
V	Volume of the constant volume chamber block [m^3]
v	Flow velocity [m s^{-1}]
v_{axial}	Flow's axial velocity [m s^{-1}]
v_{red}	Reduced velocity [m s^{-1}]
Z	Compressibility factor [-]

Chapter 1

Introduction

1.1 Context

A concept to design a high-speed, small-scale, gas-bearing supported, and turbine-driven compressor system has been set up at the Laboratory of Applied Mechanical Design (LAMD). The Compressor Turbine Unit (CTU) is part of a Solid Oxide Fuel Cell (SOFC), which aims to generate electrical and thermal energy from biomass. The small-scaled Combined Heat and Power (CHP) system processes the biomass and generates syngas, which is compressed by the CTU, to go into a fuel cell stack, as represented by the schematics in Figure 1.1

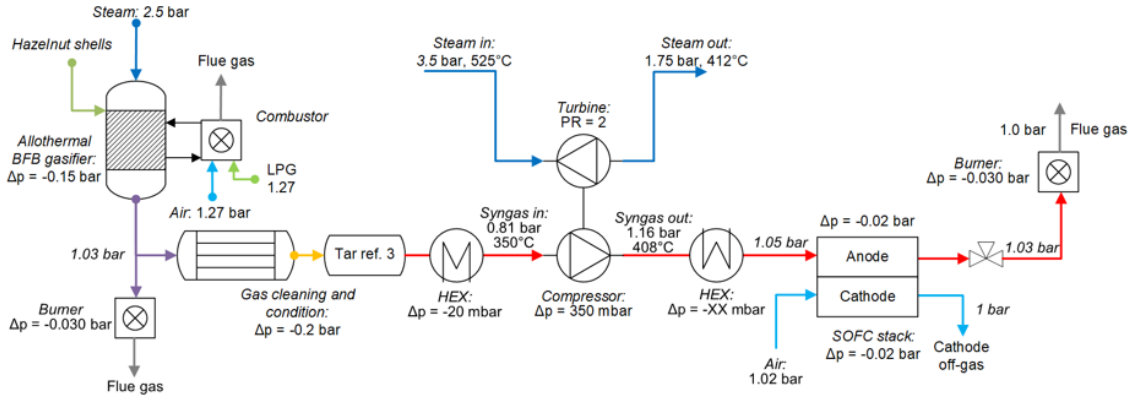

Figure 1.1
CTU and SOFC plant overview and system's boundary conditions [1].

1.2 Motivation

The Compressor Turbine Unit (CTU) is a machine subjected to high temperatures, thus the primary challenges lie in effectively managing the thermal gradients, resulting from the different working temperatures between the compressor and turbine sides. The temperature distribution is also strictly associated with the heat generated from windage losses, which is a function of the working condition and may have a dominant role in confined areas such as the gas-bearing gaps.

The centrifugal forces experienced at high rotational speeds coupled with high-temperature distribution can give rise to critical material expansions. Negligence to anticipate and address these phenomena can lead to either system failure or an overestimated design, with consequences in the dynamic stability of rotating parts

and the machine's efficiency. It can be stated that even a modest increase of 10% in the impeller's tip clearance can result in an efficiency decline of 3 to 4 points [2].

By comprehensively investigating the aforementioned thermal challenges and their impact on CTU performance, this research strives to provide scientific insights that can be carried out for robust and efficient CTU systems design. The findings will enhance such systems' reliability, performance, and efficiency while mitigating the risk of operational failures.

1.3 Goals of the research

This project aims to establish a fast, real-time, and reliable model to predict the overall temperature distribution of the investigated CTU. The idea is to be able to run it along with experiments - allowing the researchers to have a complete idea of all the overall thermal conditions, even in points not reachable with measuring probes. Additionally, the model can be fed with measured boundary conditions to improve its consistency further.

In a coupled thermal problem, the overall thermal management is strictly dependent upon the mechanical behavior of the components, such as thermal expansions that would affect the windage loss generation due to viscous forces to a major extent. Therefore one sees the necessity to further couple the thermal analysis with a mechanical one, to put more degrees of freedom in the overall assessment.

1.4 Methodology

To avoid the computational and time demand associated with FEA and CFD 3D simulations, a lumped parameter approach is adopted in this study. Achieving accurate 3D volume discretization, especially in small gaps of the order of 10^{-6} meters, results in challenging work. Furthermore, heavy computational methods do not easily allow geometry modifications, hence the method applied in this research keeps an eye also on this regard, guaranteeing flexibility in case design changes are expected.

In light of these considerations, a 1D network approach, connected to building a 2D model, is applied in this analysis, following the work of [3]. A lumped parameter approach is employed to accomplish the research objectives, wherein the level of accuracy required determines the degree of discretization of the 2D geometry. Initially, the solid components are modeled to capture conductive heat transfer occurring within the solid domain. State-of-the-art correlations are employed to model the complex fluid patterns observed in regions such as the gas bearing, modeling the heat transfer and windage losses. Finally, the remaining fluid domain is represented using 1D fluid networks directly interacting with the solid blocks.

The validation process of the thermal model involves comparison with FEA and CFD results for both steady and transient states. However, it is important to mention that the approach employed in this study may have limitations when encountering

non-axisymmetric conditions. In such cases, 3D simulations become necessary to obtain reliable and accurate outcomes.

The software used are *Matlab*, for data analysis and post-processing, *Simulink* and *Simscape* for the lumped parameter model, and *Ansys Mechanical* and *Fluent* for the FEA/CFD validations.

1.5 Machine under investigation

1.5.1 Assembly description

The CTU is composed of three sub-domains: the compressor side, the turbine side, and the steam injection side, which includes the gas-bearings-supported transmission system.

The turbine side features a radial turbine that operates with steam. The steam enters the volute at a temperature of 525 °C and a pressure of 3.5 bar and exits at a temperature of 430 °C and a pressure of 1.75 bar. The turbine generates power that is transmitted to a centrifugal compressor since the impellers are mounted on the same shaft. The turbine has been chosen to run the system - rather than an electric motor - due to the higher temperature this system can withstand.

The centrifugal compressor plays a crucial role in the CTU. It receives syngas at an inlet temperature of 350 °C and a pressure of 0.81 bar and compresses it at a pressure of 1.16 bar and a temperature of 412 °C.

The central part of the CTU assembly hosts the transmission system, which consists of a shaft connecting the compressor and the turbine. The shaft is supported by four gas bearings, two axial and two radial, characterized by extremely small gaps, of the order of 10^{-6} meters (µm). During operation, these gaps are filled with steam and its interaction with the grooves manufactured on the shaft establishes a pressure gradient, ensuring stability during rotation. The housing is injected with water vapor at a temperature of 412 °C and a pressure of 1.25 bar, with a nominal mass flow rate of 8 kg/h. The steam injection serves two primary functions: ensuring the proper conditions for the gas bearings during operation, and removing the heat generated by the gas bearings due to windage losses. The latter helps to flatten out the thermal gradient across the bushing and rotor components, homogenizing the thermal expansions along the shaft axis.

Figure 1.2 shows the mid-plane section view of the CTU and the main components are labeled. Figure 1.3 reports a schematic of the CTU's boundary conditions and how the pressure inside the steam injection chamber can be regulated employing throttling valves.

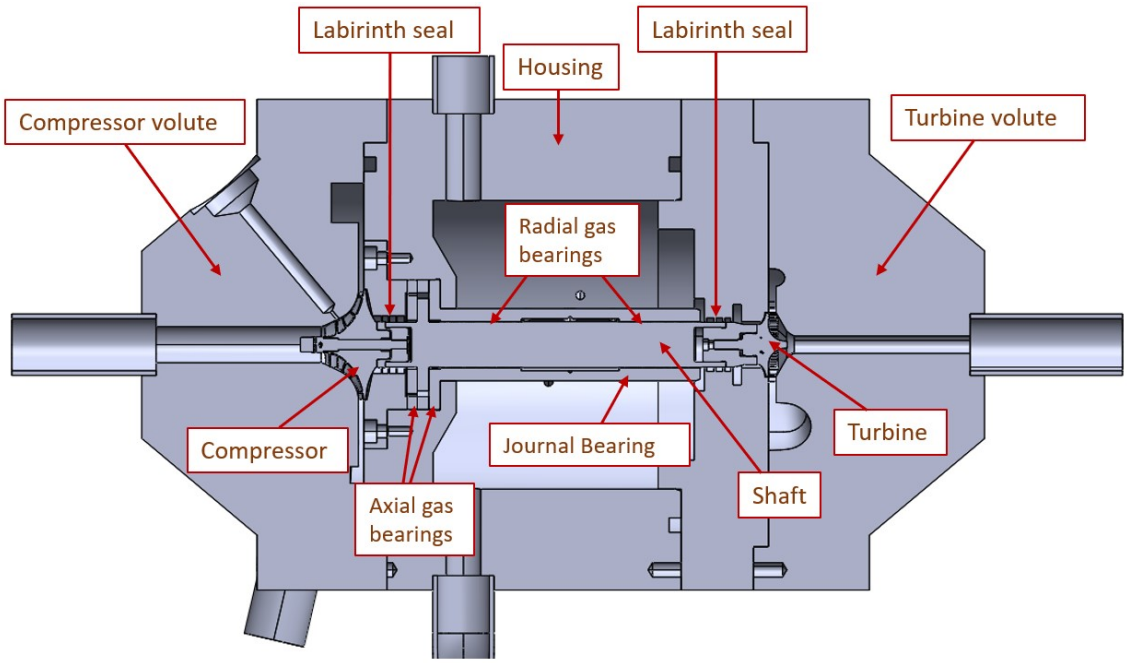

Figure 1.2
CTU section view and main components.

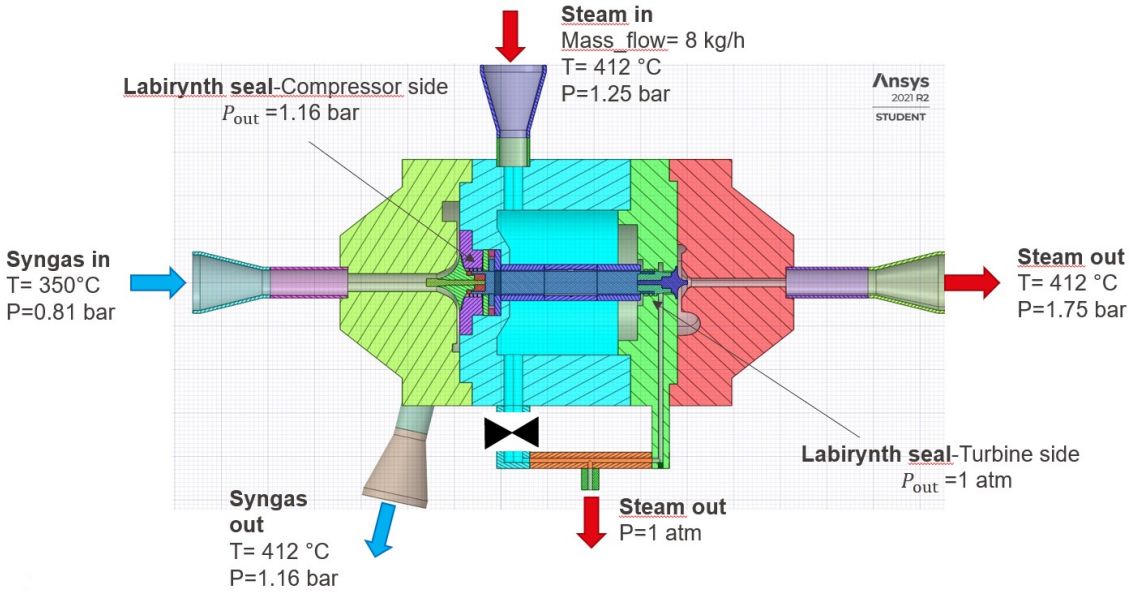

Figure 1.3
CTU section view with flow boundary conditions and location of the lamination valve to control the pressure at the gas bearings.

1.5.2 Materials

The materials used for the CTU are four: Titanium Grade 5 (Ti-6Al-4V), stainless steel 1.4301 (AISI 304) and 1.4571 (AISI 316), and tungsten carbide.

For each component, the materials used are defined in Table 1.1.

Table 1.1
Material of each component.

Steam injection side			
Component	Material	Component	Material
Housing Lid facing Tubine side	Ti Gr5 (Ti-6Al-4V)	Bushing Spacer	WC-CO
Lid facing Compressor side Pipes Kolhers	1.4301 (AISI 304) 1.4571 (AISI 316) 1.4571 (AISI 316)	Rotor SGTB	

Compressor side		**Turbine side**	
Component	Material	Component	Material
Compressor lid	1.4301 (AISI 304)	Turbine lid	Ti Gr5 (Ti-6Al-4V)
Impeller Compressor plug Spinner	Ti Gr5 (Ti-6Al-4V)	Turbine Turbine plug	
Pipes Kolhers	1.4571 (AISI 316)	Pipes Kolhers	1.4571 (AISI 316)

Chapter 2

Fundamentals of Thermo-Fluid Dynamics Modelling

2.1 Heat transfer mechanism

The following section aims to provide the physics behind the heat transfer modes, referring to milestone thermodynamics books [4–6]. The focus is on the principles of heat transfer and how to quantify the amount of energy being transferred per unit of time by using appropriate rate equations.

Generally speaking, heat transfer is thermal energy exchange due to a spatial temperature difference. When a temperature gradient exists in a stationary medium, which may be solid or fluid, the heat transfer mechanism involved is conduction. In contrast, convection happens between a surface and a moving fluid when they are again at different temperatures. The third fundamental mechanism is thermal radiation - which transfers heat in the form of electromagnetic waves emitted from surfaces at a defined temperature.

2.1.1 Conduction

Conduction is the transfer of energy due to interactions between the particles of matter. Hence, in a solid, conduction may be attributed to atomic activity in the form of lattice vibrations and higher temperatures are associated with higher molecular energies. In the presence of a temperature gradient, energy transfer always occurs in the direction of decreasing temperature.

For heat conduction, the rate equation is known as Fourier's law. Under a 1D assumption, the heat flux per unit area in the x direction can be expressed as

$$q_x = -k\frac{dT(x)}{dx} \tag{2.1}$$

in which $T(x)$ is the 1D scalar temperature field in [K], and k represents the thermal conductivity, measured in $[\mathrm{W\,m^{-1}\,K^{-1}}]$. The thermal conductivity represents an intrinsic property of the material and for isotropic ones, as in the case of metals, is independent of the direction of heat transfer, hence $k_x = k_y = k_z = k$. Moreover, It can be deduced that, for a fixed temperature gradient, the conduction heat flux is directly proportional to the thermal conductivity. This law is phenomenological, meaning that it is developed from observed phenomena rather than being derived

from principles. Finally, the minus sign is necessary because heat is always transferred in the direction of decreasing temperature.

2.1.2 Convection

Convective heat transfer is made out of two mechanisms: conduction due to random molecular motion and the advection phenomena - which represent the macroscopic energy transfer by the bulk motion of the fluid as aggregates of molecules. Since the molecules in the aggregate retain their random motion, the total heat transfer is due to a combination of conduction and advection contributions.

Convection heat transfer may be classified according to the nature of the flow. It falls under forced convection when the flow is caused by external means, such as by a fan, a pump, or the presence of wind. In contrast, for natural convection, the flow is induced by buoyancy forces, which are due to density differences caused by temperature variations in the fluid.

Regardless of the nature of the convection mechanism, the appropriate rate equation is named Newton's law and has the form

$$q = h(T_s - T_\infty) \tag{2.2}$$

where q, the convective heat flux per unit area [W/m^2], is proportional to the difference between the surface and the unperturbed fluid temperatures, T_s and T_∞ respectively. The proportionality factor h is called the convective heat transfer coefficient and depends on conditions in the boundary layer, assessed using adimensional numbers that describe the flow state.

To solve the convection problem, it is necessary to estimate the heat transfer coefficient h, which is a non-trivial target, by exploiting proper correlations which are discussed in more detail in a dedicated section.

2.1.3 Radiation

Thermal radiation is energy emitted by matter that is at a non-zero absolute temperature. Regardless of the form of matter, the emission is attributed to changes in the electron configurations of atoms or molecules. Additionally, the energy of the radiation field is transported by electromagnetic waves and photons.

While the transfer of energy by conduction or convection requires the presence of a material medium, radiation does not, and it occurs most efficiently in vacuum. Naming the surface emissive power E as the energy released per unit area in [W/m^2], the upper limit for the emissive power is dictated by the Stefan–Boltzmann law as

$$E_b = \sigma T_s^4 \tag{2.3}$$

where T_s is the absolute temperature of the surface [K] and σ is the Stefan-Boltzmann constant with value 5.67e-8 [W/m^{2}K^4]. In other words, equation (2.3) represents the

emitted energy of a black body at a defined temperature, which is the upper threshold of transmissible energy through radiation. Accordingly, the heat flux emitted by a real surface can be expressed as

$$E = \epsilon \sigma T_s^4 \tag{2.4}$$

where ϵ is the emissivity [-], a radiative property of the surface. It ranges between 0 and 1 and it is a way of measuring how efficiently a surface emits energy.

Radiation may also be incident on a surface from its surroundings and it may be partially absorbed, thereby increasing the thermal energy of the material. The rate at which radiant energy is absorbed from the surroundings per unit area is

$$G_{abs} = \alpha G \tag{2.5}$$

with α being the absorptivity that ranges between 0 and 1.

Combining (2.4) and (2.5) one can state that the total heat flux per unit area emitted by radiation can be expressed as

$$q_{rad} = E - G_{abs} = \epsilon \sigma T_s^4 - \alpha G \tag{2.6}$$

2.2 Fluid flow between concentric rotating cylinders

This section provides insight into the flow field that develops within two rotating cylinders [7]. This will help in understanding the heat transfer and viscous windage loss models in the next sections.

First of all, a classification of the flow fields that may occur within two concentric rotating cylinders is reported. Taylor [8] was the first author who analyzed this phenomenon with a ground-breaking paper in the development of hydrodynamic stability theory and demonstrated the no-slip boundary condition. In particular, the study showed that above a critical speed of rotation, the laminar Couette flow breaks down into a flow consisting of pairs of three-dimensional ring-shaped vortexes. In more recent papers Kaye and Elgar [9], experiments using hot wire anemometry and flow visualization were performed, showing four flow regimes:

1. **Purely laminar flow**, well known as Couette flow. The flow field generated by the rotation of one delimiting cylinder is steady and laminar and it is driven by viscous drag force acting on the fluid. The streamlines are annular and centered on the rotation axis.

2. **Laminar flow with Taylor vortices**. Once the critical rotation speed noted by Taylor [8] is exceeded, the flow presents instabilities, structured in a toroidal-shaped form and known as Taylor vortices. They are counter-rotative and

associated in pairs (Figure 2.1). The vortices have a toroidal shape around the rotational axis (Figure 2.1 (b)).

3. **Turbulent flow with vortices**. After the Taylor number exceeds a second critical threshold, the Taylor vortices boundaries are no longer perpendicular to the cylindrical axis, but rather present undulations due to the presence of an azimuth wave regime denoted as wavy mode (Figure 2.2). The azimuthal direction is the one that - in cylindrical coordinates - follows the angular coordinate with respect to the axis of the cylinder.

4. **Turbulent flow**. As the rotation speeds continue to rise after the disappearance of azimuthal waves, random fluctuations come to progressively dominate the flow.

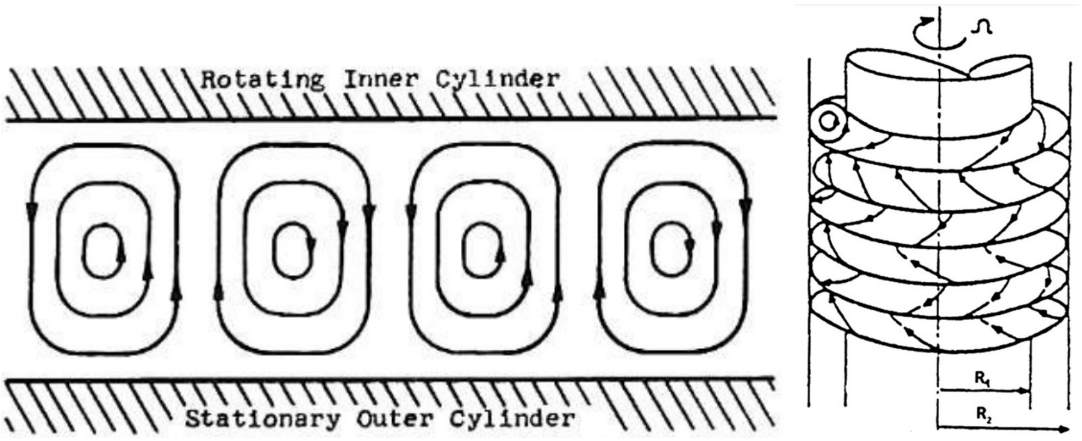

(a) **(b)**

Figure 2.1
Taylor vortices with detail on a vortices cross-section [10] (a) and an overview of the 3D flow field [11] (b).

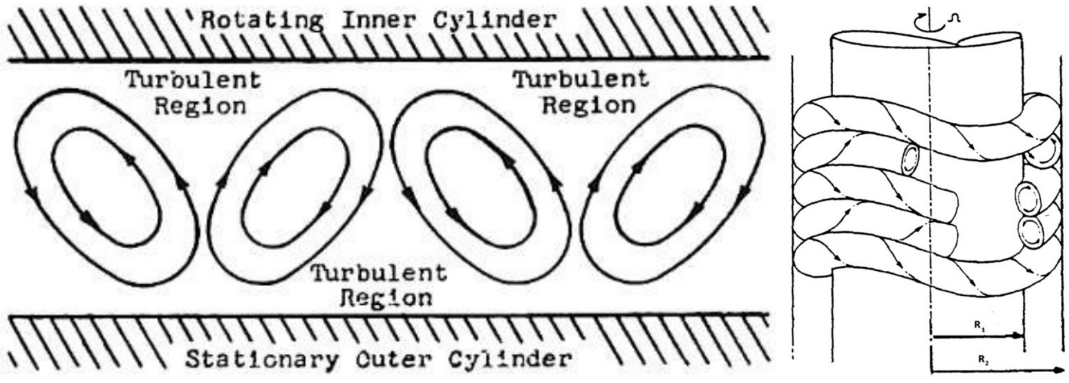

(a) **(b)**

Figure 2.2
Wavy mode characterized by an azimuthal wave regime with detail on a vortices cross-section [10] (a) and an overview of the 3D flow field [11] (b).

A fundamental difference between wavy vortex flow and toroidal vortex flow is that a significant portion of the fluid is transferred from one vortex to another for wavy vortices, whereas toroidal vortices are essentially closed cells [12]. This difference can be seen from Particle Image Velocimetry (PIV) images in Figure 2.3 (a) and Figure 2.4 (a).

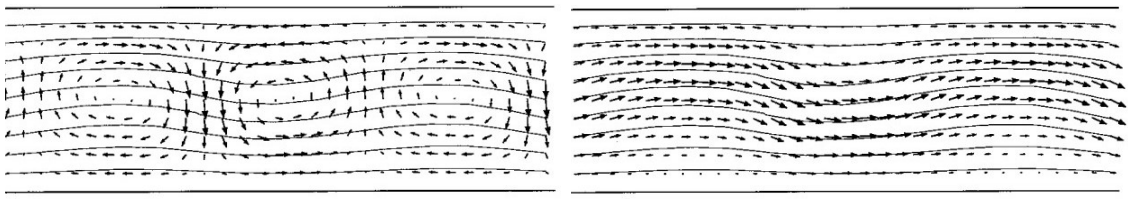

(a) **(b)**

Figure 2.3

Velocity contours of a time series for non-wavy, toroidal, laminar vortex flow (Taylor-Couette) at Ta=123 and axial Re=5.3. The upper line in each frame is the rotating inner cylinder; the lower line is the stationary outer cylinder. (a) Velocity field with the axial velocity profile removed, (b) velocity field including the axial velocity profile [12].

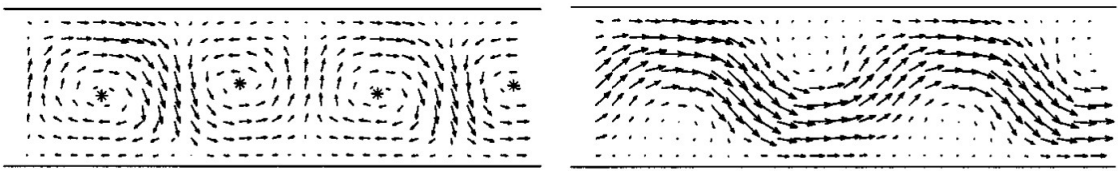

(a) **(b)**

Figure 2.4

Velocity contours of a time series for wavy toroidal vortex flow at Ta=139 and axial Re=5. The upper line in each frame is the rotating inner cylinder; the lower line is the stationary outer cylinder. (a) Velocity field with the axial velocity profile removed, (b) velocity field including the axial velocity profile [12].

The axial flow superposition impact has been analyzed by [12] (Figure 2.3 (b) and Figure 2.4 (b)) as well as by several other authors [13] [14] [15]. In particular, [12] performed experiments using PIV to see the effects. In general, two main influences on the velocity field are experienced:

- Regardless of the flow regime, either Taylor-Couette or wavy flow, at a certain axial Reynolds number the vortices swap from a toroidal to a helical shape around the cylinder rotational axis, leading to an axial translation of them.
- Regardless of the flow regime, the superposition of the axial flow causes the velocity vectors to wind around the vortices, with a so-called winding flow.

At higher Taylor numbers and axial Reynolds numbers the flow gives way to random wavy vortex flow. This flow is characterized by wavy vortices that change shape rapidly, may be helical or toroidal, and often display dislocations where two vortex pairs on one side of the cylinder appears to merge into a single vortex pair on the

the opposite side of the cylinder [12]. The velocity vector fields shown in Figure 2.5 depict the random nature of the flow.

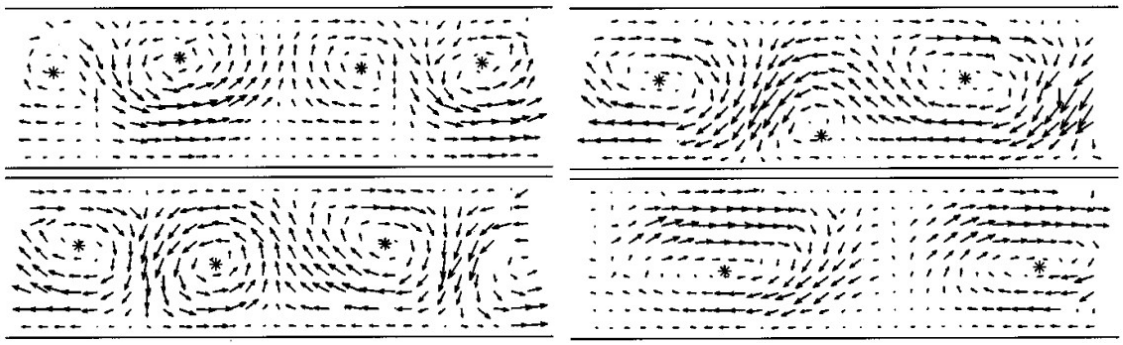

Figure 2.5
Velocity contours of a time series for random wavy vortex at Ta=215 and axial Re=23.2. The upper line in each frame is the rotating inner cylinder; the lower line is the stationary outer cylinder [12].

2.3 Correlations for heat transfer

Although the convective heat transfer equation (2.2) is simple, defining the heat transfer coefficient h can be a challenging task. It depends on several aspects such as the fluid flow conditions, fluid properties, and solid surface geometries delimiting the fluid flow. The state-of-the-art literature can provide heat transfer correlation for a broad range of conditions. However, errors within 30% may occur, the reason why numerical or experimental confirmations should be run in parallel.

All the correlations aim to provide an estimation of the Nusselt number. In the case of natural convection, the Nusselt is a function of the adimensional numbers Grashof and Prandtl as

$$Nu = f(Pr, Gr) \tag{2.7}$$

where the Grashof number (Gr) indicates the ratio of the buoyancy force to the viscous force acting on a fluid and it is used to determine the importance of natural convection in the case under study. The Prandtl number (Pr) is used in fluid mechanics and heat transfer to characterize the relative importance of momentum diffusion to thermal diffusion in a fluid, and it depends only on the thermo-mechanical properties of the fluid.

On the other side, when forced convection is involved, the correlations are of the type

$$Nu = f(Pr, Re) \tag{2.8}$$

where the Reynolds number (Re) is a dimensionless parameter used in fluid mechanics

to characterize the flow regime of a fluid, whether it is laminar, transitional, or turbulent, and indicates the ratio of inertial forces to viscous forces in a fluid flow.

The aforementioned adimensional number may be computed as follows:

$$Gr = \frac{g\beta(T_s - T_\infty)L^3}{\nu} \tag{2.9}$$

$$Pr = \frac{c_p\mu}{k} = \frac{\nu}{\alpha} \tag{2.10}$$

$$Re = \frac{\rho v L}{\mu} \tag{2.11}$$

where g is the gravitational acceleration in [m/s^2], β is the volumetric coefficient of thermal expansion of the fluid in [K^{-1}], T_s is the surface temperature in [K], T_∞ is the unperturbed fluid temperature in [K], L is the characteristic length in [m], ν is the kinematic viscosity in [m^2/s], c_p is the specific heat of the material in [J kg^{-1} K^{-1}], μ is the dynamic viscosity of the fluid in [Pa s], k is the thermal conductivity of the material in [W m^{-1} K^{-1}], α is the thermal diffusivity in [m s], ρ is the density of the material in [kg/m^3] and v the flow velocity in [m s^{-1}].

2.3.1 Horizontal cylinder

This correlation has been found in [16] and it gives the procedure to evaluate the heat transfer coefficient for a horizontal cylinder immersed in ambient air, meaning that the convection occurring between the ambient fluid and the solid part can be classified as natural. First of all, it is necessary to evaluate the adimensional Prandtl number using the equation (2.10). The thermal diffusivity α of the fluid is computed as

$$\alpha = \frac{k}{\rho c_p} \tag{2.12}$$

where ρ is the density of the material in [kg/m^3] and k is the thermal conductivity of the material in [W m^{-1} K^{-1}]. Considering the fluid's isobaric thermal expansion β for an ideal gas such as

$$\beta = \frac{1}{T_\infty} \tag{2.13}$$

being T_∞ the undisturbed ambient temperature in [K]. The dimensionless Rayleigh number Ra is a way of combining the Gr and Pr numbers as

$$Ra := Gr \cdot Pr = \frac{\rho g\beta(T_s - T_\infty)D^3}{\alpha\mu} \tag{2.14}$$

and gives the ratio between thermal transport via convection and via diffusion. In equation (2.14), D is the characteristic length of the thermal problem in [m], in this case, represented by the diameter of the cylinder.

Finally, the Nusselt number can be computed as

$$Nu = 0.36 + \frac{(0.518Ra^{0.25})}{\left[(1 + (\frac{0.559}{Pr})^{\frac{9}{16}})\right]^{\frac{4}{9}}} \tag{2.15}$$

and it follows that the heat transfer coefficient measured in [W/K/m^2] can be evaluated as

$$h = \frac{Nu \cdot k}{D} \tag{2.16}$$

2.3.2 Heat transfer between concentric rotating cylinders

Turbomachinery is often characterized by small gaps for cooling purposes (Figure 2.6) or dynamic stability (Figure 2.7), such as in the case of gas-lubricated bearings. Two different cases of interest are reported: a correlation that neglects the axial flow - meaning that the advection is not considered in the gap - and one that considers it (Nerg, Rilla and Pyrhonen [17]).

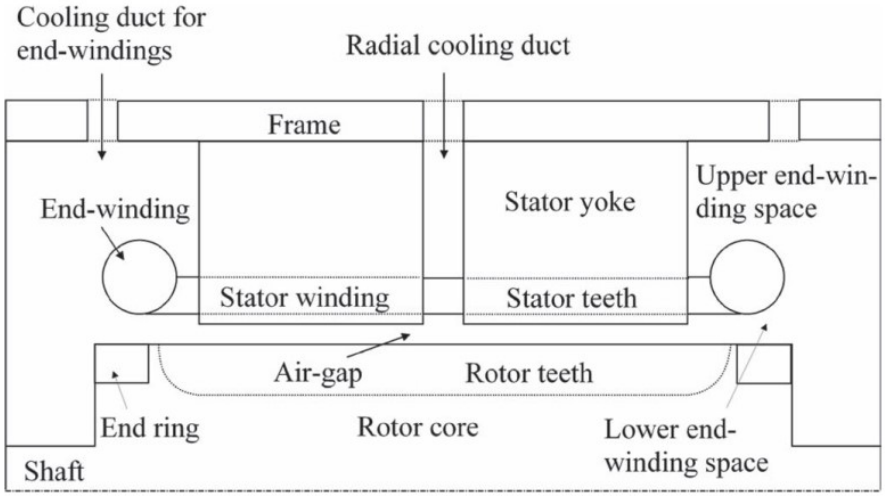

Figure 2.6
Cooling pattern of the analyzed machine in [17]: a three-phase two-pole 430-kW 170-Hz solid-rotor induction.

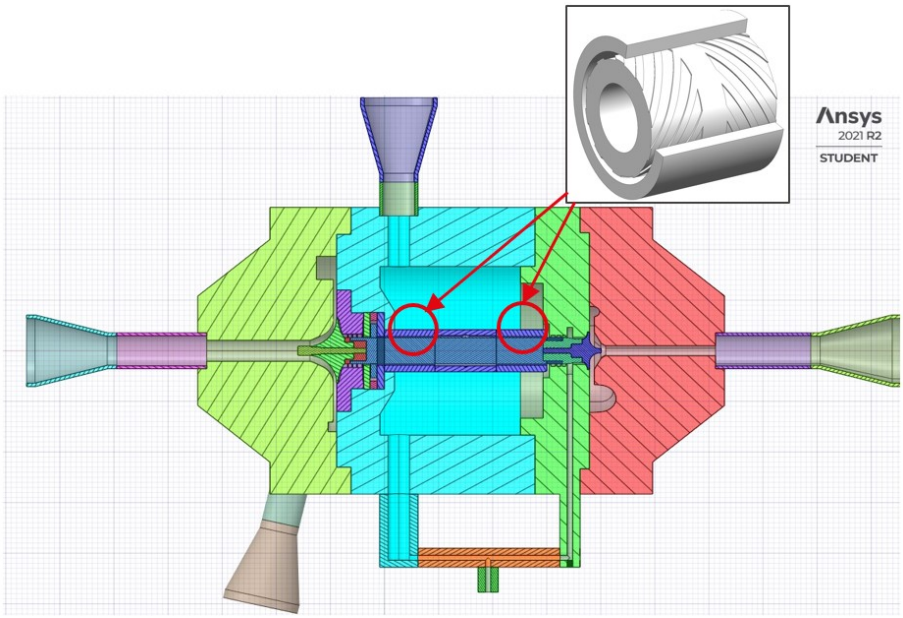

Figure 2.7
Detail on gap characterizing a radial gas bearing (in particular a Herringbone Grooved Journal Bearing) for dynamic regards.

In low axial speed, cooling through the air-gap region is not as effective as in high-speed ones. Therefore, it is appropriate to assume that the main heat transfer path is in the radial direction, thus neglecting advection. With these hypotheses, heat transfer in the air gap can be calculated from the Taylor number - an adimensional number used in fluid dynamics to compare centrifugal and viscous forces - is defined as

$$Ta = \frac{\rho^2 \omega^2 r_m \delta^3}{\mu^2} \tag{2.17}$$

where ω is the angular velocity of the rotor in $[\mathrm{rad\,s^{-1}}]$, δ is the radial length of the air gap and r_m is the average of the stator and rotor radii [m] . To fix the Taylor–Couette flow for the corresponding air-gap length and rotor radius, a modified Taylor number Ta_m is preferred

$$F_g = \frac{\pi^4 \left[\frac{2r_m - 2.304\delta}{2r_m - \delta}\right]}{1697 \left[0.0056 + 0.0571 \left(\frac{2r_m - 2.304\delta}{2r_m - \delta}\right)^2\right] \left[1 - \frac{\delta}{2r_m}\right]} \tag{2.18}$$

$$Ta_m = \frac{Ta}{F_g} \tag{2.19}$$

Finally, the Nusselt number can be evaluated according to the flow regime

$$Nu = \begin{cases} 2 & Ta_m \leq 1700, \text{Laminar} \\ 0.128 Ta_m^{0.367} & 1700 \leq Ta_{fg} \leq 10^3, \text{Transition} \\ 0.409 Ta_m^{0.241} & Ta_{fg} \geq 10^3, \text{Turbulent} \end{cases} \tag{2.20}$$

The concept of the Taylor number related to the fluid flow profile developed in between the two concentric cylinders has been deeply explored in section 2.2. Equations (2.17)–(2.20) are also suggested for low flow axial speeds since they underestimate the convection effect neglecting advection. The convection heat transfer coefficient can now be computed using equation (2.16).

In case the flow axial speed should not be neglected the following correlation is suggested by Nerg, Rilla and Pyrhonen [17]. It is possible to define a reduced velocity in the helical direction - as a relative speed with respect to the shaft - derived from the axial and rotational speed as

$$v_{red} = \sqrt{\left(\frac{\omega R}{2}\right)^2 + v_{axial}^2} \tag{2.21}$$

where R is the outer radius in [m], and v_{axial} is the axial speed of the fluid in [$\mathrm{m\,s^{-1}}$]. The hydraulic diameter d_h and the Reynolds number Re are obtained as

$$d_h = \delta \sqrt{\frac{8}{3}} \tag{2.22}$$

$$Re = \frac{\rho v_{red} d_h}{\mu} \tag{2.23}$$

Finally, one can compute the Nusselt number as

$$Nu = 0.0214 \cdot \left(Re^{0.8} - 100\right) Pr^{0.4} \left[1 + \left(\frac{d_h}{L_\delta}\right)^{0.66}\right] \tag{2.24}$$

where L_δ is the axial length of the air gap in [m]. Finally, the convection heat transfer coefficient can be computed as

$$h = \frac{Nu \cdot \lambda}{d_h} \tag{2.25}$$

It can be noticed that according to the latter correlation, the Nusselt number depends on the rotational and axial flow velocities. However, according to Seghir-Ouali et al. [18], for high rotational speeds, the heat transfer rate is governed by rotation and the axial flow only slightly influences the internal convective heat transfer. Moreover, M. Kuosa [19] proved that the equation 2.21 of the reduced velocity - based on

trigonometry - and the assumption that the velocity of the gas is one-half of the peripheral speed of the rotor is a bad assumption. Additionally, the latter relation is suggested for $10^4 < Re < 10^6$ [19] which is not the case for radial gas bearings. Thus, the first correlation, i.e. the one that neglects the axial flow, will be applied.

2.3.3 Disk

Referring to Northrop and Owen [20], the heat transfer coefficient for a free-rotating disk - hence a disk that rotates in a free volume - can be computed with the following set of equations:

$$Re_\phi = \frac{\rho \omega R^2}{\mu} \tag{2.26}$$

$$Nu_{avg} = 0.0151 Re_\phi^{0.8} \tag{2.27}$$

$$h = \frac{Nu_{avg} k}{R} \tag{2.28}$$

The heat transfer coefficient for axial airgaps, which may correspond to axial thrust bearings or impeller backfaces is estimated according to [21] as

$$C = \frac{0.014 \rho^{0.8} \omega^{0.8} k}{\mu^{0.8} \delta} \tag{2.29}$$

$$h = \frac{1}{2.6} C \frac{(R_{out}^{2.6} - R_{in}^{2.6})}{(R_{out} - R_{in})} \tag{2.30}$$

in which the involved parameters have been already described in the previous sections concerning heat transfer correlations.

2.3.4 Volute

A common assumption for thermal analysis in small-scale high-speed turbomachinery is to impose fixed temperatures as boundary conditions at the volute walls, equal to the fluid's inlet and outlet temperatures and an average one. This hypothesis relies on the fact that - for high forced flow - the temperature of the fluid and the solid surfaces are close enough.

Regarding the fluid-dynamic analysis, the common assumption is to consider the adiabaticity of the volute walls. However, in the case of small-scale machines, the fluid volume per surface ratio becomes pretty small, leading to wrong compressor/turbine maps under the assumption of adiabaticity.

For a more complete thermal analysis, the heat transfer in the volutes should be modeled, rather than applying Dirichlet boundary conditions. Additionally, the

information about the heat flux derived from the thermal study can be used to adjust the aerodynamic performance of compressors and turbines, removing the strong approximation of adiabaticity in these small-scale machines.

The volute heat transfer correlation requires the gas-to-wall surface and a representative hydraulic diameter to calculate the Re and Nu numbers [22], as described hereafter. Usually, the volute geometry is generated by the logarithmic spiral represented by the Figure 2.8

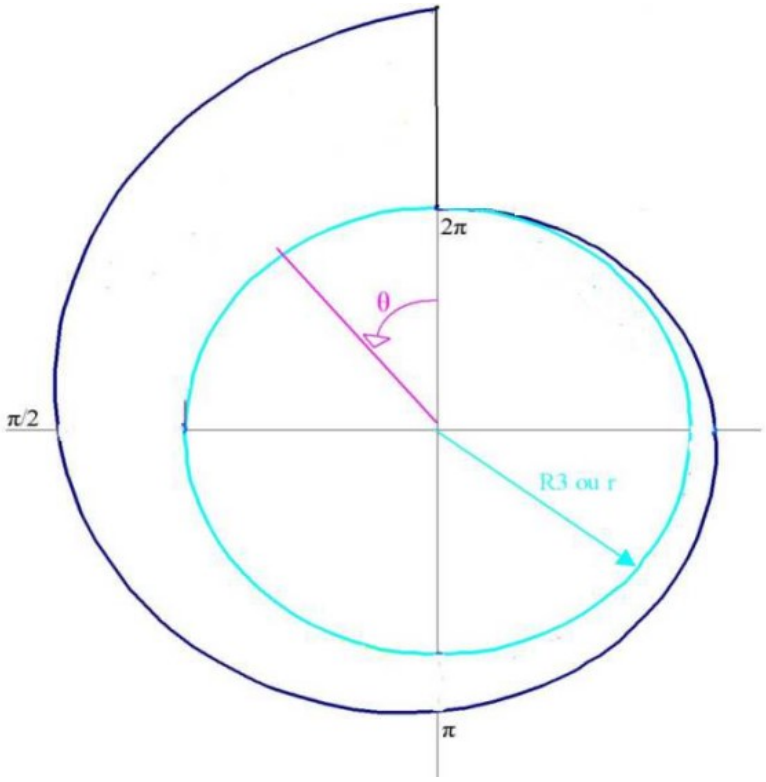

Figure 2.8
Shape of the volute on a cross-section perpendicular to the rotational axis of the impeller [23].

and the radius can be expressed as a function of the logarithmic spiral angle θ [23] as

$$R(\theta) = aexp^{-b\theta} + c \tag{2.31}$$

where $R(0)$, $R(\pi)$, $R(2\pi)$ are the external radius of the volute at $\theta = 0; \pi; 2\pi$, and a, b and c are constant real numbers depending on the geometry as

$$a = R(0) - c \tag{2.32}$$

$$b = -\frac{1}{2\pi} \ln \left[\frac{R(2\pi) - c}{a} \right] \tag{2.33}$$

$$c = \frac{R(2\pi)R(0) - R^2(\pi)}{R(2\pi) + R(0) - 2R(\pi)} \tag{2.34}$$

The length of the elementary spiral arc is described as

$$dL_{arc}(\theta) = \sqrt{\left(\frac{\partial R(\theta)}{\partial \theta}\right)^2 + R(\theta)^2 d\theta} \tag{2.35}$$

and substituting equation (2.31) one can obtain

$$dL_{arc}(\theta) = \sqrt{a^2 b^2 \exp^{-2b\theta} + \left(a \exp^{-b\theta} + c\right) d\theta} \tag{2.36}$$

If the volute cross-section perimeter $p(\theta)$ can be described analytically, then the wall-fluid contact area is

$$A_{vol} = \int_0^{2\pi} p(\theta) dL_{arc}(\theta) \tag{2.37}$$

For instance, [23] derives analytically the formulation of $p(\theta$ in the case the volute's flow section has a trapezoidal shape, but it is not reported herein. The above description of the analytical equations describing the main geometric parameters of interest of the volute is helpful in a preliminary design of it, while once the design has been already performed - as in the case of this research - A_{vol} may be easily obtained from the CAD model.

Finally, the Nusselt number in the volute can be evaluated using the Dittus-Boelter correlation for forced convection [3] as

$$Nu_{turb} = 0.023 \cdot Re_{\overline{D}}^{0.8} \cdot Pr^{0.4} \tag{2.38}$$

where the mean volute hydraulic diameter $\overline{D}_h$, the Reynolds (Re) and Prandtl (Pr) numbers are evaluated as

$$\overline{D}_h = \frac{A_{vol}}{L_{arc}} \tag{2.39}$$

$$Re_{\overline{D}} = \frac{\dot{m} \cdot \overline{D}_h}{\mu \cdot \overline{S}} \tag{2.40}$$

$$Pr = \frac{\mu c_p}{\lambda} \tag{2.41}$$

where $\overline{S}$ is the volute cross-section at the mean volute radius $\overline{R}$ found from $R(0)$ and $R(2\pi)$.

2.4 Thermal load

Rotating machines are subjected to the presence of thermal loads that must be integrated into the thermal model. They may have different origins such as heat generation by the Joule effect inside electric motors, heat generation by the interaction between a viscous fluid and rotating components, the windage losses, or the presence of a generic heat source.

In the case under study, the thermal loads involved are the windage losses. The most significant ones are generated in the axial and radial bearings since the rotational speed is very high while the gaps are of the order of micrometers. The general expression for the windage losses generated by a spinning rotor - that can be derived analytically [24] - is

$$Q_{w-rotor} = C_f \pi \rho \omega^3 r_o^4 L \tag{2.42}$$

where L is the rotor length in [m], r_o is the outer radius of the shaft in [m], and C_f is the skin friction coefficient [-] that has to be evaluated according to different cases.

For a rotating disk, the analytical equation for the windage losses becomes [24]:

$$Q_{w-disk} = C_f \frac{\pi}{2} \rho \omega^3 r_o^5 \tag{2.43}$$

2.4.1 Herringbone Grooved Journal Bearing (HGJB)

Schiffmann [2] derived a windage loss equation suitable for the Herringbone Grooved Journal Bearings (HGJB - radial bearings) that takes into account the groove depth and width of the radial bearings. A cut and top views of a typical HGJB are reported in Figure 2.9.

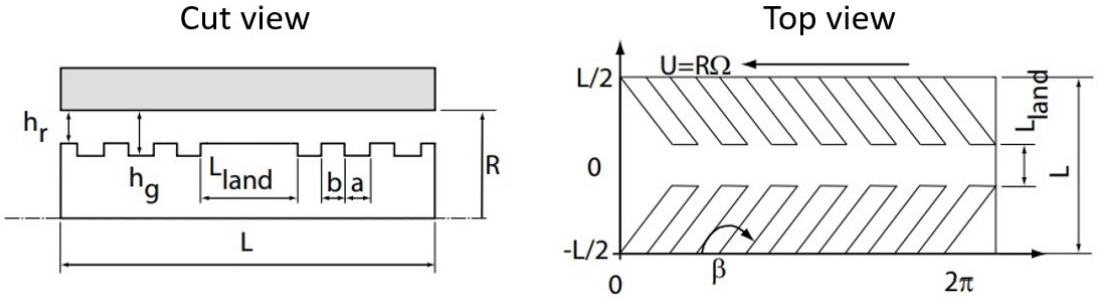

Figure 2.9
HGJB cut and top views and main geometrical parameters identification according to [2].

To do so, Schiffmann [2] started with the equation (2.42) for viscous heat generation in plain bearings and substituted the skin friction coefficient C_f with the assumption of laminar flow in the gas bearing gap. The Reynolds number is low due to a very small characteristic length. The equation obtained is:

$$Q_{w-rotor} = 2\pi \frac{R^3 \omega^2}{h_r} \mu L \tag{2.44}$$

and proposed the following modifications:

$$Q_{wHGJB} = 2\pi R^3 \omega^2 \left[\frac{\gamma\alpha}{h_g} + \frac{1-\gamma\alpha}{h_r} \right] \mu L \tag{2.45}$$

where α is the groove width ratio [-] and γ is the groove length ratio [-], defined as

$$\alpha = \frac{a}{a+b} \tag{2.46}$$

$$\gamma = \frac{L - L_{land}}{L} \tag{2.47}$$

The geometrical parameters used in the equations (2.44)-(2.47) are shown in Figure 2.9.

Other authors [24] proposed a different approach, based on generalized expressions of the friction loss, instead of using a laminar assumption. The losses were divided into three contributes: a loss over the grooved fraction of the grooved surface, a loss over the ungrooved fraction of the grooved surface, and a loss over the smooth surface in between the grooved surfaces

$$\begin{aligned} Q_{wHGJB} = \Bigg[& C_f \left(\frac{\rho\omega r_o^2}{\mu}, \frac{c+h_g}{r_o} \right) \pi\rho\omega^3 r_o^4 l\alpha\gamma \\ & + C_f \left(\frac{\rho\omega r_o^2}{\mu}, \frac{c}{r_o} \right) \pi\rho\omega^3 r_o^4 l(1-\alpha\gamma) \Bigg] \end{aligned} \tag{2.48}$$

For the geometrical parameters, in this case, refer to Figure 2.10

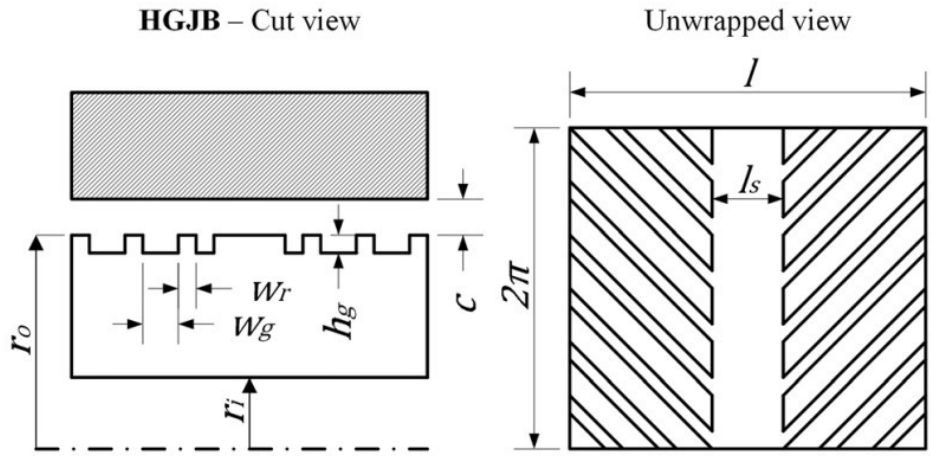

Figure 2.10
HGJB cut and top views and main geometrical parameters identification according to [24].

To compute the skin friction coefficients, one has to choose among different conditions. The common approach in the literature for the skin friction coefficient is to provide empirical expressions, valid in a specific range of non-dimensional numbers.

A non-dimensional group relevant to fluid dynamics is the Taylor number, which provides an indication of the relative effects of inertial forces and viscosity for an annulus, with rotation of one or both of the cylindrical delimiting surfaces [25]. According to [24] can be computed as

$$Ta = \frac{\rho \omega r_o^2}{\mu} \left(\frac{c}{r_o} \right)^{3/2} = Re \cdot c_r^{3/2} \tag{2.49}$$

where Re is the Reynolds number and c_r is the clearance ratio as

$$Re = \frac{\rho \omega r_o^2}{\mu} \tag{2.50}$$

$$c_r = \frac{c}{r_o} \tag{2.51}$$

In the case of concentric cylinders with the inner one spinning, assuming a laminar flow regime, without radial flow, with a linear velocity profile, and with no-slip boundary conditions, the analytically derivable equation - obtained in [24] - is

$$C_f = \frac{2}{Re} \left(1 + \frac{1}{c_r} \right) \tag{2.52}$$

In other words, the flow field for which equation (2.52) is consistent is the Couette one.

However, if either the clearance ratio is too large or the rotational speed increases too much, the linear velocity profile is not valid anymore. Instead, a Taylor-Couette velocity profile develops. The resulting skin friction coefficient is modeled as

$$C_f = \frac{4}{Re} \frac{(1+c_r)^2}{(1+c_r)^2 - 1} \tag{2.53}$$

For clearances ratios below 0.02, there is less than 1% difference between Equation 2.52 and Equation 2.53, while above 0.02 the difference starts to become important (Figure 2.11) [24].

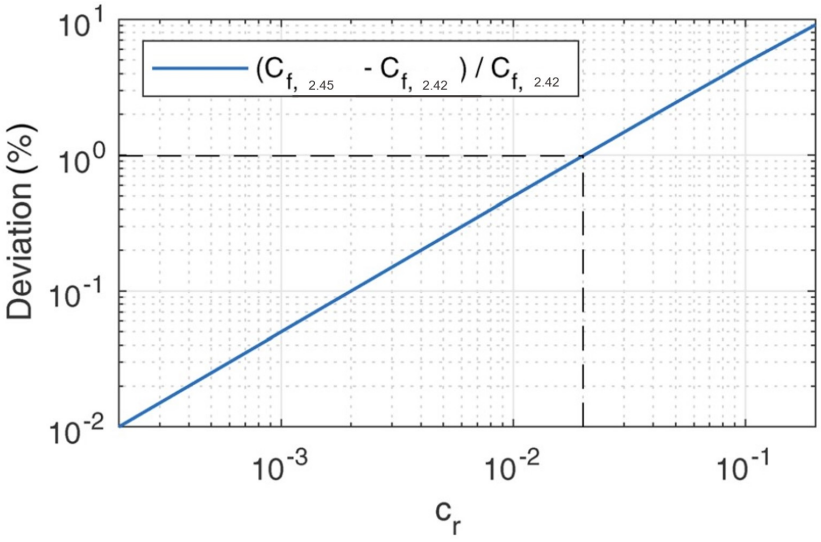

Figure 2.11

Error by using the skin friction for Couette flow or linear velocity profile (equation 2.52) or for Taylor–Couette flow (equation 2.53) [24].

One can conclude that the most general expression among the two is Equation 2.53, valid for either small or big gaps.

So far, the equations for the skin friction coefficient for Couette and Taylor-Couette flows have been defined, which are both laminar, as equations 2.52 and 2.53, respectively. Beyond a threshold defined by the Taylor number, the flow remains steady but axisymmetric toroidal vortices start to grow in the annulus - thus the flow is no longer azimuthal. Increasing the Ta number, there is a progression of instabilities characterized by wavy vortices (refer to section 2.2 for more details). The flow becomes unsteady, and above a Taylor number of 400 the flow results in being fully turbulent [24] (Figure 2.12).

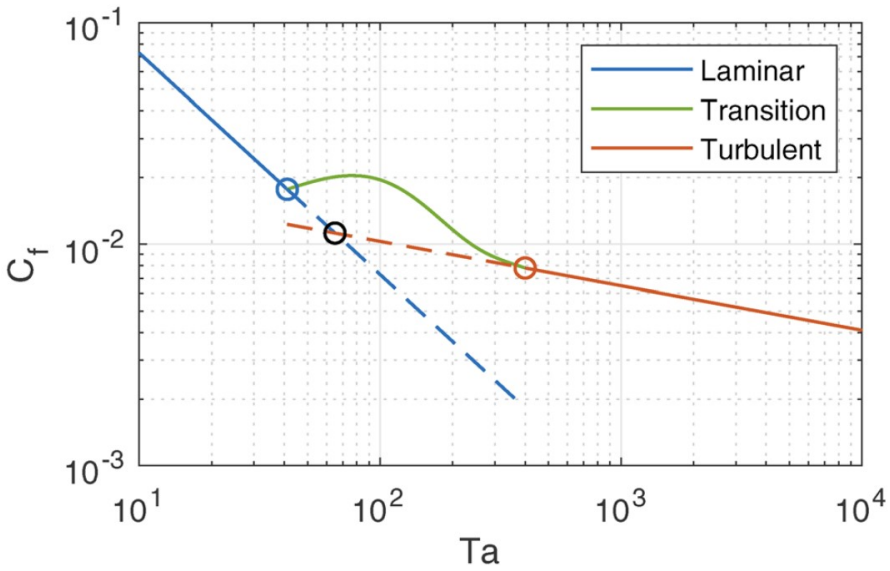

Figure 2.12
Skin friction coefficient as a function of the Taylor number [24].

For a small clearance ratio, the critical Taylor number can be computed as

$$\begin{cases} Ta_{cr} = \pi^2 \left(\frac{2+c_r}{2S}\right)^{1/2} \\ S = 0.0571(1 - 0.652 \cdot c_r) + 0.00056(1 - 0.652 c_r)^{-1} \end{cases} \tag{2.54}$$

which asymptotically tends to the value 41.1 if the clearance ratio tends to zero (Figure 2.13) [24].

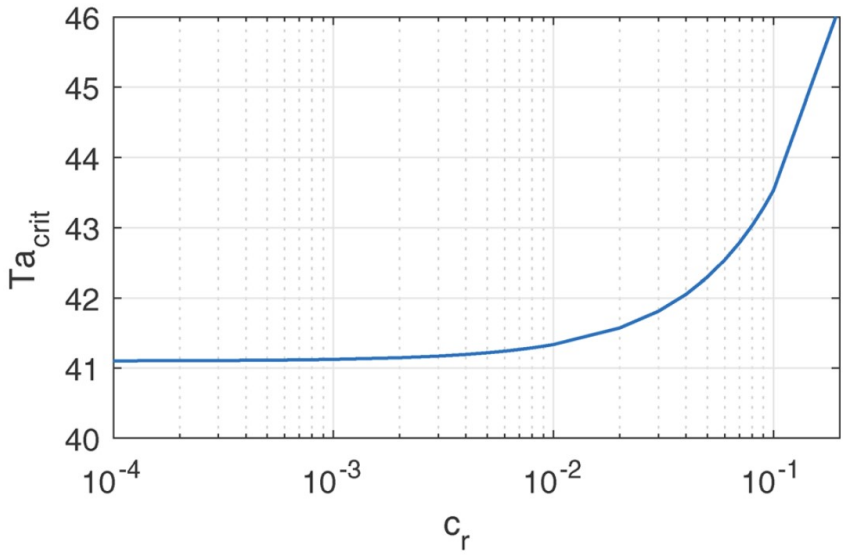

Figure 2.13
Critical Taylor number - which characterizes the onset of the formation of Taylor vortices - as a function of the clearance ratio, according to equation 2.54 [24].

Therefore, in the case of a clearance ratio below 10^{-2} one can assume the Ta_{cr} constant and equal to the asymptotic value.

One of the main models used is the one proposed by Mack [26], which has been applied to estimate windage losses in the air gap of high-speed electrical machines

$$C_f = \begin{cases} \frac{1.8}{Re} c_r^{-1/4} \frac{(1+c_r)^2}{(1+c_r)^2-1} & Ta < 41.3, \text{Laminar} \\ \frac{K}{Ta^{1/5}} & Ta > 400, \text{Fully turbulent} \end{cases} \tag{2.55}$$

and showed good agreement with experimental data when determining the proportionality coefficient K at a $Ta_{critical} = 41.3$ and starting from the laminar flow skin friction coefficient as

$$K = \frac{1.8}{Re_{critical}} c_r^{-1/4} \frac{(1+c_r)^2}{(1+c_r)^2 - 1} \cdot Ta_{critical}^{0.2} \tag{2.56}$$

Due to the not consistency between equation 2.57 and the literature with the definition of the skin friction coefficient in the laminar flow regime equation 2.53, Rosset [24] proposed to modify the equations as

$$C_f = \begin{cases} \frac{4}{Re} \frac{(1+c_r)^2}{(1+c_r)^2-1} & Ta \leq Ta_{cr}, \text{Laminar} \\ \frac{K}{Ta^{1/5}} & Ta > Ta_{cr}, \text{Fully turbulent} \end{cases} \tag{2.57}$$

Where Ta_{cr} has been set to an artificial value of 67, instead of using the theoretical value of 41.1, to better match the experimental results. For what concerns this study, laminar flow always occurs in the flow gaps as will be discussed in the Results section, therefore no special attention to this value was paid.

2.4.2 Spiral Grooved Thrust Bearing (SGTB)

This section aims to condense the most effective approach to evaluate the windage losses for the case of the Spiral Grooved Thrust Bearings (SGTB - axial bearings). Schiffmann [2] proposed the following equation with the same assumptions as for the HGJB

$$Q_{wSGTB} = \mu \frac{\omega^2 \pi}{2} \left[(R_o^4 - R_g^4)(\frac{\alpha}{h_g} + \frac{1-\alpha}{h_r}) + (R_g^4 - R_i^4)\frac{1}{h_r} \right] \tag{2.58}$$

where the geometric parameters can be seen in Figure 2.14.

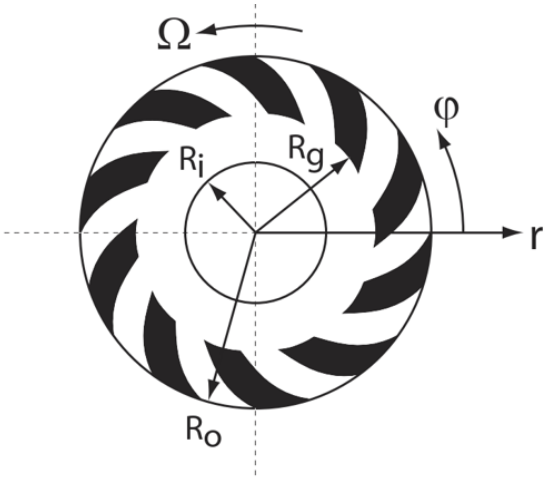

Figure 2.14
SGTB geometrical parameters identification according to [2].

Furthermore, Rosset [24] suggested a model that may take into account different flow regimes for the skin friction coefficient computation. The general windage loss equation proposed is

$$\begin{aligned} Q_{wSGTB} = \Bigg[& C'_f\left(\frac{\rho\omega r_o^2}{\mu}, \frac{c+h_g}{r_o}, \frac{r_s}{r_o}\right)\frac{\pi}{2}\rho\omega^3 r_o^5\alpha \\ & + C'_f\left(\frac{\rho\omega r_o^2}{\mu}, \frac{c}{r_o}, \frac{r_s}{r_o}\right)\frac{\pi}{2}\rho\omega^3 r_o^5(1-\alpha) \\ & + C'_f\left(\frac{\rho\omega r_s^2}{\mu}, \frac{c}{r_s}, \frac{r_i}{r_s}\right)\frac{\pi}{2}\rho\omega^3 r_s^5 \Bigg] \end{aligned} \tag{2.59}$$

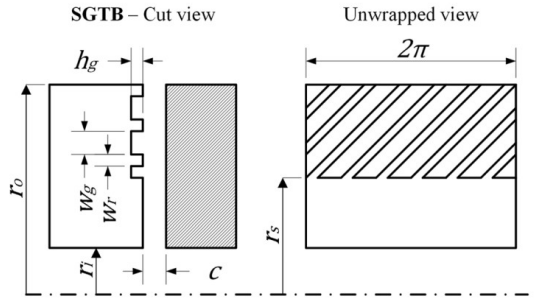

Figure 2.15
SGTB cut and top views and main geometrical parameters identification according to [24].

Considering no axial flow and a linear velocity profile with no-slip boundary conditions in the tangential direction (Couette flow), the skin friction coefficient for a rotating disk is

$$C_f = \frac{1-\lambda^4}{Rec_r} \tag{2.60}$$

Daily and Nece [27] presented a model to evaluate the skin friction coefficient associated with an enclosed rotating disk. Their model was validated based on a large set of experiments in which they identified four flow regimes. A bottleneck is that only a single radius ratio of 0.1 was investigated, thus making the model inappropriate for disks with a large inner radius R_i. Thus, the set of equations proposed by [27] does not take into account R_i:

$$C_f' = \begin{cases} \frac{1}{\mathrm{Re}\, c_r}, & \text{laminar flow, merged boundary layers} \\ \frac{3.7 c_r^{1/10}}{2\pi\, \mathrm{Re}^{1/2}}, & \text{laminar flow, separate boundary layers} \\ \frac{0.08}{2\pi\, \mathrm{Re}^{1/4}\, c_r^{1/6}}, & \text{turbulent flow, merged boundary layers} \\ \frac{0.102 c_r^{1/10}}{2\pi\, \mathrm{Re}^{1/5}}, & \text{turbulent flow, separate boundary layers} \end{cases} \tag{2.61}$$

Starting from that, Rosset [24] proposed to integrate into the model the effect of the inner diameter - differentiating the four flow regimes - as:

$$C_f' = \begin{cases} \frac{1-\lambda^4}{\mathrm{Re}\, c_r}, & \text{laminar flow, merged boundary layers} \\ \frac{3.7 c_r^{1/10}\left(1-\lambda^{39/10}\right)}{2\pi\, \mathrm{Re}^{1/2}}, & \text{laminar flow, separate boundary layers} \\ \frac{0.08\left(1-\lambda^{14/3}\right)}{2\pi\, \mathrm{Re}^{1/4}\, c_r^{1/6}}, & \text{turbulent flow, merged boundary layers} \\ \frac{0.102 c_r^{1/10}\left(1-\lambda^{9/2}\right)}{2\pi\, \mathrm{Re}^{1/5}}, & \text{turbulent flow, separate boundary layers} \end{cases} \tag{2.62}$$

Chapter 3

1D Modelling

3.1 Simscape™

3.1.1 Overview of the physical network approach

Simscape™ is a set of block libraries and simulation features for modeling physical systems in the Simulink environment. Differently from Simulink, it employs the Physical Network approach and is suited to simulating systems that consist of real physical components, such as pipes, solids components, or pumps. Since Simulink blocks represent basic mathematical operations, connecting them results in a diagram that is equivalent to the mathematical model of the system under analysis. Further, Simscape - according to the physical network approach - allows the creation of a network in which any functional element interacts with each other by exchanging energy and mass through their ports. In other words, Simscape diagrams mimic the physical system layout, rather than be just a mathematical model.

Additionally, it is not necessary to specify flow directions when connecting Simscape blocks. The connection ports are non-directional and they model physical connections between elements. The Physical Network approach automatically resolves all the traditional issues with the physical variables, directionality, and so on.

The number of connection ports for each element is determined by the number of energy flows it exchanges with other elements in the system, and depends on the level of idealization and discretization of the real problem.

3.1.2 Type of variables

The physical network approach applies - for the 1D networks - the electrical analogy. Thus, one may distinguish two types of variables:

- Through or flow variables - measured with a gauge connected in series to an element - similar to the current in the electrical analogy.
- Across or potential variables - measured with a gauge connected in parallel to an element - similar to the voltage in the electrical analogy.

During the computation - according to the generalized Kirchhoff laws - the potential variables are equalized at the network's nodes, and corresponding flow variables are conserved through the network branches.

The network components between two nodes impose a physical relationship between

potential and flow variables. For thermal networks, the variables are the temperature and heat flow, in which the heat flow is the through variable and the temperature is the across one. For fluid networks, the through variable is the mass flow and the across variable is the pressure.

Each flow variable is characterized by a magnitude and a sign, with the latter depending on the reference orientation. For instance, referring to a block with only two ports as in Figure 3.1, it is characterized by one pair of variables, a through variable and an across variable.

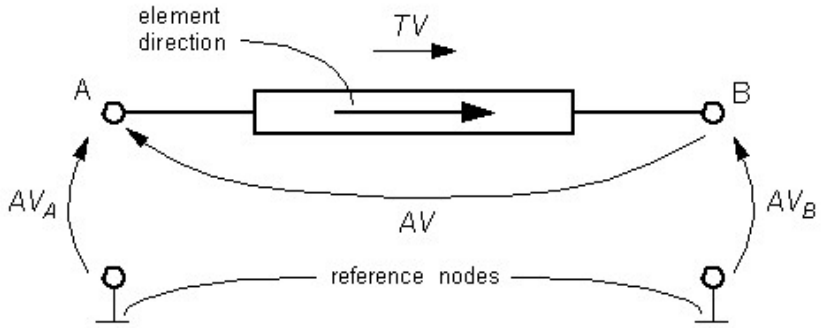

Figure 3.1
Schematics of a Simscape element with two ports [28].

If an element is oriented from port A to port B, it implies that the Through variable (TV) is positive if it flows from A to B, and the Across variable is determined as $AV = AV_A - AV_B$, where AV_A and AV_B are the values of the Across variable AV at ports A and B, respectively.

This approach to the direction of variables provides a simple yet consistent way to determine whether an element is active or passive. Indeed, the product between the across and through variables represents the energy exchanged and is positive if the element consumes energy, and is negative if it provides energy to a system.

In addition, in Simscape there is the possibility to use two types of ports:

- Physical conserving ports - that represent physical connections and relate physical variables.
- Physical signal ports - unidirectional ports that use signals from Simulink as an input for the block.

3.1.3 Differential, differential-algebraic, and algebraic systems

The mathematical representation of a physical system contains ordinary differential equations (ODEs), algebraic equations, or both.

- ODEs govern the rates of change of system variables and contain the time derivatives of the system variables.

- Algebraic equations specify functional constraints among system variables but contain no time derivatives of them.

Hence, it is possible to define three types of systems of equations:

- Without algebraic constraints, the system is differential (ODEs).
- Without ODEs, the system is algebraic.
- With ODEs and algebraic constraints, the system is mixed differential-algebraic (DAEs).

To summarize, a system variable is differential or algebraic, depending on whether or not its time derivative appears in the system equations.

3.1.4 How Simscape simulation works

The flow chart drawn in Figure 3.2 shows the Simscape simulation sequence while simulations are run.

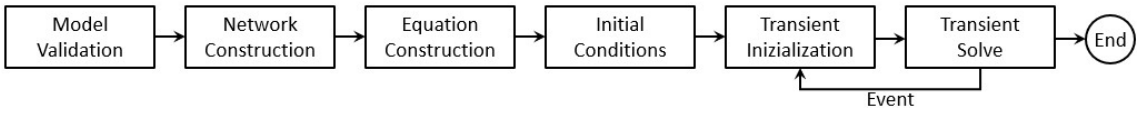

Figure 3.2
Simscape simulation flow chart.

The Simscape solver first validates the model configuration and then checks the data entries from the block dialog boxes according to the defined criteria. After validating the model, the Simscape solver builds the physical network based on the generalized Kirchoff laws. The potential variables are set equal at the nodes while the flow variables are ruled by the conservation laws at the nodes.

Based on the network configuration, the parameter values in the block, and the global parameters defined by the fluid properties, the Simscape solver builds the system of equations for the model. These equations contain system variables of the following types:

- Dynamic — Time derivatives of the variables appear in equations. Dynamic variables add time dependency to the system and require the solver to use numerical integration to compute their values. Dynamic variables can produce either independent or dependent states for simulation.
- Algebraic — Time derivatives of these variables do not appear in equations, thus they appear in algebraic equations. The states of algebraic variables are always dependent on dynamic variables or other algebraic variables.

The solver computes the initial conditions by finding initial values for all the system variables that exactly satisfy all the model equations. It is also possible to affect the initial conditions by specifying the priority and target initial values.

After computing the initial conditions, the Simscape solver performs transient initialization that is needed to fix all dynamic variables and solves for algebraic variables and derivatives of dynamic variables. The goal of transient initialization is to provide a consistent set of initial conditions for the next phase.

Finally, the Simscape solver performs transient solve of the system of equations. In transient solve, continuous differential equations are integrated in time to compute all the variables as a function of time. There are different methods available as the Backward Euler, Trapezoidal Rule, or Partitioning, and the first is the default one. This cycle (Figure 3.2) continues until the end of the simulation which is set by the user defining the simulation time of the physical problem.

3.2 Physical modeling - Existing blocks

This section aims to give an overview of the already existing Simscape blocks that are useful for the case of study, along with the governing equations behind each element.

3.2.1 Constant volume chamber

According to the online reference [29] the Constant Volume Chamber block models mass and energy storage in a gas network, and graphically is represented as in Figure 3.3. The chamber contains a constant volume of gas and it can have up to four flow ports and one thermal port, labeled as H. The first ones are used by the block to exchange mass and energy with the gas network while the thermal port H can exchange heat with the environment at a constant temperature, defined at node H. The exchange of mass and energy with the connected network leads to an evolution in time of its internal pressure and temperature.

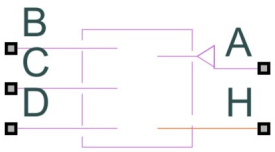

Figure 3.3
Constant volume chamber block in Simscape™ Gas Library.

The mass conservation within the block is ruled by the mass conservation equation and it relates the mass flow rates at the ports to the dynamics of the pressure and temperature of the node as

$$\frac{\partial M}{\partial p}\frac{dp}{dt} + \frac{\partial M}{\partial T}\frac{dT}{dt} = \dot{m_A} + \dot{m_B} + \dot{m_C} + \dot{m_D} \tag{3.1}$$

Energy conservation relates the energy and heat flow rates at the ports to the dynamics of the pressure and temperature of the internal nodes:

$$\frac{\partial U}{\partial p}\frac{dp}{dt} + \frac{\partial U}{\partial T}\frac{dT}{dt} = \dot{\phi_A} + \dot{\phi_B} + \dot{\phi_C} + \dot{\phi_D} + \dot{\phi_H} \tag{3.2}$$

The partial derivatives in equations (3.1) and (3.2) of the mass M and the internal energy U of the gas volume, with respect to pressure and temperature - at constant volume - are evaluated as

$$\frac{\partial M}{\partial p} = V\frac{\rho}{p} \tag{3.3}$$

$$\frac{\partial M}{\partial T} = -V\frac{\rho}{T} \tag{3.4}$$

$$\frac{\partial U}{\partial p} = V\left(\frac{h_v}{ZRT} - 1\right) \tag{3.5}$$

$$\frac{\partial U}{\partial T} = V\rho\left(c_p - \frac{h_v}{T}\right) \tag{3.6}$$

3.2.2 Pipe

The pipe bock simulates the flow in a gas duct and it accounts for friction losses and convective heat transfer with the pipe walls. The pipe contains a constant volume of gas, and the temperature and pressure evolve based on the compressibility and thermal capacity of the gas volume. Chocking might occur in this block but that is not the case in this study.

It is characterized by two flow ports, one inlet, one outlet - and this is one of the main differences with respect to the constant volume chamber. Additionally, the pipe block has one thermal port through which it may exchange thermal power with the surrounding solid surfaces. The graphical representation in Simscape is depicted in Figure 3.4.

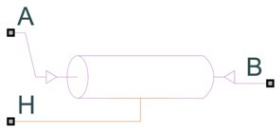

Figure 3.4
Pipe block in Simscape™ Gas Library.

As for the Constant Volume Chamber, the pipe block solves the mass balance (3.1) and the energy balance (3.2) equations.

Two additional equations are solved with respect to the constant volume chamber. One of those is the momentum balance at the two flow ports, which takes into account the pressure drop due to viscous losses as

$$p_A - p_I = \left(\frac{\dot{m}_A}{S}\right)^2 \cdot \left(\frac{1}{\rho_I} - \frac{1}{\rho_A}\right) + \Delta p_{AI} \tag{3.7}$$

$$p_B - p_I = \left(\frac{\dot{m}_B}{S}\right)^2 \cdot \left(\frac{1}{\rho_I} - \frac{1}{\rho_B}\right) + \Delta p_{BI} \tag{3.8}$$

where p is the pressure at the flow ports - A and B - and at the internal node I, ρ is the density at the nodes, S is the cross sectional area of the pipe, Δp_{AI} and Δp_{BI} are pressure losses due to viscous friction.

The heat exchanged with the pipe wall through port H is added to the gas volume at the internal node I via the energy conservation equation. Therefore, the momentum

balances for each half of the pipe are assumed adiabatic processes, and the total enthalpies are conserved as

$$h_A + \frac{1}{2}\left(\frac{\dot{m}_A}{\rho_A S}\right)^2 = h_I + \frac{1}{2}\left(\frac{\dot{m}_A}{\rho_I S}\right)^2 \tag{3.9}$$

$$h_B + \frac{1}{2}\left(\frac{\dot{m}_B}{\rho_B S}\right)^2 = h_I + \frac{1}{2}\left(\frac{\dot{m}_B}{\rho_I S}\right)^2 \tag{3.10}$$

where h is the specific enthalpy at the different nodes.

The pressure losses Δp_{AI} and Δp_{BI} in equations (3.7) and (3.8) depend on the flow regime, the Reynolds numbers for each half of the pipe are defined as

$$Re_A = \frac{|\dot{m}_A| \cdot D_h}{S \cdot \mu_I} \tag{3.11}$$

$$Re_B = \frac{|\dot{m}_B| \cdot D_h}{S \cdot \mu_I} \tag{3.12}$$

Based on the flow regime, the pressure drops are evaluated by exploiting the Darcy friction factor f_{Darcy} according to [30].

For what concerns the heat transfer by convection with the walls, the heat transfer coefficient is computed as

$$h = Nu\frac{k_{avg}}{Dh} \tag{3.13}$$

where k_{avg} is the thermal conductivity evaluated at the average temperature. The Nusselt number Nu depends on the flow regime, for a turbulent flow follows the Gnielinski correlation

$$Nu_{turbulent} = \frac{\frac{f_{Darcy}}{8}(Re_{avg} - 1000)Pr_{avg}}{1 + 12.7\sqrt{\frac{f_{Darcy}}{8}}(Pr_{avg}^{2/3} - 1)} \tag{3.14}$$

where Pr_{avg} is the Prandtl number evaluated at the average temperature and the average Reynolds number is

$$Re_{avg} = \frac{|\dot{m_{avg}}| \cdot D_h}{S\mu_{avg}} \tag{3.15}$$

where μ_{avg} is the dynamic viscosity evaluated at the average temperature.

3.3 Physical modeling - Customized blocks

For assessing the targets of this research, customized blocks are used, based on the work of [3]. They are composed of conduction - or solid blocks - and convection blocks, which apply the correlations explained before.

3.3.1 Conduction block

The conduction blocks are thought of as cylinders that combine two 1D thermal networks - one radial and one axial - and therefore a 2D network is achieved. In Figure 3.5 (a) the schematic of the physical network is shown.

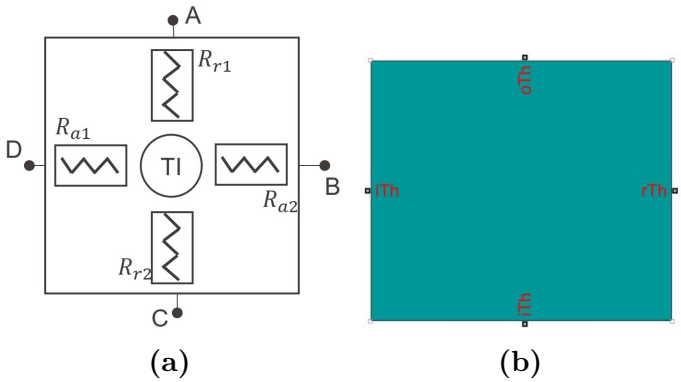

Figure 3.5
Schematic 2D network of the conduction block (a) and Conduction block representation in Simscape (b).

The block is constituted by a thermal inertia (TI) in the middle, which determines the system's dynamic behavior, and from which 4 thermal resistances depart. Two resistances are axial, denoted as R_{a1} and R_{a2}, while two are radial, labelled R_{r1} and R_{r2}. The block has four thermal ports named A, B, C, and D and can be fed with temperature or heat flux boundary conditions. Figure 3.5 (b) shows the graphic representation of the conduction element in Simscape.

The thermal inertia describes the ability of the material to store internal energy and it is ruled by the time-dependent differential equation

$$Q = mc\frac{dT}{dt} \tag{3.16}$$

where Q is the heat flux in [W], m is the mass in [kg], c is the heat capacity in $[\mathrm{J\,kg^{-1}\,K^{-1}}]$, and T is the temperature in [K].

The value of the four thermal resistances can be evaluated with the equations [31]

$$R_{r1} = \frac{1}{4\pi k_r}\left[\frac{2r_o^2 \ln\frac{r_o}{r_i}}{(r_o^2 - r_i^2)} - 1\right] \quad (3.17) \qquad R_{r2} = \frac{1}{4\pi k_r}\left[1 - \frac{2r_i^2 \ln\frac{r_o}{r_i}}{(r_o^2 - r_i^2)}\right] \quad (3.18)$$

$$R_{a1} = \frac{L}{2\pi k_a(r_i^2 - r_o^2)} \quad (3.19) \qquad R_{a1} = \frac{L}{2\pi k_a(r_i^2 - r_o^2)} \quad (3.20)$$

where r_o and r_i are the outer and inner radii of the cylinder in [m], and k_r and k_a are the radial and axial thermal conductivity of the material in $[\mathrm{W\,m^{-1}\,K^{-1}}]$.

If internal heat generation has to be considered, two additional resistances must be added, denoted as R_{3a} R_{3r} in the schematic of Figure 3.6, [32].

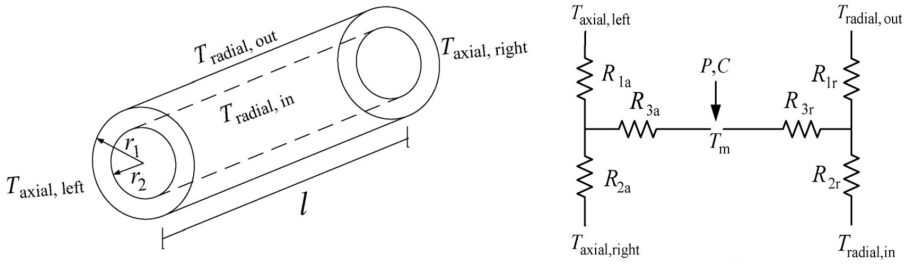

Figure 3.6
Schematic of the electrical analogy for the conduction block with internal heat generation [32].

the value of the two additional resistances can be obtained as:

$$R_{3r} = \frac{-1}{8\pi(r_i^2 - r_o^2)k_r L}\left[r_i^2 + r_o^2 - \frac{4r_i^2 r_o^2 \ln\frac{r_o}{r_i}}{(r_o^2 - r_i^2)}\right] \quad (3.21)$$

$$R_{3a} = \frac{-L}{6\pi k_a(r_o^2 - r_i^2)} \quad (3.22)$$

3.3.2 Conduction, convection, and radiation block

It can be useful to integrate into a single block the three heat transfer mechanisms. In particular, this can be helpful to increase the compactness of the 1D model. This block can be applied to simulate the housing of a turbo machine in contact with the external environment.

This block is supposed to transfer heat via conduction with the same approach of the conduction block described in subsection 3.3.1. In addition, at one port are connected the convection and radiation sub-blocks in parallel, meaning that the temperature drops across those components are the same as

$$\Delta T = T_s - T_\infty \tag{3.23}$$

Figure 3.7 shows the idea of the physical modeling of the block through the electrical analogy.

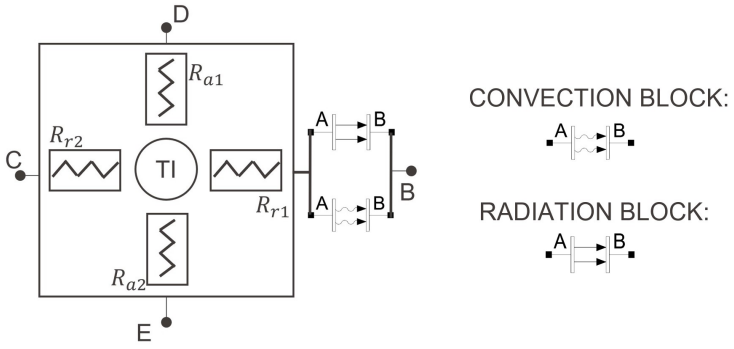

Figure 3.7
Schematic of the electrical analogy for the conduction, convection, and radiation block.

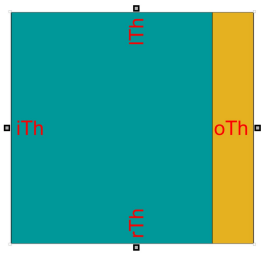

Figure 3.8
Simscape's graphical representation of the conduction, convection, and radiation block.

3.3.3 Convection block

The convection block allows the selection of different ways to compute the heat transfer coefficients by using correlations (section 2.3) and including in the thermal model the windage losses, according to section 2.4. The radial convection block may receive as an input signal the mass flow rates and it would be used in case the 'volute heat transfer' correlation is selected. Figure 3.9 shows the graphical interface of the convection block in Simscape.

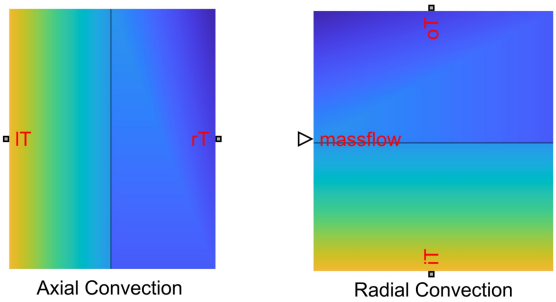

Figure 3.9
Simscape's graphical representation of the convection blocks.

3.3.4 Thermo-mechanical block

Once the temperature distribution is known in the whole domain, the analysis may further dig into critical aspects, such as thermal and centrifugal expansion, for static and rotating components.

According to Olmedo and Schiffmann [33], the relationship for strain ϵ and displacement u in case of small deformations is

$$\epsilon_{ij} = \frac{1}{2}\left(\frac{\partial u_i}{\partial x_j} + \frac{\partial u_j}{\partial x_i}\right) \tag{3.24}$$

The stress σ and the strain ϵ are related through the Hooke's law as

$$\sigma_{ij} = \frac{E}{1+v}\left(\epsilon_{ij} + \frac{v}{1-2v}\epsilon_{kk}\delta_{ij}\right) - \frac{E\alpha\Delta T}{1-2v}\delta_{ij} \tag{3.25}$$

where the last term of the second member takes into account the thermal effect, based on the temperature difference ΔT and the thermal expansion coefficient α, measured in K^{-1}.

By applying the 2D radial axisymmetric equilibrium condition, the centrifugal deformation of rotating elements is accounted for. In cylindrical coordinates yields:

$$\epsilon_{rr} = \frac{du}{dr} \quad \epsilon_{\theta\theta} = \frac{u}{r} \quad \epsilon_{zz} = C \tag{3.26}$$

The radial equilibrium including the rotational speed ω is

$$\frac{\sigma_{rr}}{dr} + \frac{1}{r}\left(\sigma_{rr} - \sigma_{\theta\theta}\right) + \rho\omega^2 r = 0 \tag{3.27}$$

The displacement u_{rr} at the radius r is found by combining the radial equilibrium 3.27 with the stress-strain 3.25 equations:

$$u_{rr}(r) = -\rho r^3 \omega^2 8 \frac{(1+v)(1-2v)}{E(1-v)} + c_1 r + \frac{c_2}{r} \tag{3.28}$$

where c_1 and c_2 are integration constants dependent on the boundary conditions.

According to Olmedo et al. [3], the analytical solution to the centrifugal radial deformation $u(r)$ of a hollow 2D cylinder yields:

$$u(r) = \frac{\rho\omega^2}{8E(1-\eta^2)} \left[-r^3 + (3+\eta) \left(\frac{(D_o^2 + D_i^2)r}{4(1+\eta)} + \frac{D_o^2 D_i^2}{16(1-\eta)r} \right) \right] \tag{3.29}$$

where D_o and D_i are the outer and inner diameter respectively of the hollow cylinder depicted in Figure 3.10, while E is the Young's modulus of the material, ρ is the density and η is the Poisson coefficient of the rotor material.

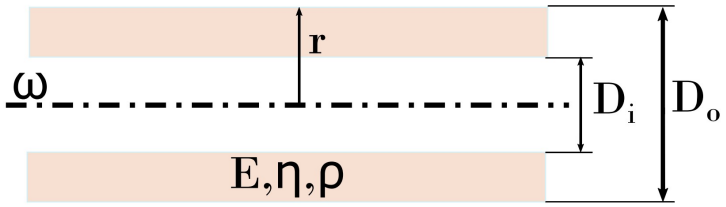

Figure 3.10
Geometric parameters involved in the calculation of the thermal expansions [33].

3.3.5 Varying thermal properties

Materials properties may vary to a major extent as a function of temperature. Therefore, in applications with grave thermal gradients and temperature ranges involved, the properties can no longer be assumed as constant, to improve the reliability of the model.

Considering the material properties invariant with temperature is a good approximation for ambient working conditions, hence it is not a reasonable hypothesis for the aim of this research. Accordingly, the materials' heat capacity and thermal conductivity are modeled with polynomial functions for temperature, for both 1D and 3D models.

Chapter 4

3D Modelling

4.1 Geometric modelling

This section attempts to present the process of geometry modeling as well as motivate the decisions taken throughout.

The CTU is made of 38 components with several contact faces, different size scales, and critical geometric features, such as sharp edges, small faces, and intersecting bodies. Dealing with complex geometry, if not carefully handled and sub-divided, could lead to failures at any level of the simulation's steps - from mesh generation to convergence issues.

Hence, for the first simulations, it has been decided to split the entire CTU into three sub-domains: the turbine side, the steam injection side, and the compressor side (see Figure 4.1).

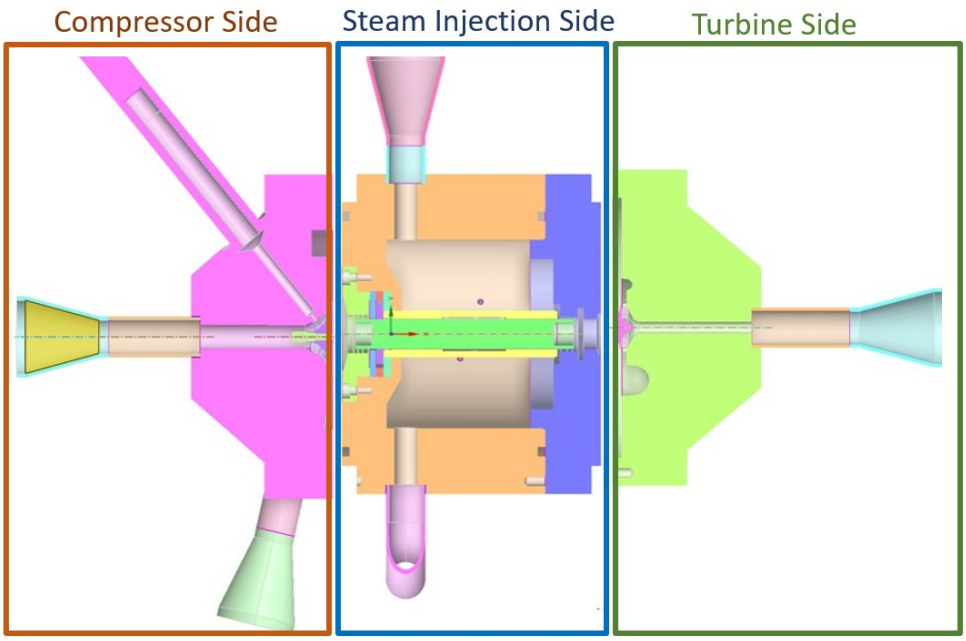

Figure 4.1
Partition of the CTU in three sub-domains: the compressor side, the steam injection side, and the turbine side.

To avoid problems at different levels of the simulation, other precautions are taken

into account:

- closure of all the domain openings except for the inlet, outlet, and labyrinth seal ports, to make it easier the definition of the flow domains and the boundary conditions.
- All the contact surfaces are recognized as single surfaces through the *Share topology* command in Space Claim, to speed up the mesh generation phase.
- The number of edges, small faces, and the complexity of the components is reduced, to decrease the number of cells that will be generated for the volume discretization.
- Specific surfaces of interest, such as the ones for thermal boundary conditions, inlet/outlet capping, and rotational speed, are named.

The fluid domain is not extracted at this level but it will be done during the mesh generation, to avoid possible problems due to interfering bodies [34].

To summarize, the geometries created are four. An extremely simplified one of the steam injection domain for the first part of the validation process (the validation of the 1D solid blocks). A simplified but representative one of the steam injection domain, for the validation of the fluid networks that model the central part of the CTU. An additional one for the computation of the heat transfer coefficients with CFD to be tuned in the 1D model. And a last one made of all three subdomains: the turbine side, the compressor side, and the steam injection side.

4.2 Physical modeling

Differently, from the 1D lumped parameter approach, CFD and FEA analysis solves partial differential equations ruling the physical laws by exploiting different schemes. This process may result in computational expenses, especially for transient problems. This section aims to provide useful insights about the equation solved by Ansys software.

4.2.1 Thermal problem

The governing PDE which rules thermal behavior occurring in solid bodies is

$$\frac{\partial}{\partial t}(\rho h) + \nabla \cdot (\vec{v}\rho h) = \nabla \cdot (k\nabla T) + S_h \tag{4.1}$$

where k is the thermal conductivity in [$\mathrm{W\,K^{-1}\,m^{-1}}$], t is the time in [s], T is the temperature in [K], S_h is the volumetric heat source in [$\mathrm{W/m^3}$] and h is the sensible enthalpy evaluated as

$$h = \int_{T_{ref}}^{T} c dT \tag{4.2}$$

where c is the specific heat capacity of the material in $[\mathrm{J\,kg^{-1}\,K^{-1}}]$.

The first term of equation (4.1) is the rate of energy storage in the body responsible for the dynamic behavior of the analysis - namely the transient term. Once this term becomes negligible, the steady state condition has been achieved. The second term on the left-hand side represents convective energy transfer due to the rotational or translational motion of the solids. The velocity field $\vec{v}$ is computed from the motion specified for the solid component as a boundary condition. The terms on the right-hand side are the heat flux due to conduction and volumetric heat sources within the solid, respectively.

In the case of materials that behave anisotropically, the only term of (4.1) that has to be modified is the conduction one, becoming

$$\nabla \cdot (k_{ij} \nabla T) \tag{4.3}$$

where k_{ij} represents the thermal conductivity matrix since the thermal properties are in this case directional dependent.

Regarding fluids, the general energy equation becomes more complex, and with additional terms, as follows

$$\frac{\partial}{\partial t}\left(\rho(e + \frac{v^2}{2})\right) + \nabla \cdot \left(\rho v(h + \frac{v^2}{2})\right) = \nabla \cdot (k_{eff} \nabla T - \sum_j h_j \vec{J}_j + \overline{\overline{\tau}}_{eff} \cdot \vec{v}) + S_h \tag{4.4}$$

where e is the internal energy, v is the velocity field, k_{eff} is the effective conductivity which is the sum of the thermal conductivity k, and turbulent thermal conductivity k_t - defined according to the turbulence model being used. $\vec{J}_j$ is the diffusion flux of species j. The first three terms on the right-hand side of equation (4.4) represent energy transfer due to conduction, species diffusion, and viscous dissipation, respectively.

For more details regarding the equation's terms and how they are modeled in different cases refer to [35].

4.2.2 Fluid flow

In this section, the conservation equations for fluid flow in an inertial reference frame are presented.

The mass conservation equation, named continuity equation, in the most general and local form, can be written as

$$\frac{\partial \rho}{\partial t} + \nabla \cdot (\rho \vec{v}) = S_m \tag{4.5}$$

where S_m is the mass source term and represents the mass added to the continuous phase, for instance when phase change problems are involved.

The second ODE involved in the problem regarding fluid flows is the conservation of momentum. In an inertial reference frame can be written as

$$\frac{\partial}{\partial t}(\rho\vec{v}) + \nabla \cdot (\rho\vec{v}\vec{v}) = -\nabla p + \nabla \cdot (\overline{\overline{\tau}}) + \rho\vec{g} + \vec{F} \tag{4.6}$$

where p is the static pressure, $\rho\vec{g}$ is the the gravitational body force and $\vec{F}$ is the external body force. $\overline{\overline{\tau}}$ is the viscous part of the stress tensor given by

$$\overline{\overline{\tau}} = \mu\left[(\nabla\vec{v} + \nabla\vec{v}^T) - \frac{2}{3}\nabla \cdot \vec{v}I\right] \tag{4.7}$$

where μ is the molecular viscosity, I is the unit tensor and the second term on the right-hand side is the effect of volume change.

The fluid used for all the cases of study is either water vapor or air, which belongs to the category of Newtonian fluids. The physics behind a Newtonian fluid is that the shear stress arising from the motion of the fluid is proportional to the rate of change of the fluid's velocity; the constant of proportionality is the dynamic viscosity of the fluid.

For a 2D general case with a cartesian frame of reference, the Newtonian fluid inner shear stress is analytically described by the equation 4.8, in which τ_{ij} [Pa] is the j^{th} component of the stress acting on the faces of the fluid element perpendicular to i axis, μ [kg/(m·s)] is the fluid dynamic viscosity, x_i and x_j are the i^{th} end j^{th} spatial coordinates measured in [m], v_i and v_j are the fluid's velocity components in the two directions and measured in [m/s].

$$\tau_{ij} = \mu(\frac{\partial v_i}{\partial x_j} + \frac{\partial u_j}{\partial x_i}) \tag{4.8}$$

The dynamic viscosity of a Newtonian fluid is only dependent upon temperature and pressure. However, in this research, the dynamic viscosity is kept constant with respect to pressure and temperature.

The fluid is modeled as compressible, meaning that the density depends locally on the fluid's thermodynamic state. The density value is modeled according to the ideal gas law, equation 4.9.

$$pV = nRT \tag{4.9}$$

4.2.3 Turbulence modeling

In Reynolds averaging, the solution variables in the instantaneous Navier-Stokes equations are decomposed into the mean (ensemble-averaged or time-averaged) and

fluctuating components. For the velocity components yields

$$u_i = \overline{u}_i + u_i' \tag{4.10}$$

where $\overline{u}_i$ and u_i' are the mean and fluctuating velocity components in the direction $i = 1, 2, 3$.

Likewise, for pressure and other scalar quantities holds

$$\phi = \overline{\phi} + \phi' \tag{4.11}$$

where ϕ denotes a scalar such as pressure, energy, or species concentration. Substituting expressions of this form for the flow variables into the instantaneous continuity and momentum equations and taking a time (or ensemble) average (and dropping the overbar on the mean velocity, $\overline{u}$) yields the ensemble-averaged momentum equations. They can be written in a cartesian tensor form as

$$\begin{cases} \frac{\partial \rho}{\partial t} + \frac{\partial}{\partial x_i}(\rho u_i) = 0 \\ \\ \frac{\partial}{\partial t}(\rho u_i) + \frac{\partial}{\partial x_i}(\rho u_i u_j) = -\frac{\partial p}{\partial x_i} + \frac{\partial}{\partial x_j}\left[\mu\left(\frac{\partial u_i}{\partial x_j} + \frac{\partial u_j}{\partial x_i} - \frac{2}{3}\delta_{ij}\frac{\partial u_i}{\partial x_i}\right)\right] + \frac{\partial}{\partial x_j}(-\rho\overline{u_i' u_j'}) \end{cases} \tag{4.12}$$

Equation 4.12 are called Reynolds-averaged Navier-Stokes (RANS) equations. They have the same general form as the instantaneous Navier-Stokes equations, with the velocities and other solution variables now representing ensemble-averaged (or time-averaged) values. Additional terms now appear and represent the effects of turbulence. The Reynolds stresses $-\rho\overline{u_i' u_j'}$ must be modeled to close Equation 4.12 and the fluid dynamics problem.

4.2.4 Standard k-ω Model

This section aims to introduce a model for the Reynolds shear stresses computation. The standard $k - \omega$ model is an empirical model based on modeling transport equations for the turbulence kinetic energy k and the specific dissipation rate ω.

The turbulence kinetic energy k and the specific dissipation rate ω are obtained from the following transport equations

$$\frac{\partial}{\partial t}(\rho k) + \frac{\partial}{\partial x_i}(\rho k u_i) = \frac{\partial}{\partial x_j}\left(\Gamma_k \frac{\partial k}{\partial x_j}\right) + G_k - Y_k + S_k + G_b \tag{4.13}$$

$$\frac{\partial}{\partial t}(\rho \omega) + \frac{\partial}{\partial x_i}(\rho \omega u_i) = \frac{\partial}{\partial x_j}\left(\Gamma_\omega \frac{\partial \omega}{\partial x_j}\right) + G_\omega - Y_\omega + S_\omega + G_{\omega b} \tag{4.14}$$

G_k represents the generation of turbulence kinetic energy due to mean velocity gradients. G_ω represents the generation of ω. Γ_k and Γ_ω represent the effective diffusivity of k and ω, respectively. Y_k and Y_ω represent the dissipation of and due to turbulence. S_k and S_ω are source terms, G_b and $G_{\omega b}$ account for buoyancy terms. For further details about the calculation of the above terms, refer to [35].

In particular, for the CFD analysis of the current study, the Shear Stress Transport (SST) $k-\omega$ is chosen for its advantages compared to other models available [35]:

- good performance for wall-bounded, complex boundary layers and adverse pressure gradient conditions. Useful aspects when conjugated heat transfer problems are involved since the heat transfer is highly dependent on the boundary layer developed.
- combines the original Wilcox $k-\omega$ model near walls and the standard $k-\epsilon$ model away from walls.
- better numerical stability than the $k-\epsilon$ due to the functions implemented.

Additionally, Enhanced Wall Treatment (EWT) was used for all the CFD simulations. EWT is a technique used in computational fluid dynamics to improve the accuracy of predictions near solid surfaces [35]. The goal of EWT is to enable more accurate predictions of near-wall turbulence without resorting to extremely fine meshes, allowing for better resolution of boundary layer flows and improved heat transfer predictions in CFD simulations.

Standard turbulence models might struggle to capture the near-wall behavior accurately due to their reliance on turbulence parameters that tend to become singular or approach unrealistic values near solid boundaries [35]. Enhanced Wall Treatment methods aim to address these issues by providing a more accurate representation of the flow near walls without the need for excessive grid refinement, which can be computationally expensive.

EWT involves modifications to the turbulence model equations near-walls to improve predictions in these regions. For the $k-\omega$ turbulence model, Enhanced Wall Treatment methods involve adjustments to the near-wall damping functions, and modifications to the k and ω equations in the near-wall region.

4.3 Computational mesh

At the base of the finite element analysis, it is necessary to discretize the 3D volume in a finite number of elements. This allows us to solve the partial differential equations concerning the problem of interest.

4.3.1 Boundary layers

It is recommended, for conjugated heat transfer problems, the use of boundary layer cells for both solid and fluid regions [35]. For the fluid region, this mesh feature allows us to better solve the fluid behavior near walls, where high shear stress and

velocity gradient are expected. A number of 5 inflation layers is generated for the fluid region, while the number is set to 3 for the solid parts. The offset method type used is the smooth transition option. It does not allow to define explicitly the layer thickness, but it is computed from the size of local quadrilateral elements to ensure a smooth change in the area ratio of adjacent elements [36]. The growth rate of inflation layers, defined as the ratio of thickness between adjacent layers starting from the wall, is specified as 1.1, to ensure a good cell size transition in small gaps.

Figure 4.2 shows the boundary layer refinements. Figure (a) is an enlargement of the 0.25 mm gap of the radial bearings; the component in violet is the rotor and the one in blue is the journal bearing. Figure (b) shows the detail of the axial bearings gap of 0.25 mm; in brown and violet is the rotor while in blue are the axial bearings. For both images, the golden area represents the fluid region.

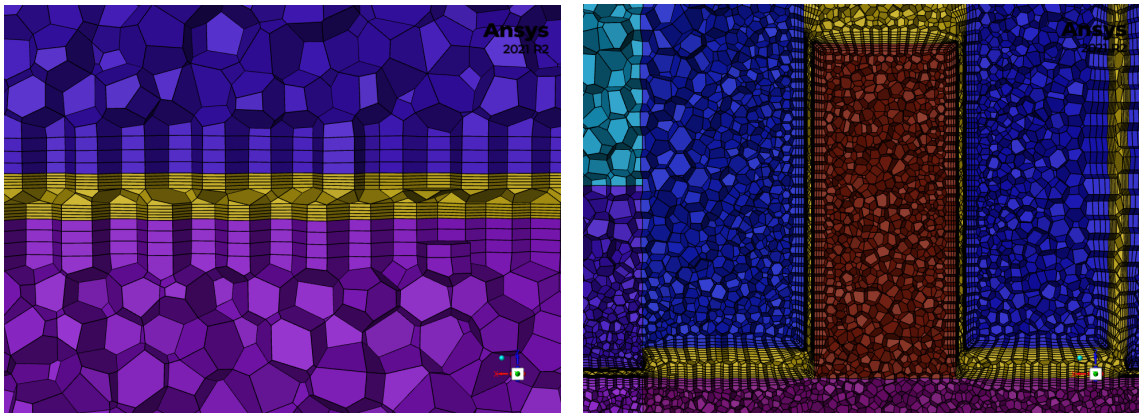

(a) **(b)**

Figure 4.2
Boundary layer refinements for radial bearing (A) and axial bearing (B)

The boundary layer feature is also an optimizing method in terms of computational cost. Indeed, the elements generated have a small dimension along the direction of big gradients, hence along the wall's normal vector, whereas they are characterized by a higher thickness in the direction of small gradients, thus the direction tangent to the walls. For this reason, the boundary layer elements have a high aspect ratio, which is defined as the ratio of the longest to shortest side - a way to measure the element stretching.

Figure 4.3 shows the computational mesh for the geometry with all the subdomains: boundary layers and near-wall refinements can be appreciated.

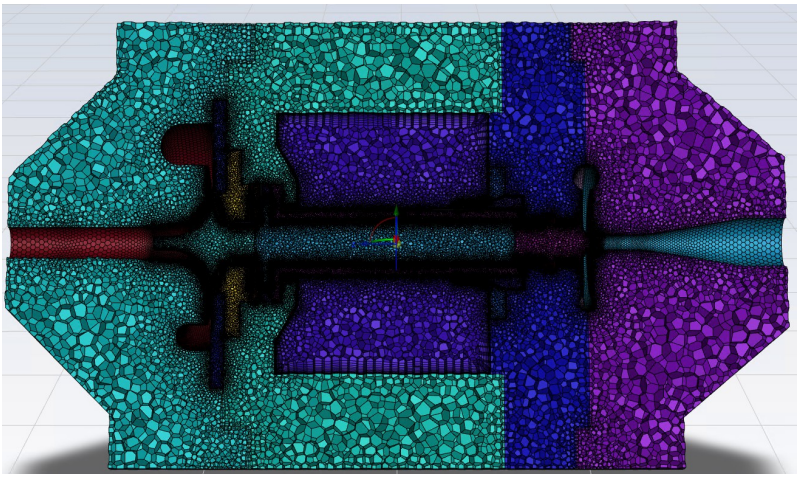

Figure 4.3
Computational mesh for the geometry with all the three subdomains.

4.3.2 Mesh quality

Different parameters for describing the mesh quality exist. However, the more important ones are [34]:

1. the skewness, which indicates how a triangle is far from being equilateral, which would be perfect for the computation. It ranges from 0 - equilateral triangle - to 1 - degenerate triangle. Good values of skewness are below 0.7.
2. the orthogonality, which measures the alignment between two elements' faces. Orthogonality is 1 for perfectly aligned faces and a good value can be considered when above 0.3.

After the generation of the mesh, *Fluent* gives as default the maximum skewness and minimum orthogonality values. However, for mesh with a large number of cells, it is important to check the overall trend of the elements' quality, as shown in the graphs in Figure 4.4.

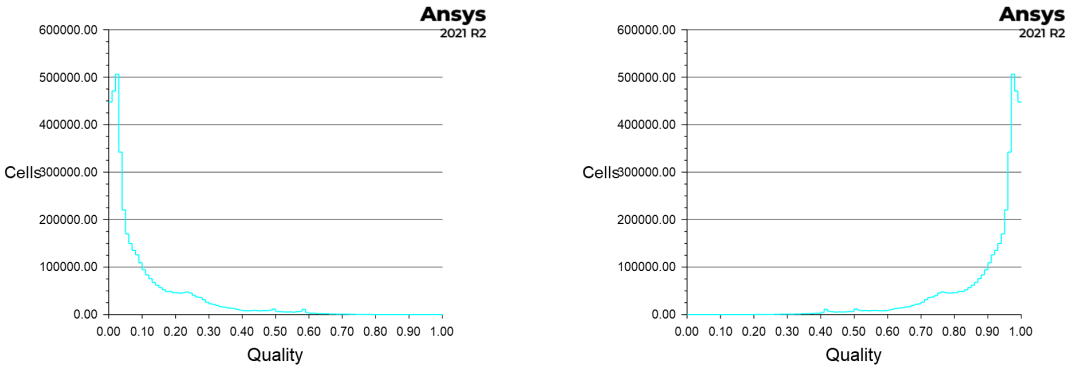

(a) **(b)**

Figure 4.4
Skewness (A) and orthogonality (B) for the steam injection's mesh

4.3.3 Grid dependency test

The mesh generation phase is characterized by several parameters and settings that can be changed. Therefore, it is important to ensure that the results do not depend upon those variables to reach a good reliability of the model.

The mesh type has been changed between the structured and unstructured mesh. For the first method, the elements generated are hexahedra for the domain's core and polyhedra near the wall boundaries. For the unstructured mesh, the polyhedra elements type is chosen.

Figure 4.5 shows the differences between structured and unstructured mesh for the steam injection side.

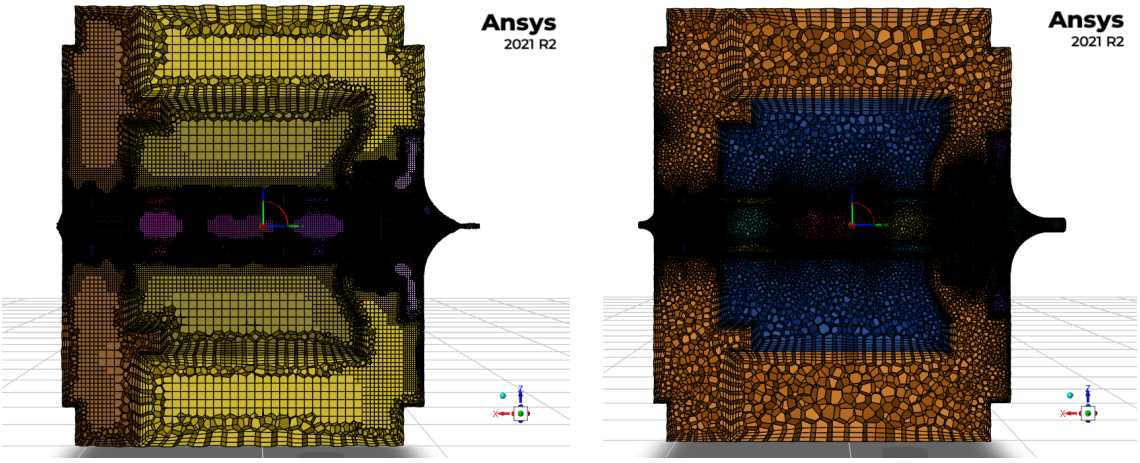

(a) **(b)**

Figure 4.5
Structured mesh constituted of poly-hexahedra elements (A) and unstructured mesh made of polyhedra elements (B) - steam injection side

The change in the mesh type highly affects the number of cells in the discretized volume. To give some numbers, for the steam injection domain the structured mesh is composed of 7.070.043 while the unstructured one is made of 4.044.232 cells, considering the same geometry and other mesh parameters.

Different simulations were run with the two mesh described. No changes in the results of interest are spotted. Hence, the unstructured mesh grid is selected for all future calculations due to the smaller number of cells.

4.4 Numerical methods

This section illustrates the numerical approach used for simulating the fluid flow pattern and computing the primary quantities of interest.

4.4.1 Solver type

The fluid flow through the compressor-turbine unit is studied with steady-state and transient simulations and a turbulent model is chosen for modeling the viscous effects. In the case of the steady-state condition, *Ansys Fluent* solves the Navier-Stokes equation, with the assumptions that the flow is steady, compressible, and independent of external forces, as shown in equation 4.15:

$$\nabla \cdot \mathbf{u} = 0 \tag{4.15}$$

$$(\mathbf{u} \cdot \nabla)\mathbf{u} = -\nabla p - \frac{1}{Re}\nabla^2 \mathbf{u} \tag{4.16}$$

where $\mathbf{u}$ is the flow velocity, p is the pressure, and Re is the Reynolds number. Since the working fluid is assumed compressible, a density-based solver with a coupled pressure-velocity scheme is employed to solve the velocity and pressure.

4.4.2 Spacial discretization method

To convert the partial differential control equations into the form of algebraic equations, the finite volume method is implemented in *Ansys Fluent*. The spatial domain is discretized with the QUICK scheme which is a higher-order numerical scheme. It achieves third-order accuracy by using a higher-degree polynomial to approximate the solution within the control volume. It attempts to reduce numerical diffusion and better capture flow features, especially in regions with steep gradients.

Moreover, for the CFD simulations in *Ansys Fluent*, the option *"keep high order accuracy"* was selected, to maintain a higher level of accuracy and convergence throughout the solution process. This involves strategies to refine the solution, reduce numerical errors, and adjust convergence criteria to ensure the simulation achieves higher accuracy levels during iterations.

4.4.3 Solution monitoring

During the iterations, it is important to keep track of some crucial parameters. The default values plotted by *Ansys Fluent* during the numerical computation are the residuals, which measure the error of the solution at each iteration.

The residuals check is a good starting point to understand if the physical problem is well posed, feasible boundary conditions are set, good mesh quality is used, and numerical stability during the computation is respected. However, quantities of interest such as the mass flow rates, the pressures or the temperatures have to be monitored as well, to ensure the validity of the results. In general, the physical parameters kept under attention should achieve stability before the residuals do. If the physical quantities continue to vary while the residuals are already steady, something wrong in the simulation has been set.

A good solution convergence, obtained for the steam injection domain simulation, is

described by Figure 4.6 where the residuals (a) and outlet mass flow rate (b) are monitored along iterations.

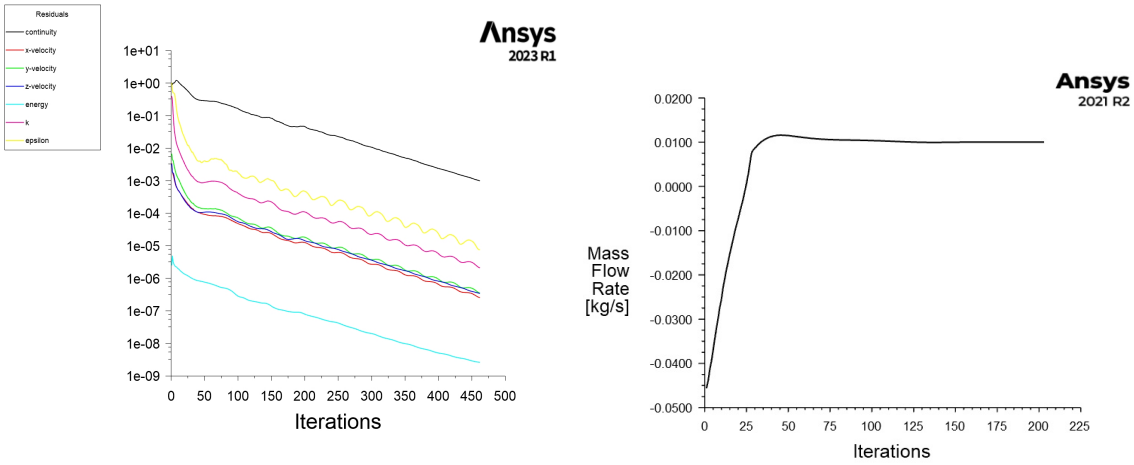

(a) **(b)**

Figure 4.6
Residuals (A) and outlet mass flow rate (B) monitoring for a steam injection side simulation.

For most of the simulations run, it was necessary to decrease the default threshold for the residuals since the results still changed while the residuals had already reached the default lower limit of *Fluent*.

Chapter 5

Results

5.1 FEA validation

5.1.1 Steady-state

The aim of simulating only the solid components is to validate the conduction-convection-radiation blocks of the 1D model and to help in the code debugging process.

To lower the degree of freedom between the 1D and 3D analysis and to make the results depend just on the applied fundamentals thermal laws (subsection 3.3.1), a material with constant properties as a function of temperature is considered. Hence, it has been applied temperature-independent material properties of Stainless Steel 404 (SS 404) available in *Ansys Mechanical*, and the same values were tuned in the solid blocks of the 1D model. In particular, the properties of interest were the density ρ, the specific heat capacity c_p, and the thermal conductivity λ.

For the current validation, a simplified 3D geometry of the CTU has been generated using *SpaceClaim*, as shown in Figure 5.1a. The geometry includes the steam injection domain of the CTU, along with the steam injection chamber and the bushing; the dimensions are the same as the actual geometry. These simplifications are just meant to reduce the mesh elements, thus increasing the computation speed and the validation process. Figure 5.1b shows the discretization of the geometry and the solid thermal blocks connection in *Simscape* for the 1D approach. Although graphically the dimensions between the two models do not seem the same, the geometry parameters in the solid blocks were tuned correctly.

Two source terms of 100 W each are set as boundary conditions of the thermal problem, mimicking the heat generated from windage losses. The source terms are the components highlighted in red in Figure 5.1a. Convective heat transfer on the outer surface of the housing is imposed, with a heat transfer coefficient of 9.2 $W/K/m^2$ (value found using the correlation for natural convection on horizontal cylinder described in subsection 2.3.1) and an ambient temperature of 50 °C.

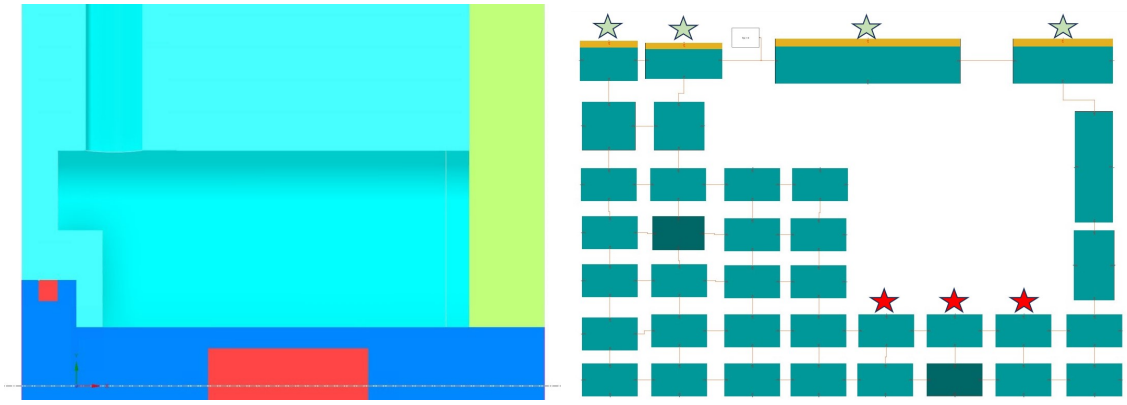

(a) (b)

Figure 5.1
Mid plane cross-section of the CTU's simplified geometry and the source term highlighted in red (a). Geometry discretization of the 1D model, the stars indicate the location of the temperature probe used for the validation (b).

In Figure 5.2, the temperature distribution on the cross-section - obtained by the FEA analysis in *Ansys Mechanical* - is shown.

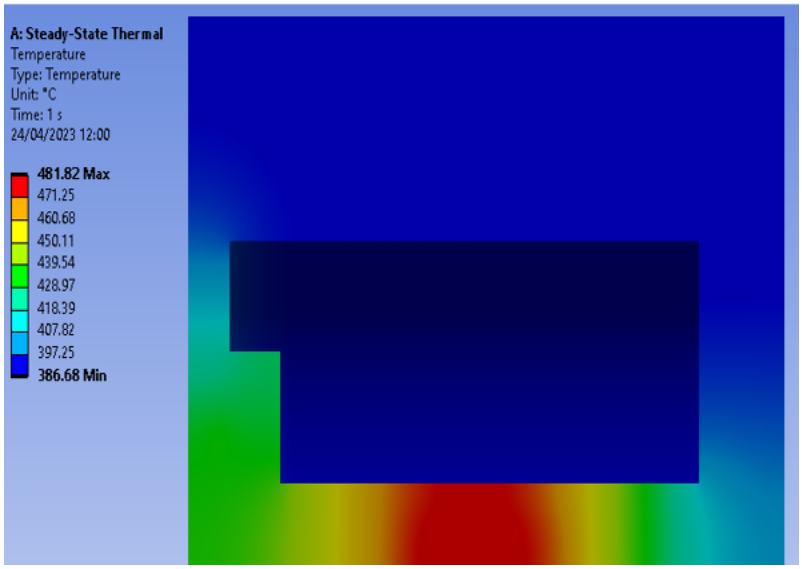

Figure 5.2
Temperature distribution obtained from FEA analysis in *Ansys Mechanical*.

Figure 5.3 shows the difference in the temperature gradients across the bushing and the rotor for the two models. For the 1D analysis, the temperature gradient across the housing and the bushing were measured at the nodes labeled with the colored stars in Figure 5.1b. For the FEA results assessment, the surfaces of the 3D model were properly split, and the *area weighted average* of the temperature at any surface of interest was caught. The results between the 1D and 3D models match well, with a maximum relative error of less than 5 %, where the temperature peak is located,

thus at the level of one of the source terms. The temperature gradients across the housing have a maximum difference of less than 1 K between the two models.

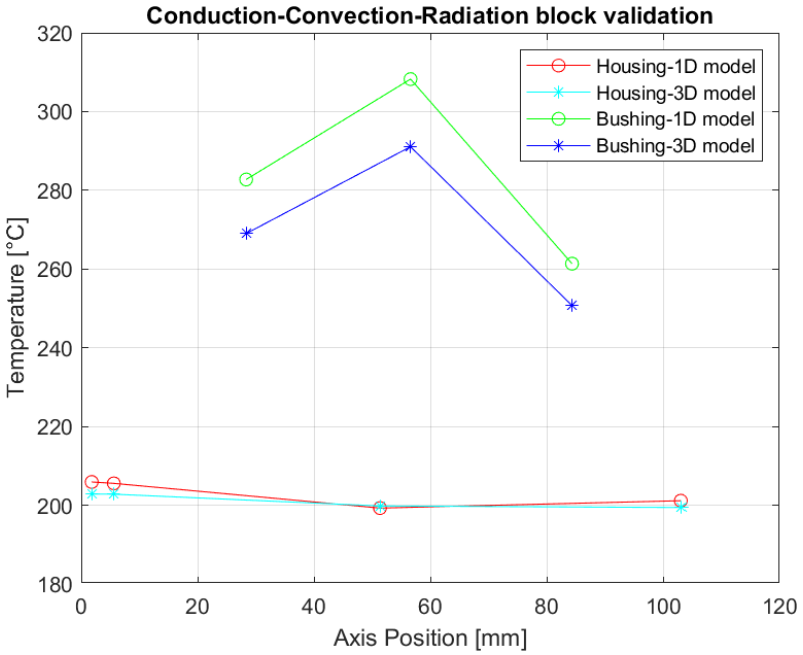

Figure 5.3

Bushing and housing temperature gradients obtained with the 1D and 3D simulations, for the first thermal analysis.

To assess the robustness of the model, an additional thermal condition is considered, imposing a fixed temperature of 800 °C (Dirichlet boundary condition) on the surface highlighted in red in Figure 5.4a. The solution of the FEA analysis can be seen in Figure 5.4b.

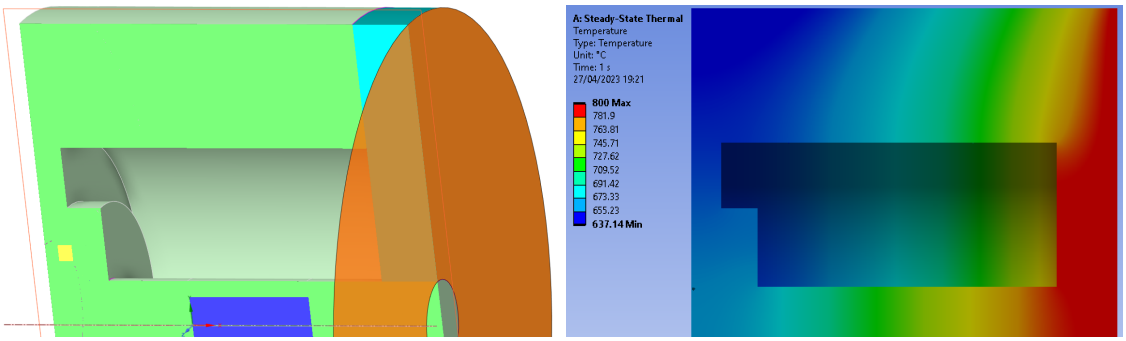

(a) **(b)**

Figure 5.4

Mid plane cross-section of the CTU with the Dirichlet BC highlighted in orange (a), and the temperature distribution from the FEA simulation for the second thermal analysis (b).

In Figure 5.5 is depicted the discretization of the solid domain in the 1D model and four temperatures in different positions are probed for results validation, labeled in the figure with numbers from 1 to 5.

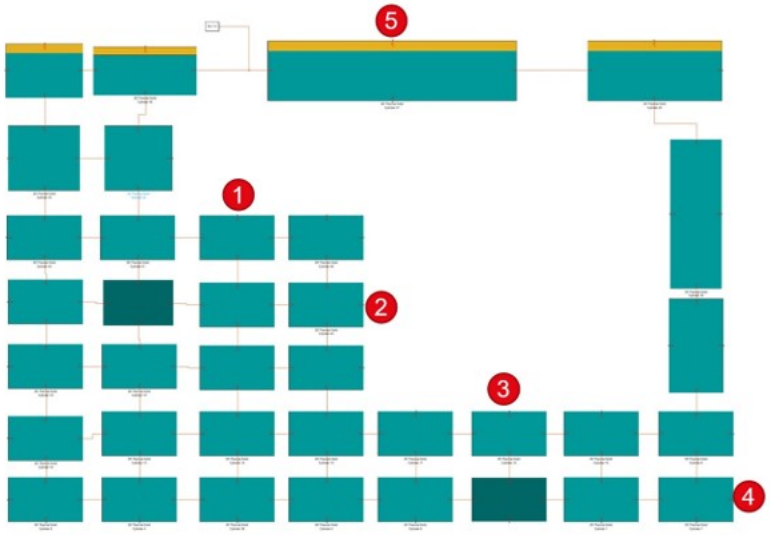

Figure 5.5
1D model for the validation of the conduction-convection-radiation blocks, for the second thermal condition. The T probes are labelled with numbers up to 5.

The results comparison is reported in Table 5.1 along with the relative error for each point, which is acceptable and always below 6 %.

Table 5.1
Temperature comparison between the 1D and 3D model in 5 different points, for the second thermal condition.

	TEMPERATURE [°C]				
Point	1	2	3	4	5
1D MODEL	670.33	672.51	732.83	790.73	651.17
3D MODEL	660.55	663.83	730.08	795.56	669.94
Relative Error [%]	1.48	1.31	0.38	0.61	2.80

5.1.2 Transient-state

The validation of the 1D transient solution has to be validated with a 3D FEA model following a similar procedure to the previous section. The initial temperatures of the solids are set at 22 °C and the simulations have been stopped after 100 s due to the high demanding computational cost of the 3D model. The material, as before, is set with constant thermal properties, in this way the results depend just upon the transient numerical solution and not on other approximations.

The exact boundary conditions described in the first thermal condition of subsection 5.1.1 have been applied: two source terms (Figure 5.1a) of 100 W each and natural convection on the outer surfaces of the housing, with a heat transfer coefficient of 9.2 W/K/m^2 and an ambient temperature of 50 °C. The time step for the 3D simulation has been computed with the option *ProgramControlled*, thus based on an algorithm the time step is defined at any integration step by the software and it stands within the range $0.001 - 0.1$s.

In Figure 5.7 and Figure 5.6 can be seen the evolution for the 1st, 2nd, 3rd, and 4th temperature probes, highlighted in Figure 5.5. For the 3D results, they were post-processed evaluating the temperature area-weighted average of the surfaces of interest. The temperatures in time are plotted for the first 100 s, a period in which the gradients have a very steep trend in time.

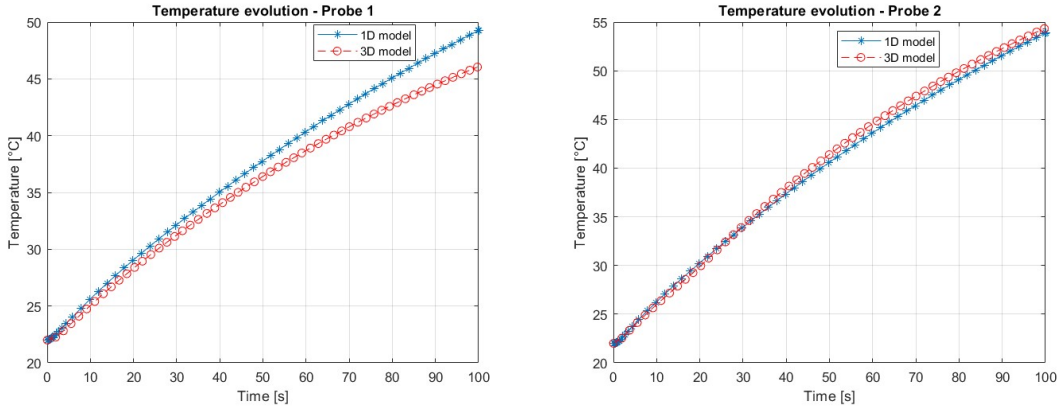

(a) **(b)**

Figure 5.6
Temperature time-evolution of probe 1 (a), and probe 2 (b). Comparison between 1D and 3D models.

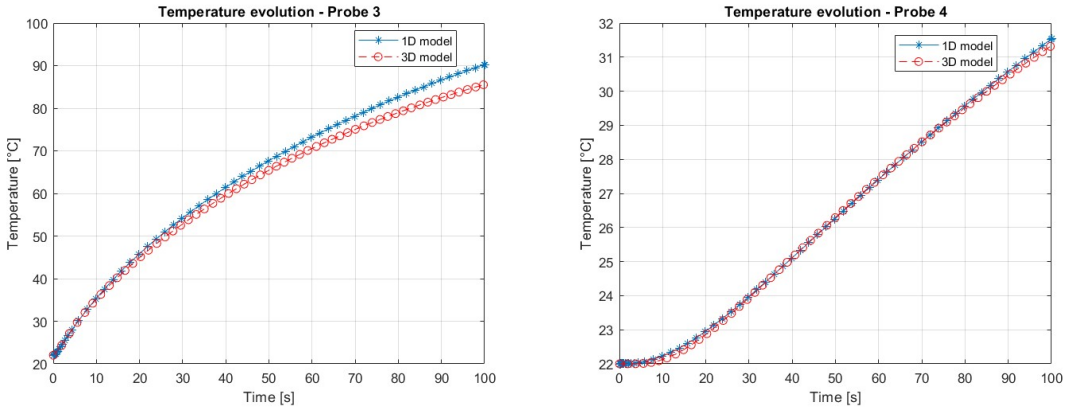

(a) **(b)**

Figure 5.7
Temperature time-evolution of probe 3 (a), and probe 4 (b). Comparison between 1D and 3D models.

The post-process shows good agreement with the two models. After 100 s, *probe 1* and *3* are affected by the maximum errors, however less than 4 %.

5.2 CFD validation - No fluid flow

5.2.1 Steady-state

During operating conditions, the steam injection chamber is filled in with water vapor with an inlet temperature of 420 °C and a nominal mass flow rate of 8 $\mathrm{kg\,s^{-1}}$. The main functions are to flatten the temperature gradients along the shaft, partially dissipate the windage losses, and feed the gas bearings.

The steam injection chamber has been discretized as shown in Figure 5.8, thus in 5 different volumes, represented in the 1D model as pipe blocks. The reason why multiple pipes have been used is that, since any pipe can exchange heat with only one thermal port at a fixed temperature, the use of several pipes allows for better capture of the thermal gradients. On the other side, if just one pipe block had been used, all the surfaces inside the steam injection chamber would have been at the same temperature, leading to an unrealistic approximation.

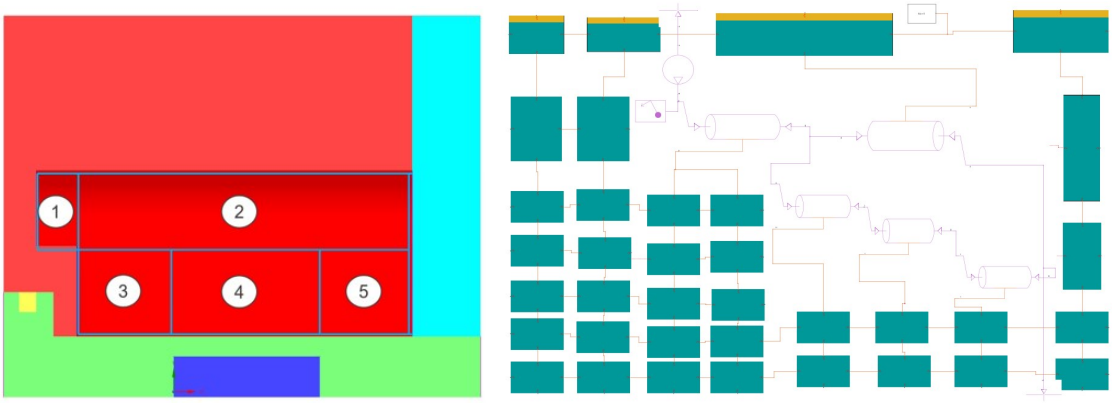

(a) (b)

Figure 5.8
Steam injection chamber discretization (a) and 1D modelling of the fluid network (b).

Firstly, for the validation of the models it has been decided to start with a condition without steam flow, hence the chamber has been filled with steam at a fixed temperature, but with no mass flow, thus the flow is buoyancy-driven. Two simulations have been performed, which can be seen as an extreme sensitivity analysis on the accuracy of the model: for the first case, the chamber has been filled with steam at 20 °C, while for the second one, the steam's temperature is set at 400 °C. Additionally, a heat source of 100 W is set inside the bushing, as for the solid block validations.

The temperature gradients across the bushing have been compared between the 1D and 3D models because it represents a critical region, i.e. the biggest temperature differences occur here, due to the imposed boundary conditions and source terms.

Figure 5.9 shows the results obtained for the case of the fluid inlet temperature of 20 °C: the temperatures contours on the bushing obtained from the 3D simulation (a), and the results comparison between the 1D and 3D model (b). In Figure 5.10 the same images are reported but in the case of fluid inlet temperature of 400 °C.

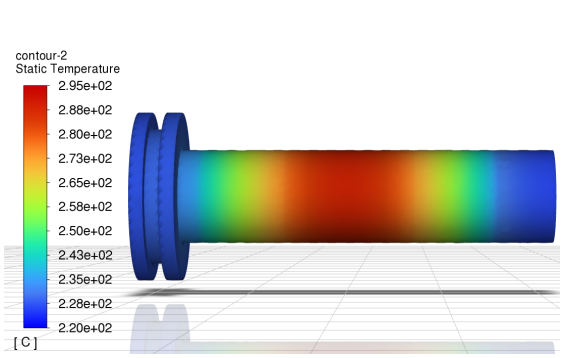

(a)

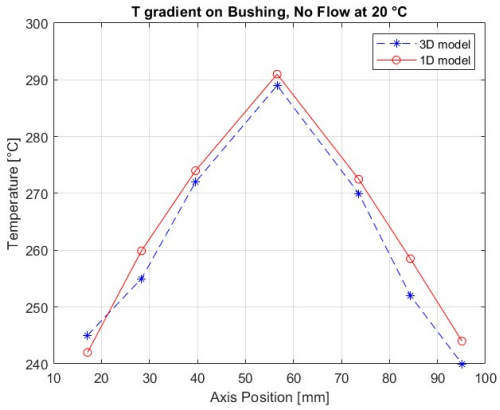

(b)

Figure 5.9

Steam chamber filled in with air at 20 °C. (a) shows the bushing's temperature contour obtained from the FEA analysis, and (b) compares the temperature gradient along the bushing axis caught by the 1D and 3D simulations.

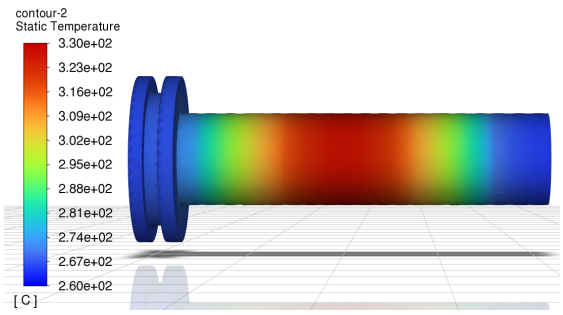

(a)

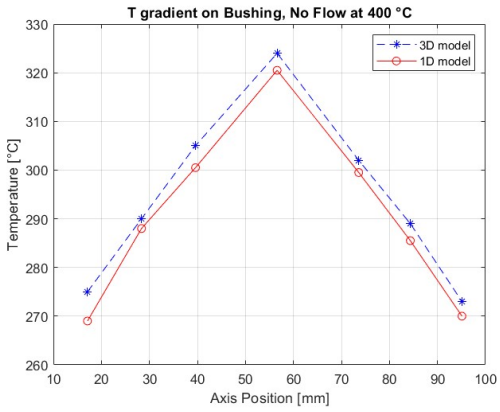

(b)

Figure 5.10

Steam chamber filled in with air at 400 °C. (a) shows the bushing's temperature contour obtained from the FEA analysis, and (b) compares the temperature gradient along the bushing axis caught by the 1D and 3D simulations.

For both cases, the agreement with the post-processed results is good, with maximum relative errors between the two models of less than 1 %. The 1D model can predict correctly the steep thermal gradient due to the source term applied. Additionally, the extreme sensitivity analysis applied through highly different fluid inlet temperatures confirms the robustness of the 1D approach.

5.2.2 Transient-state

The same workflow that has been performed for the conduction blocks is followed for the fluid network, the transient behavior is the focus of this section. The same boundary conditions of subsection 5.2.1 are imposed, comprising the change in the fluid inlet temperature (20 and 400 °C for the two cases).

For the post-processing of the results, several temperature probes are monitored. However, for the sake of report compactness, just the area-weighted averages of the temperature at the surfaces highlighted in Figure 5.11 are reported, and the 1D temperatures at the outer nodes of the respective discretized shells are considered. The period analyzed is the range 0-120 s.

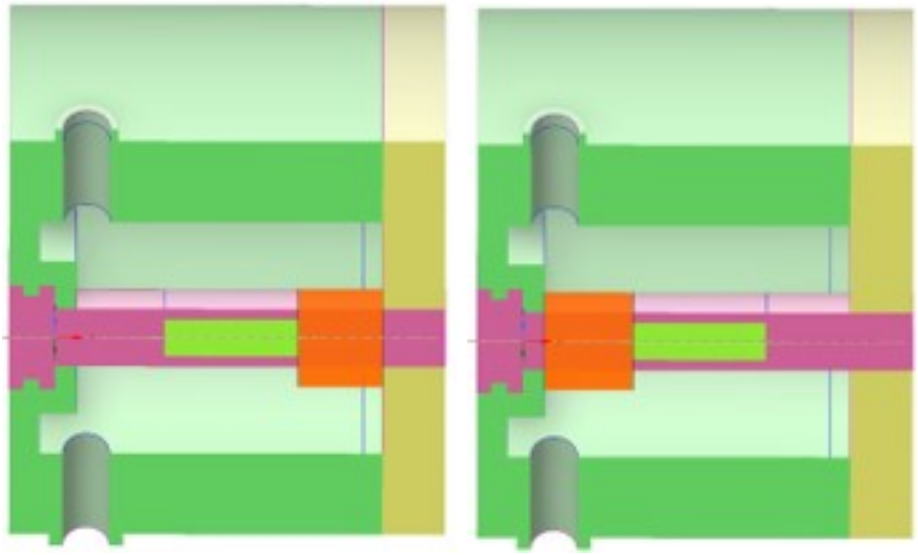

(a) **(b)**

Figure 5.11
Surfaces for which the temperature area-weighted averages are reported. For the comparison, the 1D temperatures at the outer nodes of the respective discretized shells are considered.

Figure 5.12 (b) shows the temperature area-weighted average of the right side of the bushing of the CFD analysis compared to the transient behavior captured by the 1D model, in the case of steam injection chamber filled with steam at 20 °C. The trends match very well, with a maximum error after 120 s of 0.7 % (T of the 3D result is 337 K while for the 1D is 339 K).

Figure 5.12 (a) compares the temperature area-weighted average of the right side of the bushing of the CFD analysis and the transient behavior captured by the 1D model, in the case of steam injection chamber filled with steam at 400 °C. After 120 s the temperature of the 3D result is 352K while for the 1D is 353 K (relative error of 0.85 %).

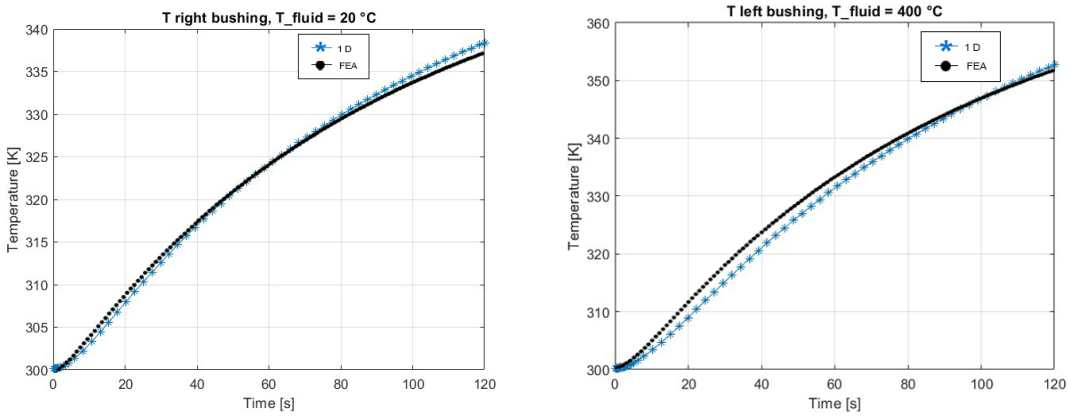

(a) **(b)**

Figure 5.12

Comparison of the transient behavior captured by the 3D and 1D simulations. Condition with no mass flow rate, hence the fluid motion is driven by buoyancy. A heat source of 100 W is applied in the middle part of the bushing, (a) compares the results with air's inlet T of 20 °C, while (b) with air's inlet T of 400 °C.

However, the fluid flow modeled as shown in Figure 5.8 seems to be not accurate when mass flow rates are imposed at the inlet of the steam injection.

The reason is that the complex 3D velocity field cannot be captured and described using pipes, since they force somehow the flow direction, neglecting the complex 3D flow pattern constituted by vortexes and eddies inside the chamber.

As proof of the high turbulent flow, the velocity field from the CFD results in the steam injection chamber is reported. Figure 5.14 shows the velocity contours with two different cut views, and Figure 5.14 shows the velocity vectors. The inlet mass flow rate imposed for this simulation is 0.5 $\mathrm{kg\,h^{-1}}$ of steam, which is far away from the nominal conditions of 8 $\mathrm{kg\,h^{-1}}$, meaning that the flow field might become even more complex.

In general, the 1D approach followed so far would be potentially good in the presence of an axis-symmetric problem, which is not the case in the current case of study, hence the difficulties to model it employing 1D tools increase.

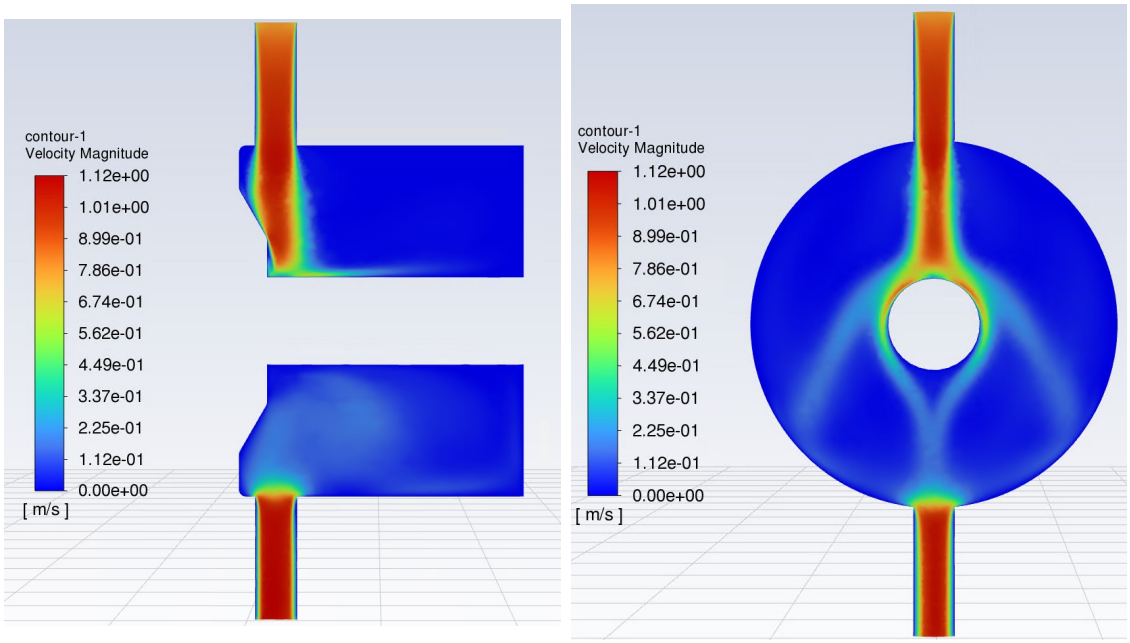

(a) (b)

Figure 5.13
Velocity field contour on a cross-section embedding the rotor axis (a). Velocity field contour on the section cutting the inlet and outlet of the steam injection domain (b).

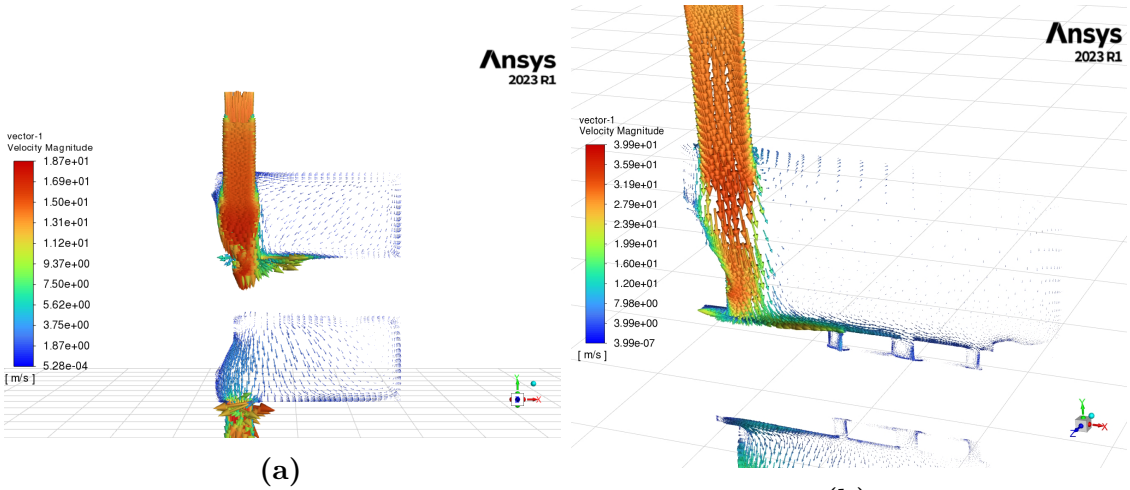

(a) (b)

Figure 5.14
Velocity field vectors on a cross-section embedding the rotor axis, with a frontal view (a), and an isometric view (b).

5.3 CFD validation - Fluid flow

To make the analysis more robust, it has been decided to model the 1D fluid network based on additional correlations that can be applied locally to the internal surfaces of the steam injection chamber. Then, following the scheme in Figure 5.15, the 1D fluid network is integrated within the solid one.

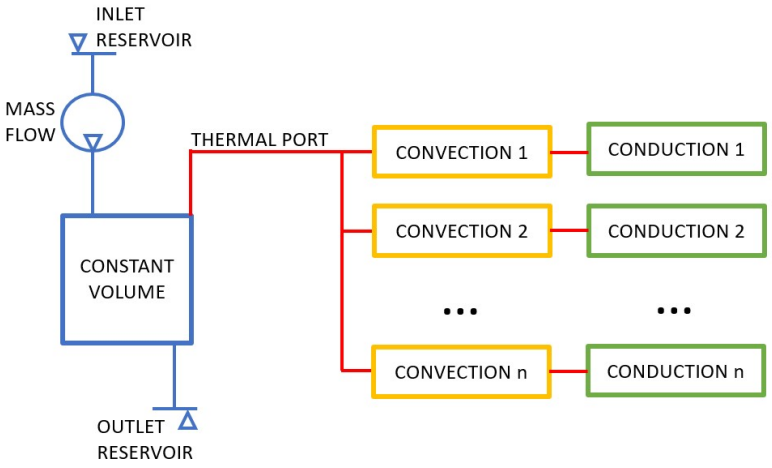

Figure 5.15
Schematic of a possible improvement of the 1D fluid network inside the steam injection domain.

The first correlation that is evident from the CFD results in Figure 5.14, is the cross-flow pipe for the first part of the bushing. This zone of the steam injection domain can be modeled as in Figure 5.16.

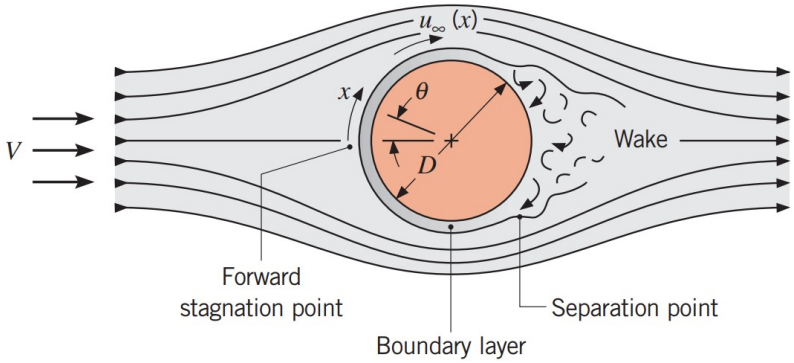

Figure 5.16
Forced convention condition for the left-hand side of the bushing.

The correlations found in [6] are two: one that includes additional constants depending on the Reynolds number and the other more general.

The first one evaluates the Nusselt number as

$$\overline{Nu}_D = \frac{\overline{h}D}{k} = CRe_D^m Pr^{1/3} \tag{5.1}$$

where C and m are constant depending on the Reynolds number as Table 5.2.

Table 5.2
Constants to be used for the correlation in cross-flow conditions for different Reynolds ranges.

Re_D	C	m
0.4 to 4	0.989	0.33
4 to 40	0.911	0.385
40 to 4000	0.683	0.466
4000 to 40 000	0.193	0.618
40 000 to 400 000	0.027	0.805

The more general correlation is:

$$\overline{Nu}_D = 0.3 + \frac{0.62Re_D^{1/2}Pr^{1/3}}{[1+(0.4/Pr)^{2/3}]^{1/4}}\left[\left(\frac{Re_D}{282000}\right)^{5/8}\right]^{4/5} \tag{5.2}$$

The correlations of equations (5.1) and (5.2) are then compared to the CFD results to assess their validity. In *Ansys Fluent*, there are two ways of measuring the heat transfer coefficient (htc) at a solid-fluid interface: evaluate it regarding the fluid-adjacent temperature or concerning a reference temperature. The first one considers the fluid temperature the one at the centroid of the fluid cell nearest to the wall, while the second one considers the temperature set by the user [34].

In the current comparison, the correct approach is the second one, and the reference temperature was set as the unperturbed fluid temperature T_∞, thus the inlet temperature. The surface of the 3D geometry considered is the part of the bushing affected by the cross-flow condition, noticeable in Figure 5.14. In Figure 5.17 are shown the results obtained in each case, along with their dependency on the mass flow rate injected in the steam injection domain, with steam as the working fluid.

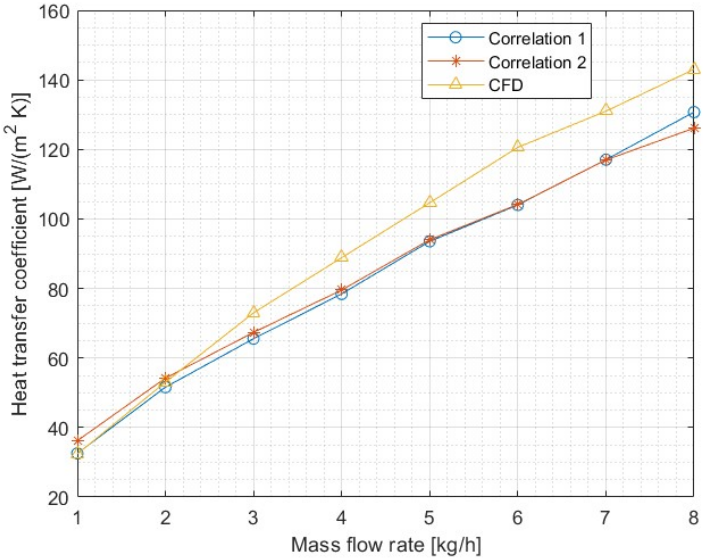

Figure 5.17
Comparison between correlations and CFD for the cross-flow condition, with steam as the working fluid.

The Reynolds numbers used for obtaining these results are shown in Table 5.3.

Table 5.3
Reynolds number for the computation of the heat transfer coefficients in Figure **??**

Mass flow rate [kg/h]	1	2	3	4	5	6	7	8
Re [-]	4963	10457	15403	20589	27383	32518	39364	44498

while the Prandtl number is dependent only on the type of fluid, considering steam at 412 °C and 1.25 bar (nominal conditions), it becomes

$$Pr = \frac{c_p \mu}{k} = \frac{1006.43 \cdot 1.79 \cdot 10^{-5}}{0.0242} = 0.74[-] \tag{5.3}$$

For the rest of the chamber, the fluid flow is characterized by strong vorticity and turbulent behavior, as can be seen from the CFD velocity vectors (figure **??**). Due to the complexity of the flow field and the lack of suitable heat transfer coefficient correlations, it has been decided to avoid this path and to try to model the fluid network with the existing *Simscape* gas blocks, exploiting the correlation for heat transfer of a pipe flow, already implemented in the software. The only correlation for the steam injection chamber that will be implemented by the author is the above-described cross-flow condition.

Therefore, the modeling of the fluid flow has been modified as shown in figure 5.18. The constant volume chamber aims to represent the cross-flow behavior at the initial part of the bushing, exchanging energy with the solids through the thermal port

H. Between the constant volume chamber and the solid block, a convection block is present, where the htc coefficient is tuned with the values obtained from the cross-flow correlation. The fluid recirculation in the rest of the volume is modeled via pipes in a configuration that imposes the path shown by the CFD study.

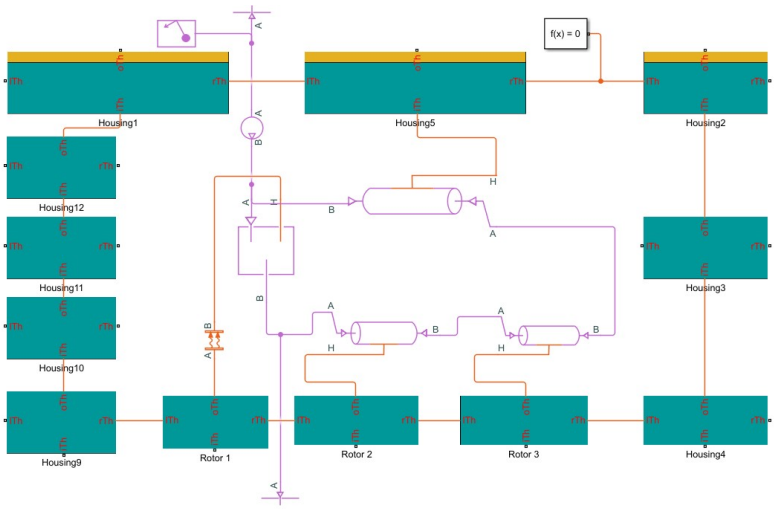

Figure 5.18

Second thermal model of the steam injection domain, with both solid and fluid networks. The fluid network is modeled with gas blocks already coded in *Simscape*.

A sensitivity analysis is performed by varying mass flow rates to asses whether the model is consistent enough. The respective results are shown in Appendix A. Although for mass flow rates lower than 2 $\mathrm{kg\,s^{-1}}$ the bushing temperature discrepancy between 1D and 3D results is below 5 %, the errors increase quickly for higher mass flow rates.

Thus, another model has been developed, without a fluid network, as shown in figure 5.19. Convection between the fluid and the solid surfaces is modeled as heat exchanged by the solids with a constant temperature source, equal to the fluid inlet temperature. In between each solid block and the constant T source, there is a convection block that defines the proper heat transfer coefficient in each specific region of the chamber. However, only one heat transfer coefficient can be reliably evaluated based on correlations, i.e. the cross-flow condition. The others have to be found by CFD simulations with a simplified geometry model and then tuned into the convection blocks of the 1D model.

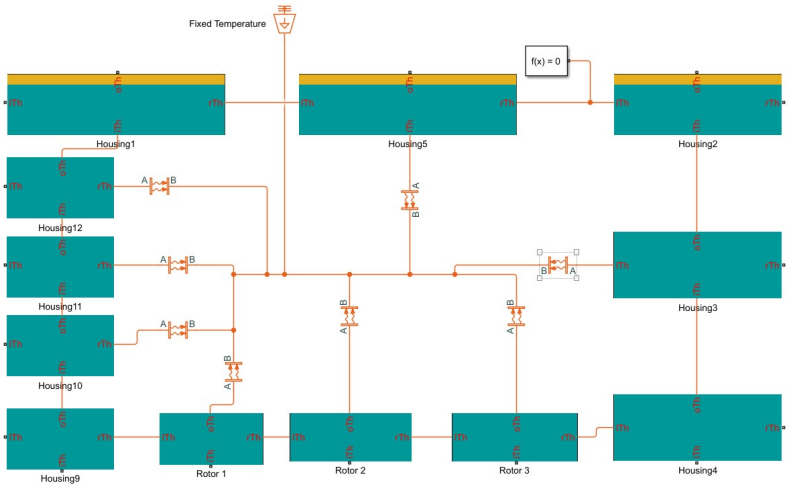

Figure 5.19

Third thermal model of the steam injection domain. The solid blocks exchange heat through convection blocks, towards a source at a constant temperature, equal to the fluid inlet temperature.

5.4 Validation with experimental data - Static test

A first experimental campaign has been performed without the shaft rotation. The CTU was fully assembled and experimental data were used for validation and comparison with the 1D and 3D simulations. The thermocouples for the experiments were located as shown in Figure 5.20, and the steam injection chamber was filled in with steam at different temperatures and mass flow rate conditions. Hence, the mass flow rates were increased to reach different Re numbers and assess the robustness of htc evaluated from the CFD and tuned in the 1D models.

However, due to the evaporator at disposal in the lab, the steam reached a maximum super-heated inlet temperature of $\approx$ 290 °C, obtained by increasing the pressure inside the chamber at 1.15 bar.

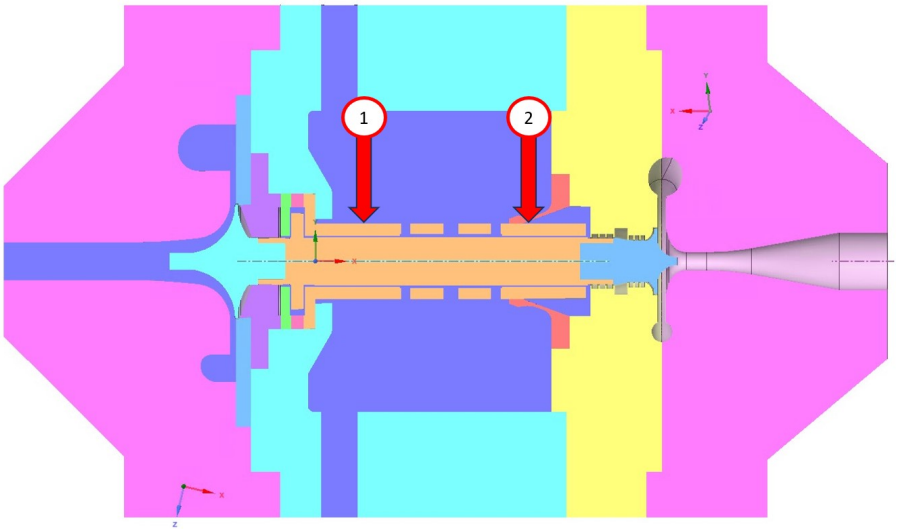

Figure 5.20
Thermal sensor positions for the experimental tests.

For what concerns the modeling part - since the gas bearings are not active - the bushing and the shaft are considered in contact, for all the static tests performed. Thus, for both the 1D and 3D models, the heat transfer mode in the gas bearings is conduction. The 3D CFD simulations were run with *Ansys Fluent* and for all the *Test Cases* and the temperatures were exported for a better post-processing with the experimental and 1D results in *Matlab*. In particular, the element under investigation is the bushing, and the temperatures at any mesh node of this component of the CFD-FEA are exported.

The materials of each component have been set up properly, with varying thermal properties against temperature. For some materials, the manufacturing company provided detailed data sheets while for others, the default material properties embedded in *Ansys Fluent* have been applied, also for the 1D model.

An additional uncertainty is related to the mass flow rate of water delivered by the pump at the evaporator. The manufacturer of the pump provided only the mass flow

rate delivered at a control voltage of 5V, and a linear interpolation has been applied to know the mass flow rates at different voltages (Appendix B). This represents a good prediction of the pump's behavior, as shown later, but still, discrepancies with the measured water flow exist.

5.4.1 Test 1

For the first test case, 1D, 3D, and experimental results are shown in Figure 5.21.

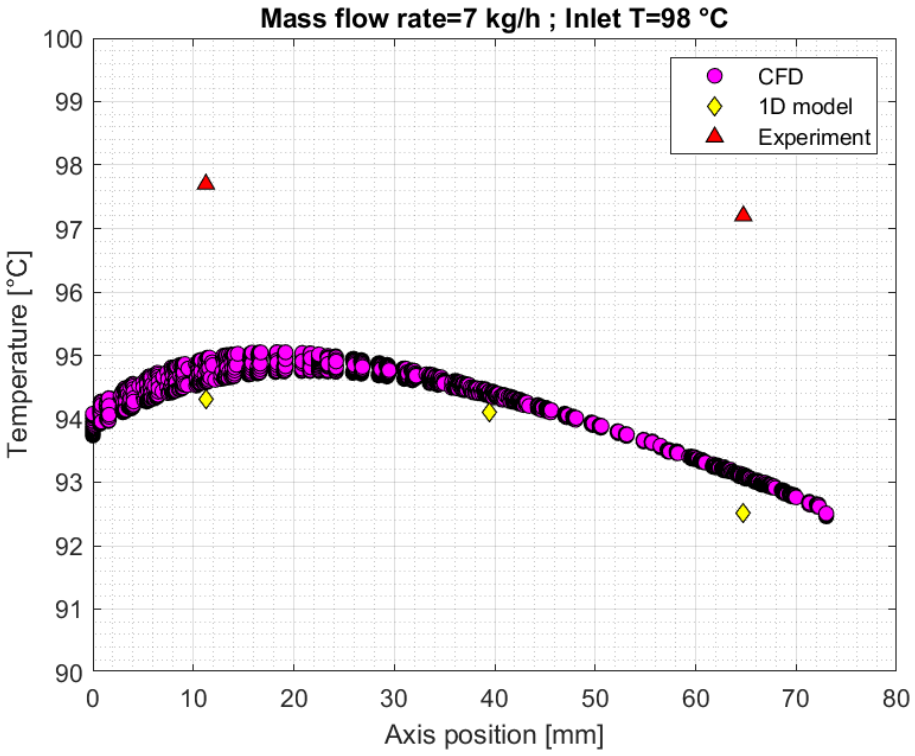

Figure 5.21

CFD, 1D and experimental comparison in the case of steam injection chamber filled in with ≈ 7 $\mathrm{kg\,h^{-1}}$ of steam at 100 °C, without shaft rotation.

For the CFD results, all the temperatures at the mesh nodes are plotted to show the minimum and maximum temperatures at a given axis position. The saturated temperature reached by the steam was ≈ 97.5 °C. The mass flow rate measured in the lab was 7.9 $\mathrm{kg\,h^{-1}}$ while the one from the linear interpolation of the pump characteristic is 6.3 $\mathrm{kg\,h^{-1}}$ (0.8 V of pump control voltage). The one used in the simulation is 7 $\mathrm{kg\,h^{-1}}$.

The 1D and the CFD results are very close, a good sign that the htc values were correctly computed from CFD and properly tuned in the 1D model. Regarding the experimental results, they show good agreement with the models, with a maximum relative error of ∼ 3.1 %. The differences can be due either to the uncertainties of the materials' properties, or the uncertainty regarding the mass flow rate of water sent to the evaporator by the pump.

5.4.2 Test 2

For the second test case, the mass flow rate is increased up to 8 $\mathrm{kg\,h^{-1}}$ (1.014 V of pump control voltage) but the measured one was 7.5 $\mathrm{kg\,h^{-1}}$. 1D, 3D and experimental results are shown in Figure 5.22.

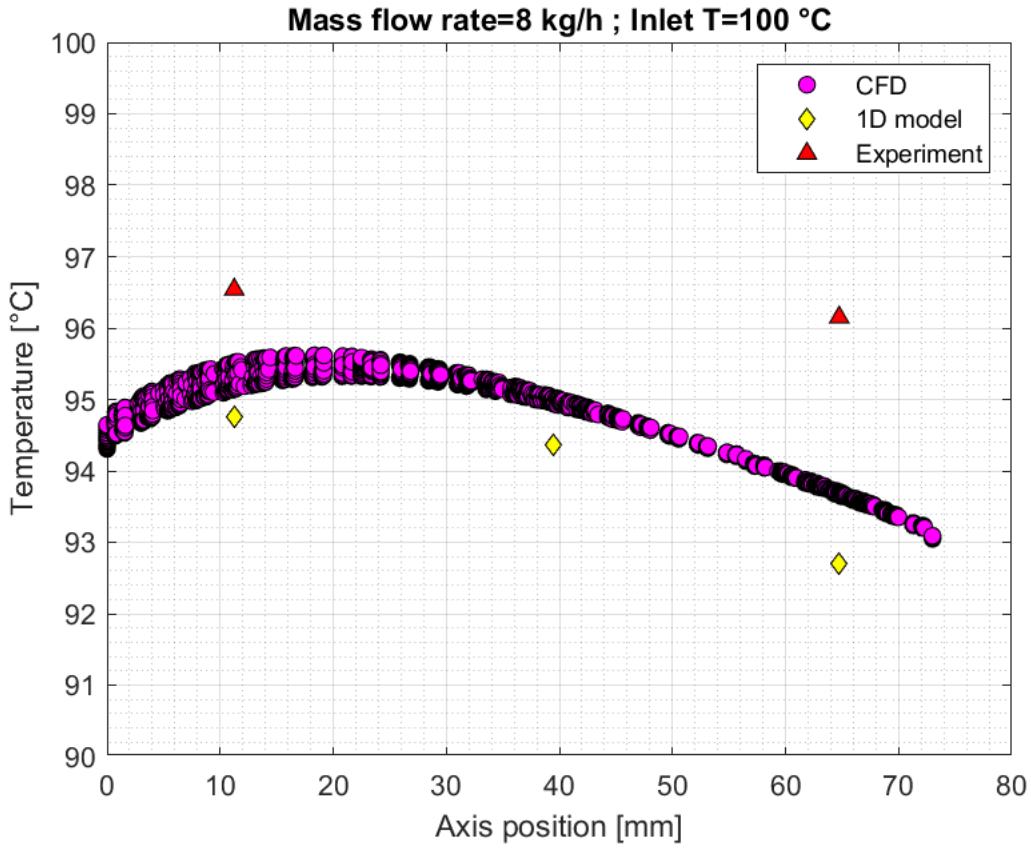

Figure 5.22

CFD, 1D and experimental comparison in the case of steam injection chamber filled in with ≈ 7.5 $\mathrm{kg\,h^{-1}}$ of steam at 100 °C, without shaft rotation.

The same conclusion of *Test 1* holds, but a maximum error of ~ 2.1 % is reported. Hence, the 1D model seems to be robust concerning inlet mass flow rate variations at the steam injection, but further assessments are needed.

5.4.3 Test 3

For the third run, the mass flow rate increases up to 15.8 $\mathrm{kg\,h^{-1}}$ - 2 V of control voltage - and the measured one was 17.4 $\mathrm{kg\,h^{-1}}$ (relative error of 9.1 %). 1D, 3D and experimental results are shown in Figure 5.23.

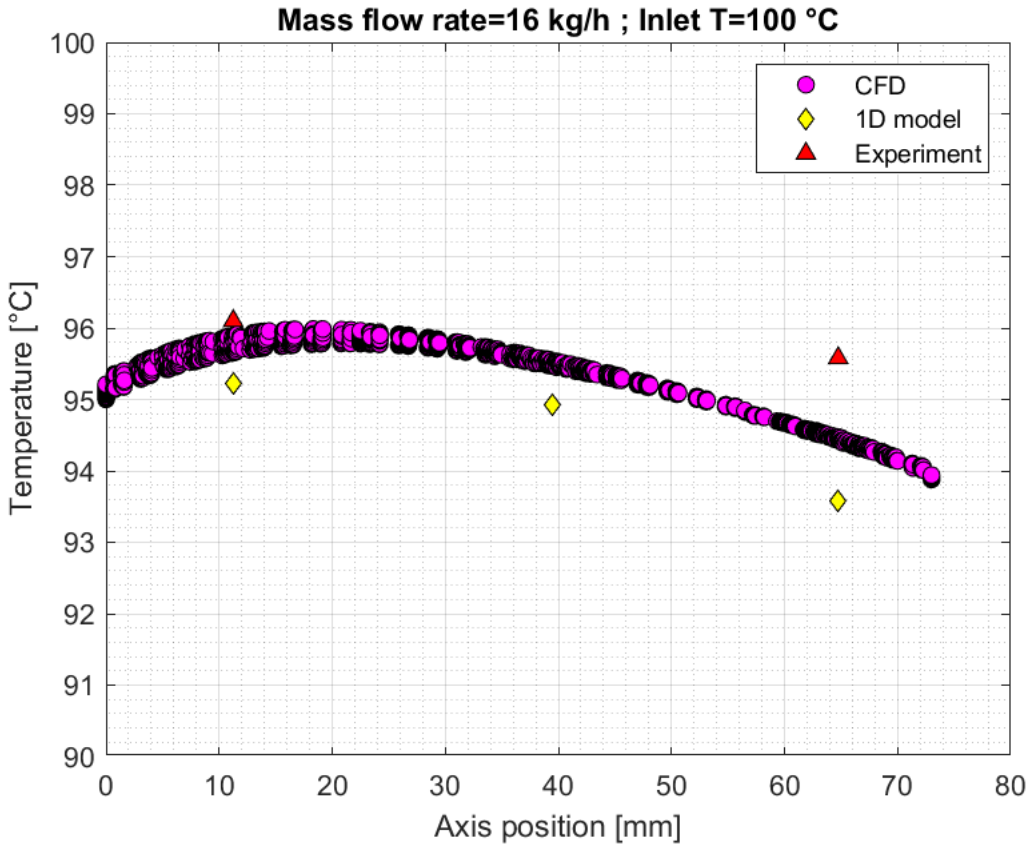

Figure 5.23

CFD, 1D and experimental comparison in the case of steam injection chamber filled in with ≈ 16 $\mathrm{kg\,h^{-1}}$ of steam at 100 °C, without shaft rotation.

With this test, the sensitivity analysis concerning the mass flow rate at the inlet of the steam injection chamber can be considered carried out. The first probe shows a relative error of 1 % to the 1D results while It overlaps with the CFD results. The second probe shows an error of 2.1 % to 1D.

5.4.4 Test 5

Test 4 is not reported since is not useful for the steady-state validation of the models: during this test, the thermal dynamic behavior of the machine was investigated during the cool-down phase, hence no steam injection was present.

For the fifth test case, the control voltage was reduced at 0.5V, corresponding to 3.95 $\mathrm{kg\,h^{-1}}$ according to the linear interpolation of the characteristic of the pump, and the measured one was 2.8 $\mathrm{kg\,h^{-1}}$, which again represent a big discrepancy. For the CFD simulation a mass flow rate of 4 $\mathrm{kg\,h^{-1}}$ is imposed.

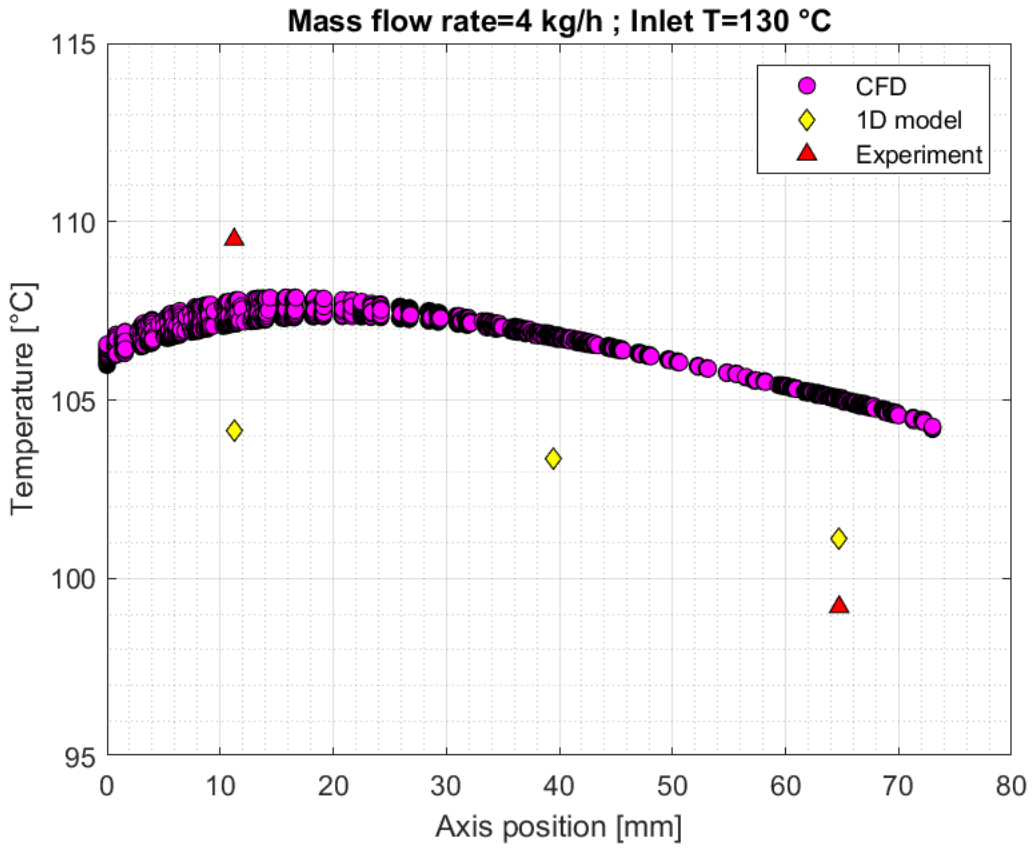

Figure 5.24

CFD, 1D and experimental comparison in the case of steam injection chamber filled in with ≈ 3.5 $\mathrm{kg\,h^{-1}}$ of steam at 130 °C, without shaft rotation.

Firstly, a strange behavior of the right temperature probe is spotted, with respect to *Test 1, 2* and *3*. Indeed, for all the previous tests, the temperatures measured were placed above the ones obtained from simulations, hence the T gradient is steeper in the actual case (assuming that no experimental errors occurred). Additionally, the uncertainty played by the water mass flow rate represents a big question mark, but let us analyze its impact in the next graph.

It may be interesting to analyze all the runs in a single chart. Thus, the CFD results of Test 1, Test 2, Test 3, and Test 5 are shown in figure 5.25.

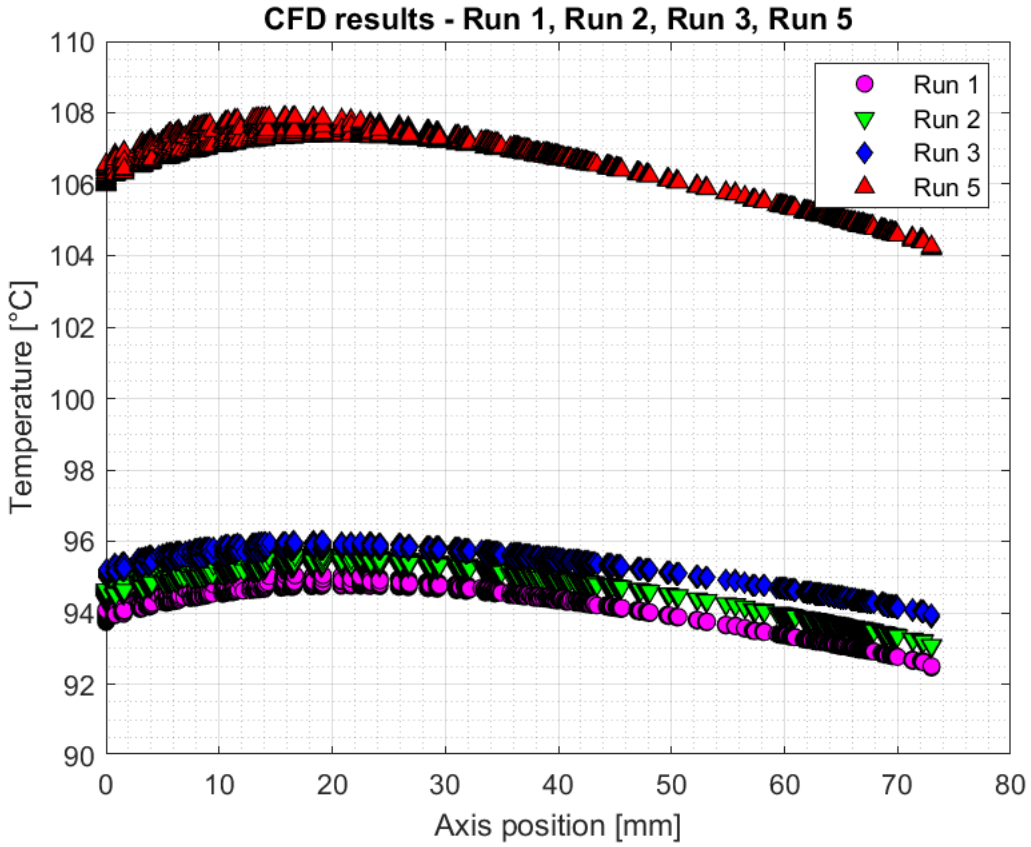

Figure 5.25
CFD results of Test 1, Test 2, Test 3, Test 4 in terms of temperature gradient across the rotor shaft.

One notices that for the first three runs - where the mass flow rate is varied and the inlet temperature of the steam is kept constant - the temperatures are close in the three cases, at any position of the shaft. On the contrary, when the inlet temperature is set at 130 °C for the fifth run, the temperatures change to a major extent, but keeping the same gradient along the shaft. This phenomenon is also beneficial in the experimental campaign since the error between the measured pump mass flow rate and the one derived from the characteristic curve does not play an extremely important role.

5.5 Experimental validation - Dynamic test

5.5.1 Gas bearings

To model the windage losses generated in the gas bearings during shaft rotation, the models described in section 2.4 are first of all compared.

The geometrical parameters for both axial and radial bearings are listed in Table 5.4. For the nomenclature used, refer to Figure 2.9 and Figure 2.14.

Table 5.4
HGJB and SGTB geometric parameters necessary to compute the windage losses.

	α [-]	γ [-]	h_g [µm]	h_r [µm]	R_o [mm]	R_g [mm]	R_i [mm]
HGJB	0.68	0.89	16	9	8	-	-
SGTB	0.53	0.74	24	19	32.6	28.1	17

The geometrical parameters listed are not constant during operation: the centrifugal forces are going to affect the clearance on the radial bearings. Additionally, the clearance at the axial bearings is modified depending on the thrust difference between the compressor and the turbine impellers. However, as a first approximation, these dimensions are considered fixed. For the evaluations of the losses, water vapor, at 412 °C and ambient pressure, has been used as the working fluid.

Firstly, the models for the HGJB windage losses (explained in subsection 2.4.1) are compared up to 250 krpm, and the graph is shown in Figure 5.26.

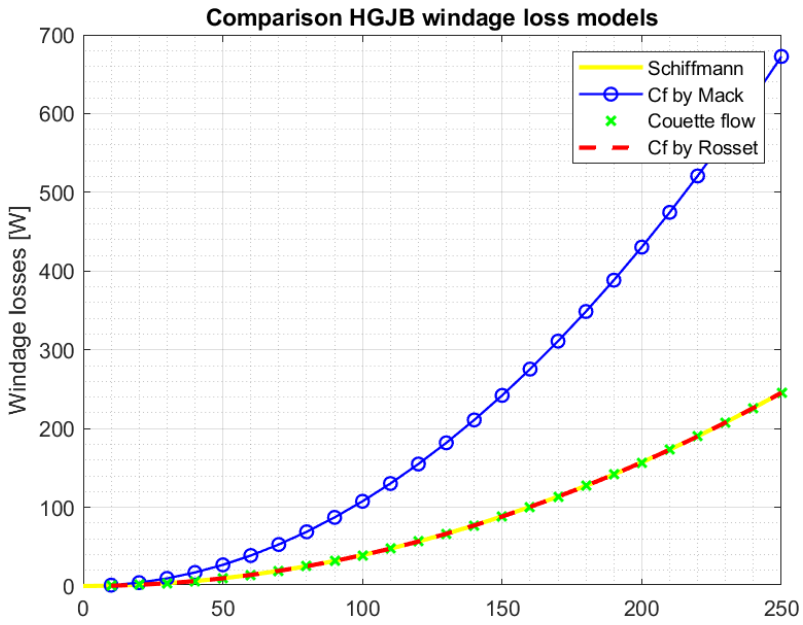

Figure 5.26
Comparison among the different windage loss models for the HGBJ.

Mack's [26] model highly overestimates the windage losses as soon as the rotational speed overtakes 50 krpm, while Schiffmann [2], Rosset [24], and Couette's models overlap with each other, with less than 1 W of error at 250 krpm. Since the different models prove the regime in the gas bearing gaps is laminar, it is well predicted by Equation (2.52) (Couette flow) and by Rosset's model in laminar condition (Taylor-Couette flow, Eq. (2.53)), while Mack's model Eq. (2.57) is not appropriate in this case.

Regarding the SGTB, the models for the viscous loss generation are described in subsection 2.4.2. The models of Schiffmann [2], Daily [27], and Rosset [24] are compared in Figure 5.27 as a function of the rotational speed, up to 250 krpm. Schiffmann and Rosset's models show numerical agreement in the range considered, therefore the hypothesis of laminar flow is again consistent.

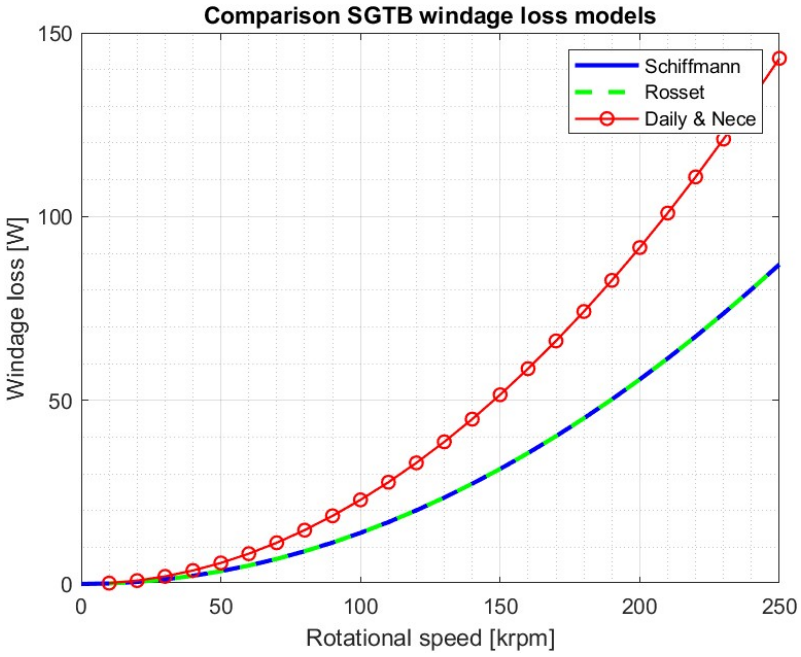

Figure 5.27
Comparison among the different windage loss models for the SGTB.

The windage losses at the nominal CTU speed of 210 rpm are shown in Table 5.5. The windage loss generated in the sleeve gap between the two radial bearings is also reported, to highlight its negligible impact, due to the gap dimension of the order of mm.

Table 5.5
Windage losses for HGJB and SGTB, and the sleeve between the two radial bearings, ate the nominal rotational speed of 210 krpm.

Windage losses [W]					
HGJB LEFT	SLEEVE	HGJB RIGHT	SGTB 1	SGTB 2	Total
173.2	1.32	173.2	61.4	61.4	470.5

5.5.2 Thermal model and Dynamic experiments

The dynamic experiments, i.e. experiments where the shaft is put under rotation while the steam injection chamber is filled in, had as main concerns the pressure distribution and calibration in locations of interest. However, useful information for thermal management was found. The temperature sensors were placed in the same positions as for the static test (see Figure 5.20).

In particular, the boundary conditions for one of these tests can be found in Table 5.6, where the corresponding mass flow rate is evaluated according to the linear interpolation of the pump's characteristic at 0.5 V.

Table 5.6
Boundary condition for the dynamic experiment, the one of interest for the thermal management.

Rotor Speed [krpm]	Inlet T [°C]	Mass Flow Rate [kg/h]
30	130	4

The values of the windage losses at 30 *krpm* are reported in the graphs in figure 5.28.

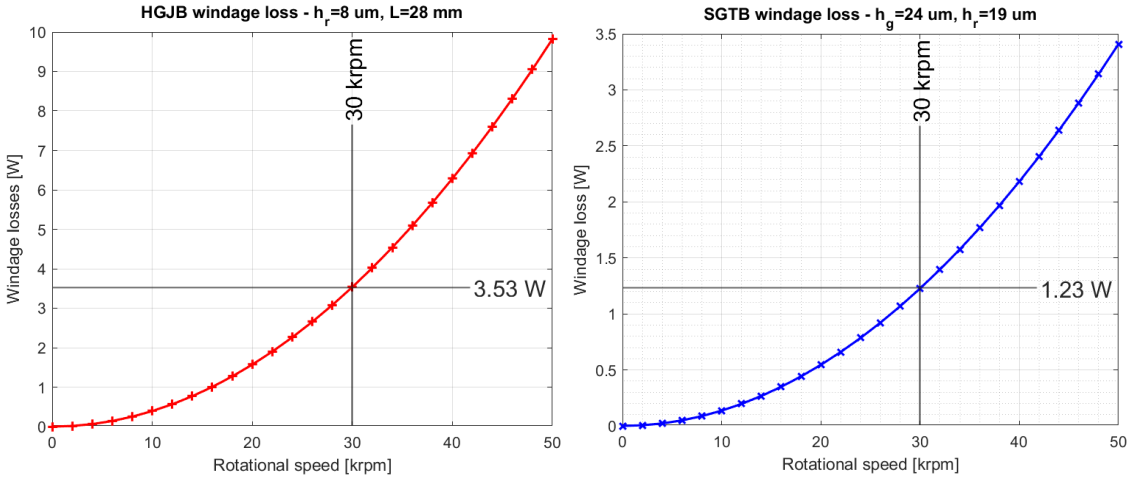

(a) **(b)**

Figure 5.28
Windage losses for radial (a) and axial (b) bearings, highlighting the values at 30 *krpm*.

In Figure 5.29 the temperature gradients on the bushing and the rotor are displayed. Only the experimental value at the level of one radial bearing has been plotted since the other one has a relevant error. Indeed, the temperature measured on the bushing at the level of the other radial bearing is 88 °C, against ≈ 110 °C computed from the simulations. However, this error was motivated when the experimental set-up was dismounted. The engineers noticed that the T-sensor of the turbine-side HGJB was not touching the bushing, hence the temperature measured was the one of the fluid rather than the solid one. This scenario could happen also for the static test 5 (see subsection 5.4.4) due to the weird behavior of the same T-sensor.

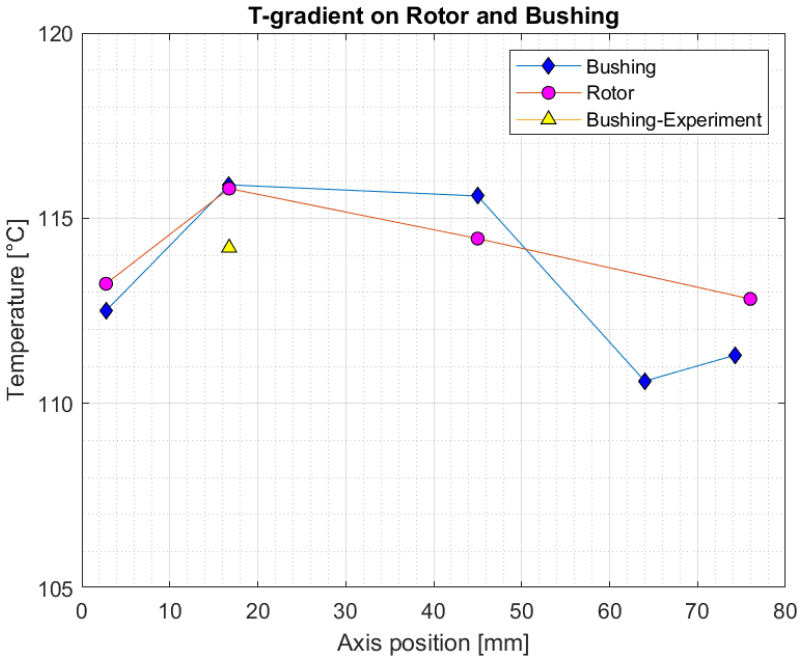

Figure 5.29
1D and experimental comparison with inlet mass flow rate of 4 $\mathrm{kg\,h^{-1}}$, inlet temperature of 130 $^{\circ}\mathrm{C}$ and rotational speed of 30 krpm.

5.6 Complete thermo-mechanical model

5.6.1 Thermal analysis

A complete thermal model was developed to predict the temperature evolution of the CTU under nominal conditions, but the experimental set-up for direct comparison was not ready yet. In the model, the compressor and turbine domains are embedded, along with the gas bearings blocks, and the heat transfer coefficients in the convection blocks were tuned according to nominal boundary conditions at the inlet of the steam injection of 8 $\mathrm{kg\,h^{-1}}$ and 412 °C.

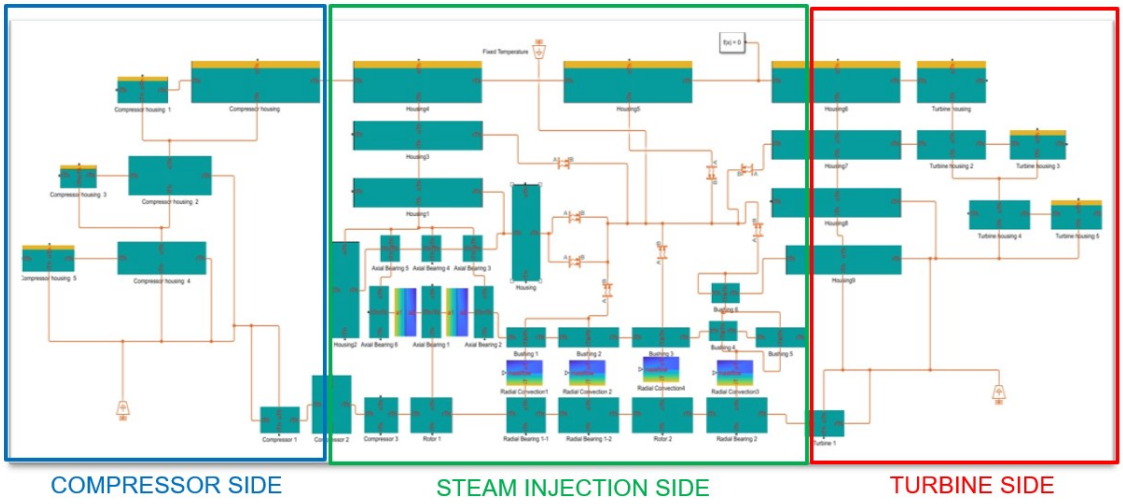

Figure 5.30
Complete 1D thermal model of the CTU. The three sub-domains are highlighted for the sake of clarity.

In figure 5.30, It is possible to see the final lumped parameters model built in Simscape. Concerning the boundary conditions at the compressor and turbine volute's wall, fixed temperatures were applied, also called Dirichlet boundary conditions. The volute's heat transfer correlation was not used since it has been noticed that a change of thermal effects in these areas would not lead to a big difference in the temperature of the critical regions, such as the gas bearings. Olmedo et al. [3] discussed also this aspect, claiming that in high-speed turbomachinery, using the fluid temperature as a constant boundary condition for the impeller wheel and volute, provides a good approximation for the overall estimation of the machine temperatures.

A first investigation was carried out by focusing on the temperature gradient across the bushing for different rotational speeds and hence different windage losses. In figure 5.31 are shown the results for rotational speeds starting from 0 $krpm$, and linearly brought up to 150 $krpm$, with a step of 30 $krpm$.

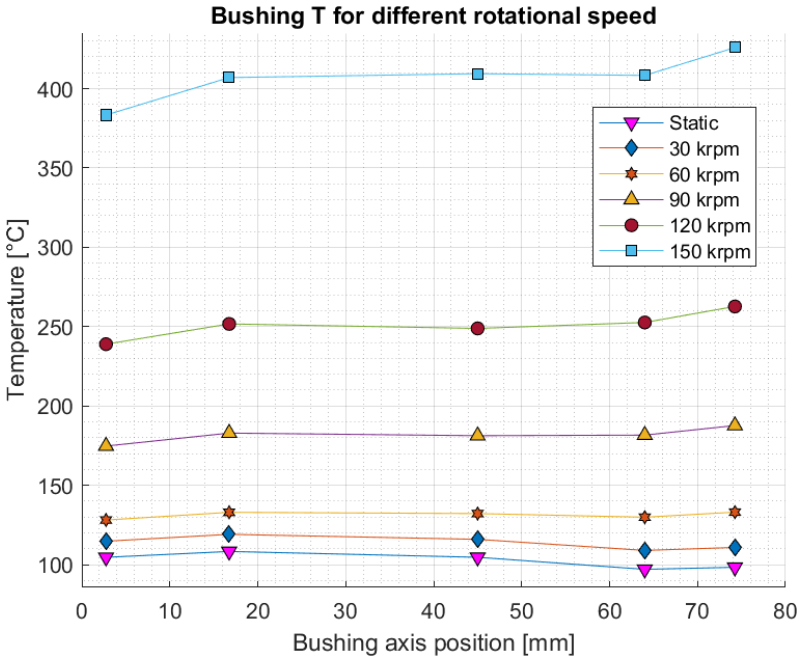

Figure 5.31

Dependency of the bushing temperature gradient upon the rotor shaft speed, for nominal steam injection condition of 8 $\mathrm{kg\,h^{-1}}$ and inlet temperature of 412 °C.

It can be noticed that as the shaft speed increases linearly, the temperature profile does not. This effect is related to the exponential relationship of the windage losses with respect to the rotational speed, and in particular, a parabolic link exists, as described by Schiffmann's model in subsection 2.4.1.

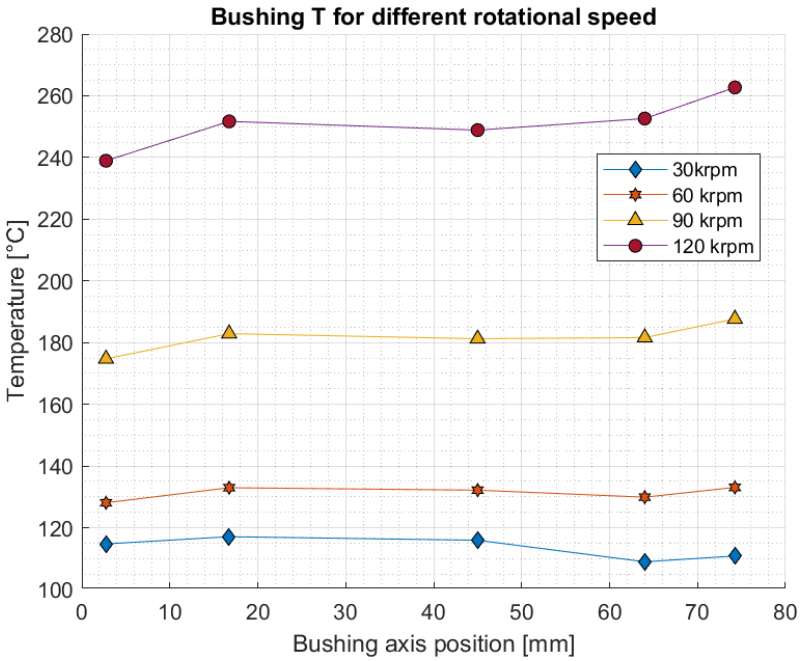

Figure 5.32

Dependency of the bushing temperature gradient upon the rotor shaft speed.

In Figure 5.32 the difference in temperature along the rotational axis of the bushing for a smaller range of rotational speeds is shown. From this perspective, it is more evident how the temperature gradient along the bushing axis has steeper behavior for increasing rotational speeds. This can be explained by the better capability of the left-hand side of the steam injection chamber to get rid of the windage losses since that region is directly under the steam injection inlet, hence the convective heat transfer is enhanced due to steam direct impingement on the bushing.

Finally, figure 5.33 shows the temperature on the bushing and rotor for the nominal condition of the steam injection (8 $\mathrm{kg\,h^{-1}}$ and inlet temperature of 412 °C) and nominal rotational speed of 210 krpm. These results will be used as thermal boundary conditions for the assessment of the expansions in critical areas in the next section.

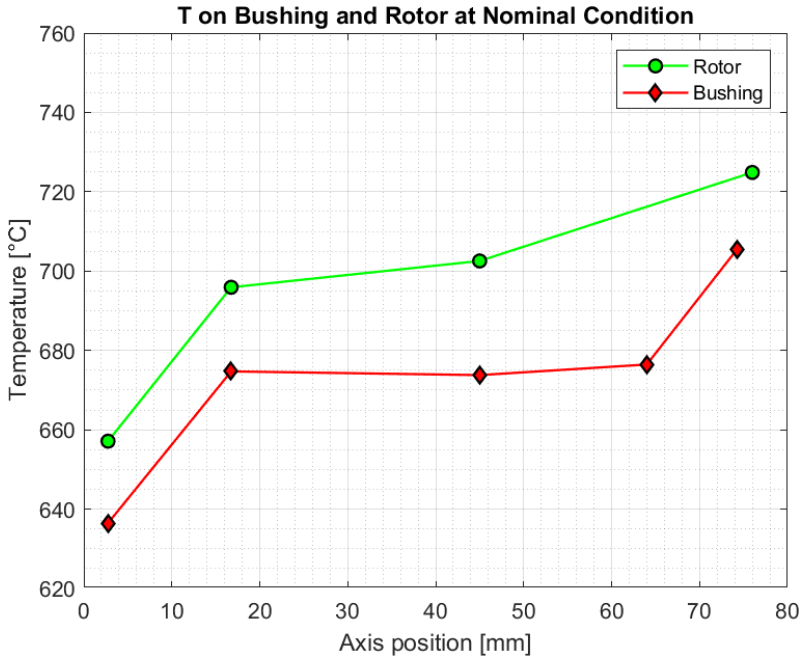

Figure 5.33

Temperature gradient across the rotor and bushing for nominal steam injection inlet conditions (8 $\mathrm{kg\,h^{-1}}$ and temperature of 412 °C) and nominal rotational speed of 210 krpm.

5.6.2 Thermo-mechanical analysis

The temperature profiles found by the simulations reported in subsection 5.6.1 are used as boundary conditions for the mechanical problem, which theory is reported in subsection 3.3.4. The representation of the 1D model in Simscape is reported in figure 5.34. The same blocks were used for the rotor and bushing, just changing properly the dimensions and boundary conditions between the two components.

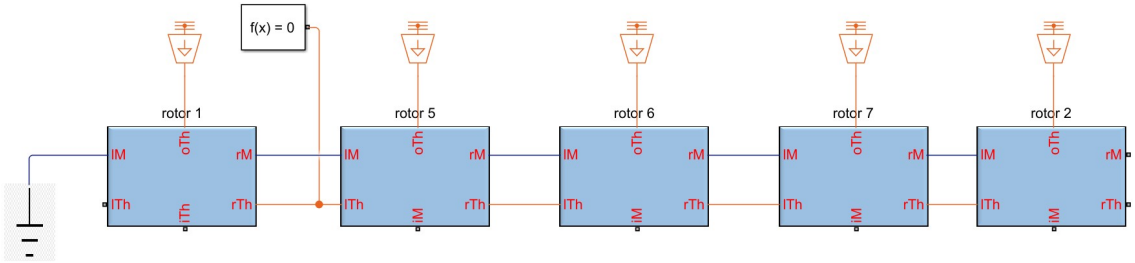

Figure 5.34
1D thermo-mechanical model in Simscape, used both for rotor and bushing.

The expansion results are reported in figure 5.35: the bushing ones just account for the thermal effect while the rotor ones are due to the coupling of high temperatures and centrifugal forces at 210 *krpm*.

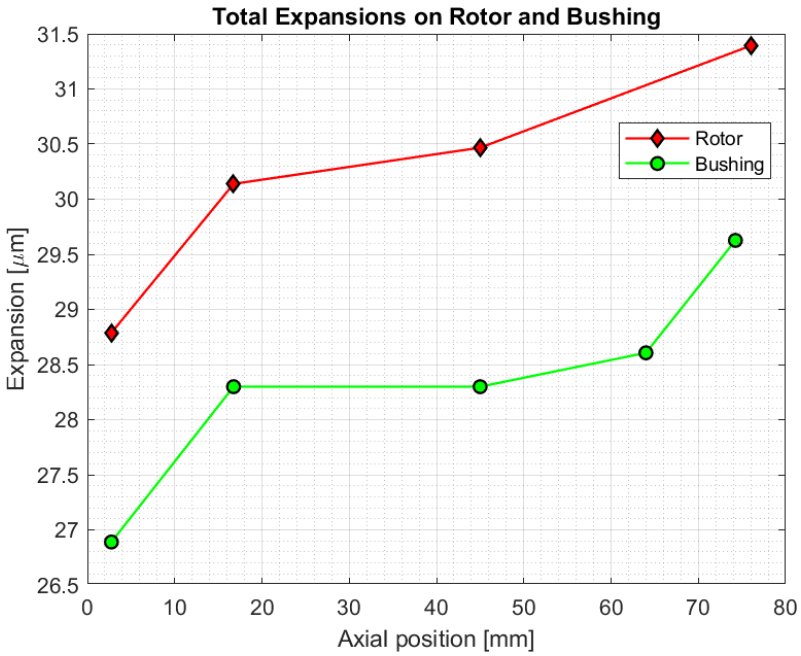

Figure 5.35
Expansions on rotor and bushing at nominal working conditions.

As can be noticed, the rotor expansions are bigger than the bushing ones, leading to possible mechanical seizure during operation. Another interesting aspect is that - due to the high temperature affecting the rotor - the centrifugal forces only cause around 3.3 % of the total rotor expansions. In fact, the centrifugal expansion at 210 *krpm* for a rotor of 8 mm of radius is 0.946 µm, against total expansions of around 30.5 µm, due to the superposition of the thermal expansions. However, this behavior is beneficial since in a configuration where the rotor and bushing are kept at the same temperatures, the high centrifugal forces do not represent a critical condition.

The gap reduction in the HGJB is analyzed in detail in figure 5.36. The *red area* shows the radial gap reduction due to bigger rotor expansions than the bushing

ones, while the green area shows the remaining gap with respect to the normalized length of the rotor and bushing. As can be seen, the remaining gap is constant with respect to the axis position, a good result for what concerns the dynamic stability provided by the gas bearings. As a conclusion of this study, It can be stated that no mechanical seizure is expected in the radial bearing gaps.

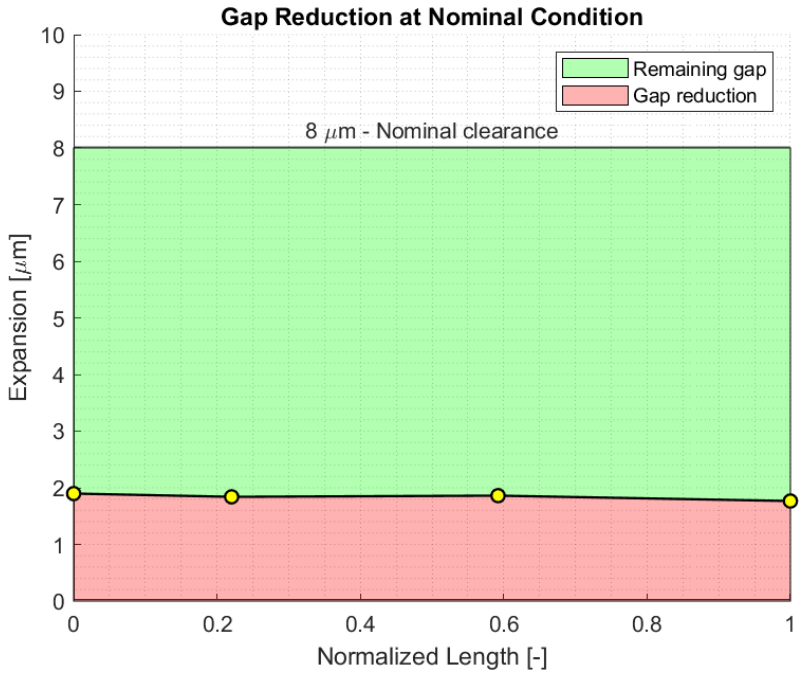

Figure 5.36

Remaining gap and gap reduction of the HGJB due to expansion effects, with respect to axis position.

Chapter 6

Discussion and Future Works

6.1 Discussion

The research aims to provide a validated thermal model of a high-speed gas bearings-supported compressor turbine unit. The requirements of the model are robustness with varying boundary conditions, enough detail in regions where temperature gradients are of special interest, and high computational speed, to be run along with experiments.

The study started with a deep analysis of the heat transfer modes along with a comprehensive study of the current state of the literature for thermal management in high-speed turbomachinery and electric motors. Additionally, particular attention was paid to the gas bearings in terms of clearance and windage loss generation which must be carefully modeled.

The 3D approach using CFD and FEA simulations resulted in not matching the target of the research: not only those methods are highly computationally demanding, but faced issues with the complex geometry that is characterized by different orders of magnitude in terms of dimension, going from mm to µm. However, a 3D simplified model has been established and exploited to help assess other relevant parameters related to thermal management (e.g. heat transfer coefficients).

The approach chosen was the 1D modeling based on a lumped parameter approach, whose goal is to simplify the thermal problem based on the electrical network analogy ruled by the Kirchoff laws. Two 1D models can be connected to generate a 2D model of the machine. This approach has been already used in the literature [3], [33], and it was shown to be fast and reliable, especially for axis-symmetric geometries.

The study started with the validation of the solid components of the 1D model, hence conduction heat transfer mode, by comparing 1D simulations, with different boundary conditions, with FEA simulations performed in *Ansys Mechanics*. Additionally, the transient state of the thermal problem due to the thermal inertia of the solid components has been validated, again comparing the 1D with FEA results.

The analysis then moved on, increasing the level of complexity, and coupling the solid network to the fluid one. The starting point was the fluid network of the steam injection chamber, which is meant to be filled in with high-temperature steam. The injected steam aims to feed the gas bearings and flatten out the temperature gradient on the middle part of the CTU, due to the different working temperatures of the turbine and the compressor sides.

Different fluid network configurations were tried. In terms of steady-state conditions, all of them worked quite well compared to CFD when the mass flow rate of the steam was either null or low concerning the design one. Hence, all the models are not able to predict the thermal effects of the 3D flow – which is highly asymmetric – in the case the designed mass flow rate is imposed. The complex flow path inside the steam injection chamber is characterized by turbulence and strong vorticity, leading to complex thermal behavior that is difficult to predict using a 1D approach. Additionally, due to the complex and unique geometry of the steam injection chamber, the evaluation of the heat transfer coefficients based on existing correlations is very challenging. For the same reason, it was not possible to establish a 1D model able to predict the transient thermal state of the CTU.

Therefore, a coupled 1D and 3D approach has been chosen. In particular, a simplified CFD model has been built to evaluate the heat transfer coefficients on the surfaces of interest and apply them to the 1D model. The simplified 3D CFD model takes around 10 minutes to run and reach convergence. This approach showed high reliability with experimental results in the case of static conditions, i.e. without rotation of the shaft, for different sets of boundary conditions tested.

The temperature profile on the rotor and bushing foreseen by the 1D model at nominal conditions were then used to check thermo-mechanical expansions of those components. The analysis showed very low expansion due to centrifugal forces on the rotor with respect to the thermal ones. However, due to the small temperature difference between the bushing and the rotor at the same axis position, the thermal expansions at the facing surfaces of the two components were close. In the end, a gap reduction of 2 µm, constant along the rotational axis, is expected: 1 µm of reduction due to centrifugal force expansion and 1 µm for the temperature difference between the bushing and the rotor (T higher on the rotor). Finally, thanks to this result, no mechanical seizure in the gas bearings at nominal conditions is foreseen.

6.2 Future works

A complete thermal management and assessment of the machine under study would comprehend additional theoretical and experimental analysis. First of all, the transient behavior of the CTU should be addressed. In particular, It is necessary to understand if the co-simulation approach would be suitable for this purpose as well. This means that the heat transfer coefficients found from the CFD simulations must be explored in time-dependent simulations. If either the transient state of the htc is small or if it shows steadiness, the integrated 1D-3D model would work.

The dynamic simulations explained in the last part of the result section consider the windage losses constant. Hence, the gap clearance of the gas bearings is considered at the nominal value of 8 micrometers and the gap reduction due to thermal effects and centrifugal forces is not taken into account. For a complete study, this aspect has to be checked, firstly in terms of the temperature difference between the bushing and the rotor with variable gaps, and secondly the gap reduction due to expansions. If the analysis results in terms of the temperature difference between the bushing

and rotor show the same difference as the study of the current thesis, the mechanical seizure is avoided. This is because, as was shown by this study, the centrifugal forces just represent 3 % of the total expansion on the rotor, due to the high effect of the thermal expansions. Thus, if the temperature difference is kept close to constant, mechanical seizure is avoided in any working conditions. The strong dependency of the windage losses on the gap clearance can be seen in figure 6.1 and figure 6.2.

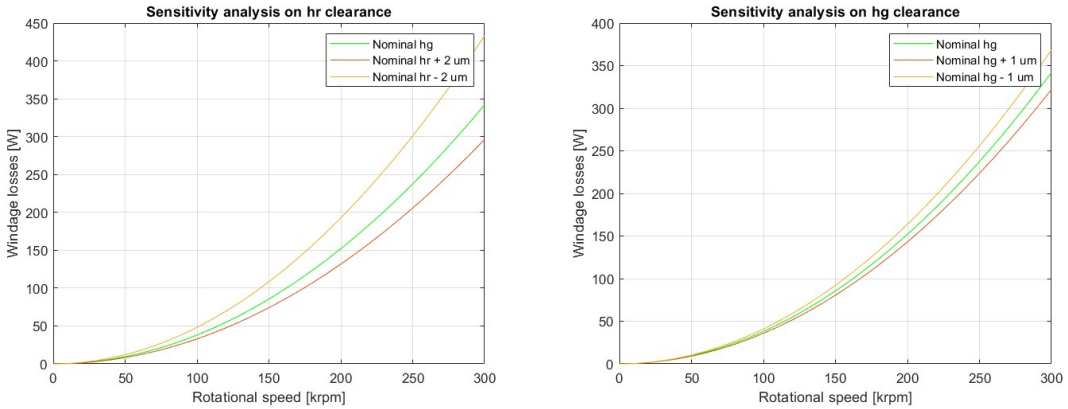

(a) **(b)**

Figure 6.1
Sensitivity analysis of HGJB windage losses as a function of h_r and h_g radial clearances.

Figure 6.2
Windage losses [W] of the HGJB as a function of radial clearance [μm] and shaft rotational speed [krpm].

The gap reduction might influence the rotor stability and damping actions. Dynamics was not something dug out by this work, but it is coupled with expansion and gap

reduction. Therefore the dynamic behavior should be assessed for a range of clearance values. Moreover, the thermo-mechanical analysis should be extended to other critical areas, such as the axial bearings and the blade tips.

For what concerns the thermal problem, additional research should be performed for the dynamic simulation results, as well as for different rotor speed conditions. Along with this, the experimental setup of the right probe sensor at the level of one of the radial bearings has to be properly checked while mounting the test rig. Finally, experiments with both the compressor and turbine spinning must be assessed, to see if the thermal boundary conditions at the compressor and turbine volute walls of the current study are reliable enough.

Chapter 7

Conclusion

The final goal of the research was to explore the capability of the 1D approach to thermo-mechanical problems, rather than heavy-computational methods, as finite volumes and elements. To assess the limitations of the 1D networks, several simulations and experimental tests were performed, for all three heat transfer modes. Regarding convection, a methodology employing coupled 1D and CFD simulations was found to be the most reliable, for a broad range of mass flow rates. Limitations and ways of improvement were dug out for the conjugated heat transfer problem under investigation.

Starting from the first results obtained, the 1D conduction network showed good reliability in terms of heat transfer and temperature distributions, for both steady and transient states. The resistance network is dependent upon the material of the solid components, and once the size of the shells is set up properly, a fast thermal network can be built. No limitation in the transient state problem occurred during the validation phase, hence this approach is broad and suitable for different types of assessments. The biggest error was spotted at the level of the internal heat generation solid block. Still, other analytical equations were not applied for this condition, since it was out of the scope of the research: the CTU under assessment does not have internal heat generation components such as an electric motor. However, the error was about 5 % for temperatures, an acceptable result while dealing with thermal problems.

As far as the fluid network was taken into account, issues started to arise. The main reason is that 1D/2D modeling is well suited if the investigation deals with axial-symmetric problems. In the current study, it was the case for the solid parts, but not for the fluid flow developed when a mass flow rate different from zero was set up at the inlet of the steam injection chamber. On the other hand, when the mass flow rate was equal to zero, and the flow inside the chamber was driven only by the buoyancy effect, good agreements were obtained from the validations. To find a final compromise and solution for the steam injection model, three fluid networks were built, and the last one resulted to be the more accurate, for a broad range of mass flow rates. In particular, a co-simulation approach was followed by tuning the heat transfer coefficient, found with a simplified CFD model, in the 1D network. The results of the 1D model showed a good match with CFD simulations and the available experimental results, for a wide range of boundary conditions.

For what concerns the complete model, it was shown that the windage losses are not negligible for small clearance gaps characterized by high rotational speeds. In

particular, since the windage losses have a parabolic dependency on the rotational speed, the temperature increase on the rotor and bushing, as a function of the rotational speed, follow an exponential path.

The temperature profile obtained for nominal conditions was then used to assess the thermal expansions on the radial bearings. The expansions due to centrifugal forces were shown to be negligible compared to the thermal ones, due to the high temperature achieved during operation. Hence, when focusing on gap reduction, thermal expansions play 50 % of the role. The thermal expansion of the bushing just differs by one micrometer less than the one of the rotor, due to the very close temperature for a given axis position of the two components. Finally, no mechanical seizure in the HGJB radial bearings was foreseen for nominal working conditions.

Appendices

Appendix A

Sensitivity Analysis 1

Table A.1
Sensitivity analysis 1 - mass flow rate of 0.36 [kg/h]

Mass Flow Rate: 0.36 [kg/h]				
		Temperature [°C]		
		HGJB 1	SLEEVE	HGJB 2
1D Model		126.4	121.4	116.2
CFD	Max T	126.6	125.8	121.3
	Min T	123.3	121.5	118.8
	Avg T	125.4	123.6	120.1
Relative Error [%]		0.8%	1.8%	3.3%

Table A.2
Sensitivity analysis 1 - mass flow rate of 1 [kg/h]

Mass Flow Rate: 1 [kg/h]				
		Temperature [°C]		
		HGJB 1	SLEEVE	HGJB 2
1D Model		148.5	144.5	141.1
CFD	Max T	152.0	151.5	147.8
	Min T	148.6	147.8	145.4
	Avg T	150.7	149.7	146.6
Relative Error [%]		1.5%	3.5%	3.8%

Table A.3
Sensitivity analysis 1 - mass flow rate of 2 [kg/h]

Mass Flow Rate: 2 [kg/h]				
		Temperature [°C]		
		HGJB 1	SLEEVE	HGJB 2
1D Model		192.9	187.9	183.8
CFD	Max T	201.2	200.1	194.2
	Min T	195.9	194.3	190.6
	Avg T	199.0	197.2	192.5
Relative Error [%]		3.1%	4.7%	4.5%

Table A.4
Sensitivity analysis 1 - mass flow rate of 3 [kg/h]

Mass Flow Rate: 3 [kg/h]				
		Temperature [°C]		
		HGJB 1	SLEEVE	HGJB 2
1D Model		219.7	208.2	201.8
CFD	Max T	232.4	231.3	224.0
	Min T	226.1	224.2	219.7
	Avg T	230.0	227.7	222.0
Relative Error [%]		4.5%	8.6%	9.1%

Table A.5
Sensitivity analysis 1 - mass flow rate of 4 [kg/h]

Mass Flow Rate: 4 [kg/h]				
		Temperature [°C]		
		HGJB 1	SLEEVE	HGJB 2
1D Model		229.8	212.2	205.5
CFD	Max T	247.4	246.4	238.4
	Min T	240.7	238.6	233.8
	Avg T	244.9	242.5	236.2
Relative Error [%]		6.2%	12.5%	13.0%

Appendix B

Second appendix

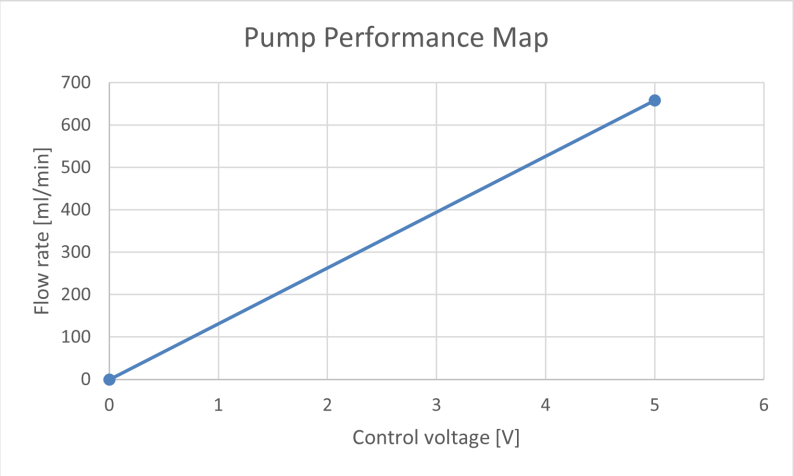

Figure B.1

Bibliography

[1] *EPFL LAMD internal reports*. Ecole Polytechnique F ed erale de Lausanne (EPFL).

[2] Jürg Schiffmann. *Integrated Design, Optimization and Experimental Investigation of a Direct Driven Turbocompressor for Domestic Heat Pumps*. Ecole Polytechnique Federale de Lausanne, 2008.

[3] LE Olmedo et al. 'Thermal management for gas lubricated, high-speed turbomachinery'. In: *Applied Thermal Engineering* 218 (2023), p. 119229.

[4] Yunus A. Cengel. *Introduction to thermodynamics and heat transfer*. McGraw-Hill, 1997.

[5] Theodore L. Bergman Frank P. Incropera David P. DeWitt. *Fundamentals of Heat and Mass Transfer*. John Wiley I& Sons, 2007.

[6] Theodore L Bergman et al. *Introduction to heat transfer*. John Wiley & Sons, 2011.

[7] Peter RN Childs. 'Rotating cylinders, annuli, and spheres'. In: *Rotating flow* (2011), pp. 177–247.

[8] Geoffrey Ingram Taylor. 'VIII. Stability of a viscous liquid contained between two rotating cylinders'. In: *Philosophical Transactions of the Royal Society of London. Series A, Containing Papers of a Mathematical or Physical Character* 223.605-615 (1923), pp. 289–343.

[9] Joseph Kaye and Everett Charles Elgar. 'Modes of adiabatic and diabatic fluid flow in an annulus with an inner rotating cylinder'. In: *Transactions of the American Society of Mechanical Engineers* 80.3 (1958), pp. 753–763.

[10] IS Bjorklund and WM Kays. 'Heat transfer between concentric rotating cylinders'. In: *Journal of Heat Transfer* 81.3 (1959), pp. 175–183.

[11] M. Fénot et al. 'A review of heat transfer between concentric rotating cylinders with or without axial flow'. In: *International Journal of Thermal Sciences* (2011), pp. 1138–1155.

[12] Steven T Wereley and Richard M Lueptow. 'Velocity field for Taylor–Couette flow with an axial flow'. In: *Physics of Fluids* 11.12 (1999), pp. 3637–3649.

[13] K Kataoka, H Doi and Tr Komai. 'Heat/mass transfer in Taylor vortex flow with constant axial flow rates'. In: *International Journal of Heat and Mass Transfer* 20.1 (1977), pp. 57–63.

[14] ZH Gu and TZ Fahidy. 'Characteristics of Taylor vortex structure in combined axial and rotating flow'. In: *The Canadian Journal of Chemical Engineering* 63.5 (1985), pp. 710–715.

[15] Karl Bühler and Norbert Polifke. 'Dynamical behaviour of Taylor vortices with superimposed axial flow'. In: *Nonlinear Evolution of Spatio-Temporal Structures in Dissipative Continuous Systems*. Springer, 1990, pp. 21–29.

[16] J. H. Lienhard IV and J. H. Lienhard V. *A Heat Transfer Textbook, fifth edition*. University of Houston, Cambridge, MA, 2020.

[17] Janne Nerg, Marko Rilla and Juha Pyrhonen. 'Thermal analysis of radial-flux electrical machines with a high power density'. In: *IEEE Transactions on industrial electronics* 55.10 (2008), pp. 3543–3554.

[18] S Seghir-Ouali et al. 'Convective heat transfer inside a rotating cylinder with an axial air flow'. In: *International journal of thermal sciences* 45.12 (2006), pp. 1166–1178.

[19] J Larjola M. Kuosa P. Sallinen. 'Numerical and Experimental Modelling of Gas Flow and Heat Transfer in the Air Gap of an Electric Machine'. In: *Thermal Science* 13.3 (2004), pp. 264–278. DOI: https://doi.org/10.1007/s11630-004-0041-4.

[20] A Northrop and JM Owen. 'Heat transfer measurements in rotating-disc systems part 1: The free disc'. In: *International journal of heat and fluid flow* 9.1 (1988), pp. 19–26.

[21] G. H. Dibelius and M. Heinen. 'Heat Transfer From a Rotating Disc'. In: Turbo Expo: Power for Land, Sea, and Air Volume 4: Heat Transfer; Electric Power; Industrial and Cogeneration (June 1990), V004T09A028.

[22] A. Romagnoli et al. 'A review of heat transfer in turbochargers'. In: *Renewable and Sustainable Energy Reviews* 79 (2017), pp. 1442–1460.

[23] A Diango et al. 'Influence of Heat Transfer on Gas Turbine Performance'. In: *Advances in Gas Turbine Technology* (2011), pp. 212–236.

[24] Kévin Rosset and Jürg Schiffmann. 'Extended windage loss models for gas bearing supported spindles operated in dense gases'. In: *Journal of Engineering for Gas Turbines and Power* 142.6 (2020), p. 061010.

[25] David A Howey, Peter RN Childs and Andrew S Holmes. 'Air-gap convection in rotating electrical machines'. In: *IEEE transactions on industrial electronics* 59.3 (2010), pp. 1367–1375.

[26] Manfred Mack. *Luftreibungsverluste bei elektrischen Maschinen kleiner Baugrösse*. na, 1967.

[27] James W Daily and Ronald E Nece. 'Chamber dimension effects on induced flow and frictional resistance of enclosed rotating disks'. In: (1960).

[28] Matlab. *Matlab documentation*. 2023. URL: https://it.mathworks.com/help/simscape/ug/basic-principles-of-modeling-physical-networks.html.

[29] Matlab. *Matlab documentation*. 2023. URL: https://it.mathworks.com/help/simscape/ref/constantvolumechamberg.html.

[30] Matlab. *Matlab documentation*. 2023. URL: https://it.mathworks.com/help/simscape/ref/pipeg.html.

[31] D. Roberts. 'The Application of an Induction Motor Thermal Model to Motor Protection and Other Functions (PhD)'. In: *University of Liverpool* (1986).

[32] Phil H Mellor, D Roberts and DR Turner. 'Lumped parameter thermal model for electrical machines of TEFC design'. In: *IEE Proceedings B (Electric Power Applications)*. Vol. 138. 5. IET. 1991, pp. 205–218.

[33] LE Olmedo and J Schiffmann. 'Towards a real-time capable hybrid-twin for gas-bearing supported high-speed turbocompressors'. In: *Energy* 275 (2023), p. 127385.

[34] Ansys. *Ansys Fluent Users Guide*. Version 2021 R2. 2021.

[35] Ansys. *Ansys Fluent Theory Guide*. Version 2021 R2. 2021.
[36] Ansys. *ANSYS Meshing User's Guide*. Version 13.0. 2010.